

University of Central Florida

STARS

Honors Undergraduate Theses

UCF Theses and Dissertations

2022

Mechanical Understanding and Optimization of Template Guided Core Needle Biopsy

Isaac Girgis

University of Central Florida



Part of the [Medical Biotechnology Commons](#), and the [Oncology Commons](#)

Find similar works at: <https://stars.library.ucf.edu/honorsthesis>

University of Central Florida Libraries <http://library.ucf.edu>

This Open Access is brought to you for free and open access by the UCF Theses and Dissertations at STARS. It has been accepted for inclusion in Honors Undergraduate Theses by an authorized administrator of STARS. For more information, please contact STARS@ucf.edu.

Recommended Citation

Girgis, Isaac, "Mechanical Understanding and Optimization of Template Guided Core Needle Biopsy" (2022). *Honors Undergraduate Theses*. 1447.

<https://stars.library.ucf.edu/honorsthesis/1447>

MECHANICAL UNDERSTANDING AND OPTIMIZATION OF TEMPLATE
GUIDED CORE NEEDLE BIOPSY

by

ISAAC E. GIRGIS

A thesis submitted in partial fulfillment of the requirements
for the Honors Undergraduate Thesis Program in Mechanical Engineering
in the College of Engineering and Computer Science
and in the Burnett Honors College
at the University of Central Florida
Orlando, Florida

Fall Term, 2022

Thesis Chair: Sang-Eun Song, Ph.D.

Thesis Committee Member: Yuanli Bai, Ph.D.

Copyright © 2022 Isaac E. Girgis

Abstract

Prostate cancer is the second highest cause of cancer related deaths among men. According to the diagnostic pathway for prostate cancer, a prostate biopsy is performed if an individual showed signs of lesions through high prostate-specific antigen (PSA) concentration or suggestive digital rectal exam (DRE) results. The core biopsy mechanism involves inserting a beveled needle into the organ and removing a cylindrical fragment of tissue. Many factors affect the histological quality of the sample, including fragmentation, needle deflection, and needle insertion velocity. If a biopsy core is not clinically viable, an alternative core will need to be taken, resulting in increased patient trauma and potential risk of infection.

Many of these relevant factors are impacted by sources of friction in the system. Prior studies have examined methods of decreasing the friction of the interactions between different components of the biopsy system to reduce the negative effects on histological sample quality. While scenarios have been explored that examine reducing the friction between the needle and tissue through sharpening and polishing techniques, the friction introduced by the needle guide in template guided core prostate biopsies has not been analyzed in the decades since its development. This study aims to introduce the biopsy guide as an additional source of friction which can be optimized to reduce friction force, while proposing and testing several configurations of the needle guide that would reduce the friction force of the system. A Finite Element Analysis (FEA) was conducted using SIMULA Abaqus modeling software, and the simulation was correlated with a derived equation that estimated friction force according to material properties.

The study demonstrated that configurations for the internal surface of the needle guide which provided decreased contact surface compared to the control needle guide resulted in lower friction force between the needle and guide. Conditions which had contact points oriented parallel to the direction of insertion had the lowest recorded friction force. This suggests that the traditional biopsy needle guide may be optimized to introduce less friction force by reducing the contact area between the needle and guide inner surface. This has application in reducing the number of passes required to obtain a histologically viable core specimen, and therefore reducing the opportunity for patients to develop infection.

Acknowledgements

I thank Dr. Sang-Eun Song for presenting me with this research opportunity, guiding me through the successful completion of this endeavor, and assisting me in receiving my honors distinction through my work done in this thesis.

I thank Dr. Yuanli Bai for being on my thesis committee and evaluating my work while providing inputs and evaluations that ultimately led to my success.

I thank the Office of Honors Research in the University of Central Florida Burnett Honors College for providing me a means of sharing my passion and my work to the public.

Table of Contents

List of Equations	viii
List of Figures	x
1 Introduction	1
1.1 Overall Background	1
1.2 Prostate Core Biopsy	2
1.3 Analysis of Core Biopsy Samples	4
1.4 Location Accuracy	6
1.5 Insertion Velocity	9
1.6 Simulation Background	11
2 Methods	18
2.1 Mathematical Derivation	18
2.2 Simulation Parameters	22
3 Results	28
3.1 Mathematical Correlation	28
3.2 Simulation Results	30
4 Discussion	39
4.1 Interpretation of Results	39
4.2 Application	43
4.3 Limitations and Future Study	45
Appendix A: Null Control Simulation Methodology	47
Appendix B: Control Simulation Methodology	53

Appendix C: Perpendicular 5-point Simulation Methodology	59
Appendix D: Perpendicular 3-point Simulation Methodology	65
Appendix E: Parallel 3-point Simulation Methodology	71
List of References	77

List of Equations

Equation 1: Friction Force with Surface Area Correction	11
Equation 2: Pressure	11
Equation 3: Stress	12
Equation 4: Stress Tensor	12
Equation 5: Stress Tensor Symmetry.....	13
Equation 6: Mean Stress	13
Equation 7: Relationship Between Pressure and Mean Stress.....	13
Equation 8: Strain	13
Equation 9: Strain Tensor	13
Equation 10: Strain Tensor Symmetry.....	14
Equation 11: Mean Strain	14
Equation 12: Young's Modulus	14
Equation 13: Poisson's Ratio	15
Equation 14: Maximum Tangential Stress.....	18
Equation 15: Derivation Step #1- Maximum Tangential Stress	19
Equation 16: Relationship of Tangential Stress and Strain	19
Equation 17: Tangential Strain in Terms of a Cylinder	20
Equation 18: Derivation Step #2- Tangential Strain in Terms of Young's Modulus	20
Equation 19: Derivation Step #3- Solving for Internal Pressure	20
Equation 20: Relationship Between Radius and Diameter	20
Equation 21: Derivation Step #4- Simplification.....	20

Equation 22: Friction Force with Area Correction Factor	21
Equation 23: Relationship Between Friction and Internal Pressure	21
Equation 24: Final Derived Equation Solving for Friction Force.....	21
Equation 25: Area of an Open Cylinder	21
Equation 26: Area of Contact per Perpendicular Ridge.....	41
Equation 27: Area of Contact per Parallel Ridge.....	41

List of Figures

Figure 1: Lobes of the Prostate Gland	5
Figure 2: Transperineal Ultrasound-Guided Biopsy.....	7
Figure 3: The Strain versus Stress Curve.....	15
Figure 4: Derived Equation Components.	19
Figure 5: Excel Derivation Spreadsheet 1	29
Figure 6: Excel Derivation Spreadsheet 2	29
Figure 7: Deformation Map of the Null Control Condition.....	31
Figure 8: Plot of Friction Force versus Time for the Null Control Condition.....	31
Figure 9: Deformation Map of the Control Condition.....	32
Figure 10: Plot of Friction Force versus Time for the Control Condition.....	33
Figure 11: Deformation Map of the Perpendicular 5-point Condition	34
Figure 12: Plot of Friction Force versus Time for the Perpendicular 5-point Condition	34
Figure 13: Deformation Map of the Perpendicular 3-point Condition	35
Figure 14: Plot of Friction Force versus Time for the Perpendicular 3-point Condition	36
Figure 15: Deformation Map of the Parallel 3-point Condition	37
Figure 16: Plot of Friction Force versus Time for the Parallel 3-point Condition	38
Figure 17: Contact Area of Experimental Conditions	42
Figure 18: Contact Area vs. Friction Force	42
Appx. A. Figure 1: Needle Dimensions.....	48
Appx. A. Figure 2: Needle Part Image	48
Appx. A. Figure 3: Needle Material Property.....	49

Appx. A. Figure 4: Null Control Dimensions.....	49
Appx. A. Figure 5: Null Control Part Image	50
Appx. A. Figure 6: Null Control Material Property.....	50
Appx. A. Figure 7: Null Control Assembly	51
Appx. A. Figure 8: Null Control Interaction.....	51
Appx. A. Figure 9: Null Control Boundary Conditions.....	52
Appx. A. Figure 10: Null Control Mesh	52
Appx. B. Figure 1: Needle Dimensions	54
Appx. B. Figure 2: Needle Part Image.....	54
Appx. B. Figure 3: Needle Material Property	55
Appx. B. Figure 4: Control Dimensions	55
Appx. B. Figure 5: Control Part Image.....	56
Appx. B. Figure 6: Control Material Property	56
Appx. B. Figure 7: Control Assembly	57
Appx. B. Figure 8: Control Interaction.....	57
Appx. B. Figure 9: Control Boundary Conditions.....	58
Appx. B. Figure 10: Control Mesh	58
Appx. C. Figure 1: Needle Dimensions	60
Appx. C. Figure 2: Needle Part Image.....	60
Appx. C. Figure 3: Needle Material Property.....	61
Appx. C. Figure 4: Perpendicular 5-point Dimensions.....	61
Appx. C. Figure 5: Perpendicular 5-point Part Image	62

Appx. C. Figure 6: Perpendicular 5-point Material Property	62
Appx. C. Figure 7: Perpendicular 5-point Assembly.....	63
Appx. C. Figure 8: Perpendicular 5-point Interaction	63
Appx. C. Figure 9: Perpendicular 5-point Boundary Conditions	64
Appx. C. Figure 10: Perpendicular 5-point Mesh.....	64
Appx. D. Figure 1: Needle Dimensions.....	66
Appx. D. Figure 2: Needle Part Image	66
Appx. D. Figure 3: Needle Material Property.....	67
Appx. D. Figure 4: Perpendicular 3-point Dimensions	67
Appx. D. Figure 5: Perpendicular 3-point Part Image	68
Appx. D. Figure 6: Perpendicular 3-point Material Property	68
Appx. D. Figure 7: Perpendicular 3-point Assembly	69
Appx. D. Figure 8: Perpendicular 3-point Interaction	69
Appx. D. Figure 9: Perpendicular 3-point Boundary Conditions	70
Appx. D. Figure 10: Perpendicular 3-point Mesh.....	70
Appx. E. Figure 1: Needle Dimensions	72
Appx. E. Figure 2: Needle Part Image.....	72
Appx. E. Figure 3: Needle Material Property	73
Appx. E. Figure 4: Parallel 3-point Dimensions.....	73
Appx. E. Figure 5: Parallel 3-point Part Image	74
Appx. E. Figure 6: Parallel 3-point Material Property.....	74
Appx. E. Figure 7: Parallel 3-point Assembly	75

Appx. E. Figure 8: Parallel 3-point Interaction.....	75
Appx. E. Figure 9: Parallel 3-point Boundary Conditions.....	76
Appx. E. Figure 10: Parallel 3-point Mesh.....	76

1 Introduction

1.1 Overall Background

The normal prostate is a 3 cm long, 4cm wide, and 2cm deep (anteroposterior diameter) inverted cone-shape accessory gland of the male reproductive organ (approximately 30g) that lies in the pelvic cavity below the urinary bladder and above the levator ani muscle (pelvic floor), behind the pubic symphysis and in front of the rectum through which it can be palpated by rectal examination. Prostate historically has an anterior (isthmus) and a posterior lobe, a middle (median) lobe, and two lateral lobes, although clinical classification may vary slightly.^{[1][2][3]} Prostate is a fibromuscular (1/3) and glandular (2/3) tissue. The glands are distributed in three zones including the transitional zone that contains about 5% of the prostatic volume and surrounds the prostatic urethra, the central zone that comprises 25% of the prostatic volume and surrounds the transitional zone, and the peripheral zone where 80% of the prostate cancers occur, surrounds the central zone and consists of 75% of the volume of the prostate.^[1]

In 2021, prostate cancer represented the most prevalent cancer type among males, accounting for 26% of all cancer diagnoses. In the United States, 1 in 8 males were expected to be diagnosed with prostate cancer, and a mortality rate of 11% ranks it as the second-highest cause of cancer death in males.^[4] The key factors in assessing the risk of prostate cancer development include age and family history; survival rates of men with prostate cancer are relatively high, with only a 2.5% lifetime risk of dying due to the disease, but the median age of death due to prostate cancer is 80 years old. These factors suggest that men aged 55 to 69 years should undergo periodic screening for prostate cancer.^[5]

Clinical screening for prostate cancer begins with an analysis of the level of prostate-specific antigen (PSA) in the blood. PSA is a serine-protease that is naturally produced by epithelial cells lining the prostate and is an essential protein in semen, and is normally found in low levels in the blood. Elevated concentrations of PSA (measured in nanograms per milliliter, ng/ml) act as a serum marker for cancerous lesions.^[6] Conventional clinical guidelines indicate that a serum PSA concentration of above 4ng/ml warrants further analysis, however the risk factors of the patient may suggest a cutoff of 3ng/ml or 2.5ng/ml. The lack of standardization in this diagnostic method is due to the many possible physiological conditions that may elevate serum PSA other than cancer, including prostate inflammation (prostatitis), benign prostatic hyperplasia, and even ejaculation.^[5] As a result, repeated screening and early detection of elevated PSA reduces prostate cancer mortality by over 20%, but the risk of false positive results is fairly significant.^{[7][8]} One trial demonstrated that over a 10-year period, 15% of men who were screened every 2 to 4 years experienced at least one false-positive result for prostate cancer.^[9] A secondary, less accurate method for diagnosing prostate cancer is the digital rectal examination (DRE), in which a physician will manually examine the posterior region of the prostate through the rectum to feel for a solid mass.

1.2 Prostate Core Biopsy

With the guidance of the physician, the results of a PSA or DRE screening may be followed by a prostate biopsy. A prostate biopsy is the only method of accurately determining if a patient has a cancerous lesion or not. A tissue biopsy mechanism generally contains a beveled needle with an indentation for an isolated specimen, and a deployment mechanism (spring-loaded, manual, etc.) that inserts a cutting sheath over the beveled needle. The tissue cutting system is separated into two phases: an initial phase in which needle force accumulates to the amount required to

separate the tissue, and a secondary phase where needle force stabilizes once the tissue has been separated.^[10] The variety of forces that act on the needle in each stage induce deflection and other sources of error that ultimately determine the accuracy and quality of the biopsy sample. There are two major variations of core prostate biopsies that are currently routinely performed, including the transrectal and transperineal (transgluteal is performed to a lesser extent), which differ in their point of insertion. Transrectal biopsies are maneuvered within the rectum before penetrating the rectal wall, while transperineal biopsies are done through superficial intervention. The transrectal ultrasound-guided (TRUS) biopsy may miss some anatomical portions of the prostate (favors probing of the posterior region) while transperineal biopsies favor the anterior prostate.^[11] TRUS procedures are more practical, since only a local anesthetic is required and can be completed within an office setting; while the perineal approach can be performed under general anesthesia, an increasing number of physicians are performing transperineal procedures under the same conditions as TRUS.^[12] Patient movement during TRUS biopsies can have a negative impact on biopsy results, representing an additional drawback that is avoided if the transperineal approach under general anesthesia is utilized. The efficiency of TRUS biopsies are paired with an increased likelihood to develop infection due to non-sterility and complications ranging from moderate to severe rectal hemorrhaging compared to the more sterile transperineal approach.^[13]

Recent biopsy mechanisms have been improved from the original sextant form through technological advances, better understanding of zonal anatomy of the prostate (allowing for consideration of lateral lesions), and computer modeling of localized prostate cancer.^[14] Robot-assisted TRUS has been found to increase biopsy precision, and the more accurate needle targeting has the potential to increase the detection of clinically significant prostate cancer per procedure. The use of prostate magnetic resonance imaging (MRI) in the risk stratification, diagnosis, and

treatment pathway of men with prostate cancer is expanding as well, providing more accurate needle insertion into the cancerous lesion and a more reliable diagnostic pathway for potential cancer patients.^[15] Incorporating multiparametric MRI into the diagnostic pathway as an initial test prior to prostate biopsy may reduce the proportion of men having unnecessary biopsies, improve the detection of prostate cancer, and increase the cost-effectiveness of the prostate cancer diagnostic and therapeutic pathways.^[16] The inherent direct relationship between the number of biopsy procedures performed and the complications experienced by the patient suggest the potential for the accuracy of MRI to play a role in developing a more rapid diagnosis and treatment implementation.

1.3 Analysis of Core Biopsy Samples

Core biopsy samples are analyzed by pathologists to determine the clinical application of the specimen. For the evaluation to be accurate, the biopsy specimen must have certain histological characteristics that qualify it as an appropriate model. The specimens are produced as cylindrical cores of the target tissue resulting from the shape of the cutting sheath. Primarily, the biopsy sample should have been taken from the region of interest (i.e., a lesion or growth). The specificity of the sample and the false negative rate of cancer diagnosis that it produces is largely dependent on the volume of the sampled tissue.^[17] Since this is correlated to its length, a longer biopsy core with greater diameter is a desirable characteristic. Fragmentation of the biopsy sample is also a concern, since no conclusive data can be drawn about the physiology of the region. When an optimal sample is obtained, it will be analyzed on a standardized scale called the Gleason Score, a grading system from 1 to 5 used to categorize the progression of the cancer within the tissue.^[18]

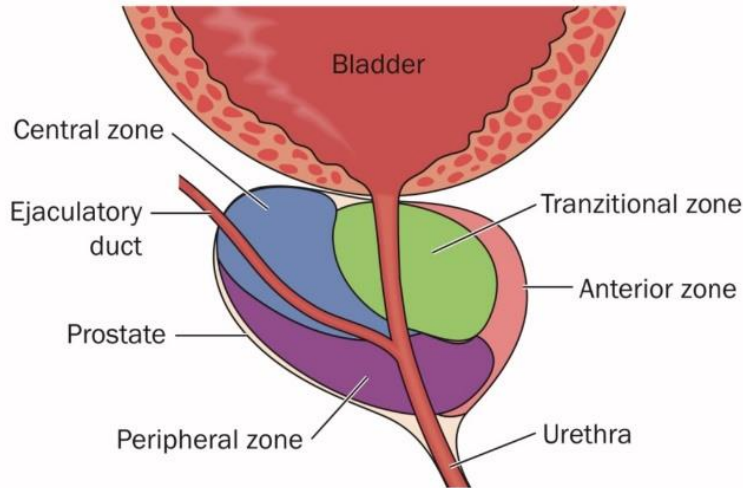


Figure 1: Lobes of the Prostate Gland

The clinical diagnostic pathway for prostate cancer begins with routine checks of PSA levels with a general practitioner. A detection of a high serum antigen level of this marker may be followed up with a DRE to physically check for lesions on the prostate. Suggestive results in these two examinations will typically be followed by a prostate biopsy. Transperineal biopsies are biased towards anterior zone of the prostate, while transrectal biopsies tend to evade this region.

Deflection of the needle and dynamic tissue deformation are two potential sources of error during the biopsy procedure that need to be accounted for. Tissue deformation includes three cases: the displacement of the tissue, relative sliding of multi-layer soft tissue and motions of the organs. The amount of gaps within soft tissue makes it easily compressible, causing the volume to change with deformation.^[19] Deformation of the tissue results from the force of the rigid needle at the focal point of the target before penetration, resulting in movement in the tissue layers and potential movement of the target. Innovations including model-based path planning and robotic steering of the needle have been proposed, but are largely inconsistent due to the inhomogeneity of the human tissue layers.^[20] Needle deflection involves the needle deviating from the linear trajectory of the needle and instead following a curved path, caused by the beveled needle tip and the flexibility of the body.^[21] A suggested solution to this phenomenon involves rotating the needle to continuously

redirect the deflection path, but histological analysis suggests this technique invokes tissue damage and expansion of the entry point.^[22] The factors affecting the histological quality of a core prostate biopsy sample can be categorized into variables affecting the location accuracy of needle insertion and variables affecting needle insertion velocity as it relates to tissue deformation.

1.4 Location Accuracy

The geometry of the needle tip is the most superficial aspect affecting the location accuracy of needle insertion into soft tissue. Core prostate biopsies are often performed using a tru-cut biopsy needle with a single bevel and a groove for the sample surrounded by a hollow cannula for sampling. Despite advances in imaging guided systems, including MRI-ultrasound fusion targeted biopsies (MRF-TB), deflection induced by these single-bevel needles causes variance between the target location and final sampling location.^[23] Ultrasound-guided techniques, including TRUS core biopsies, experience limitations in this area as well, since ultrasound probes inserted through the rectum may shift the positioning of the prostate or compressing it.

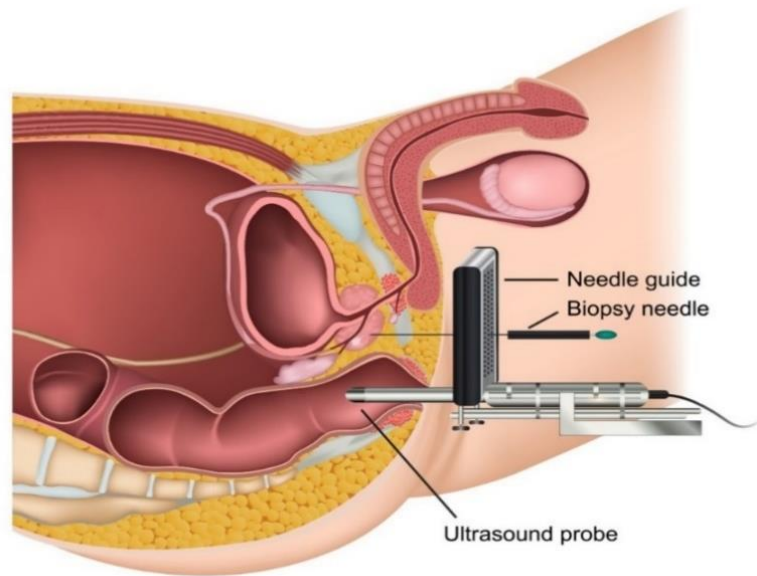


Figure 2: Transperineal Ultrasound-Guided Biopsy

The transperineal biopsy is the only prostate biopsy method that employs the use of a template. By working with imaging results, the clinician will utilize a range on the template to gather multiple distributed cores from the area of interest. Sources of variability when utilizing a template include the freedom of rotation of the needle within the insertion template, deformation of the tissue upon insertion, reduction of the insertion velocity of the needle, and deflection of the needle from the linear path. Template guides may introduce additional frictional forces and limit the needle from being inserted in the location of interest.

The single-bevel needles in current hand-held biopsy devices often deflect significantly during needle insertion, causing variance in the targeted and actual locations of the sampled tissue. This variance can lead to inaccurate sampling and false-negative results.^[24] Studies have shown that the inclusion of multiple bevel tips can generate opposing forces that balance the arc motion of the needle within the tissue. However, currently proposed multi-bevel designs suffer from altering the tissue separation point, and thus reducing tissue sampling length and potentially compromising the cancer diagnostic accuracy of the sample.^[23] A full-core or side-notch biopsy needle system represents another variable affecting the technique that was used to extract the sample. A randomized trial comparing the histopathological quality and physical features of biopsy cores indicated that the full core system produced significantly higher quality samples than the

side notch system, favoring this layout to increase sample length and decrease fragmentation rate.^[25] Even within multi-bevel needle systems, there remains a variation in sampling ability. One study demonstrated that Fork-tipped and Franseen geometries recorded producing better overall histological quality than reverse-bevel and Menghini tips, evidently displaying an inconsistency in the various multi-bevel needle designs.^[26]

Location accuracy in core biopsy insertion is also dependent on the interaction between the biopsy template and the needle insertion mechanism. Application of a grid or template is only utilized in transperineal biopsy approaches and cannot be used in transrectal biopsies. The general consensus according to clinical trials of the utilization of a biopsy template remains controversial. In core prostate biopsies, following a template could better ensure uniform and well distributed sampling of the prostate compared to the traditional freehand biopsy approach, possibly decreasing the chance of false-negative biopsy.^[27] However, the application of a grid or template has also been shown to be susceptible to error; the increased friction associated with a smaller grid clearance does have a drawback in the reduction of the insertion velocity of the needle. This suggests an increase in tissue deformation, but underlying improvement in precision and accuracy of needle insertion is generally present regardless of the insertion speed.^[28] The tightness of the stabilizing agent to the needle affects the correlation of the grid coordinates and degrees of rotation during needle insertion, potentially allowing technical and equipment-associated error. This suggests that technique remains critical even when using a template for insertion, and therefore does not necessarily imply reproducible needle placement.^[29] An additional drawback to the application of an external grid is the limitation it presents to the physician in the insertion of the needle, since guides are stable and may restrict the needle from being directed to a location of interest.

1.5 Insertion Velocity

The rate at which the needle is inserted into the target tissue has a significant effect on the final histological quality of the sample, mainly through the effect of acceleration on dynamic soft tissue deformation. The results of one experimental analysis showed that maximum tissue deformation occurs upon insertion of the needle, obscuring the target lesion at the point in which the tissue and needle made contact. Past that point, an increase in insertion velocity leads to a decrease in deformation due to the generation of kinetic and viscous energies. This produces a decrease in targeting error and a more histologically valuable biopsy sample.^[19] During insertion of the needle, the contact between the surface of the needle and the tissue creates friction stresses. Average friction stress along the needle-tissue interface has been shown to decrease with increasing insertion speed.^[30] Increased needle insertion velocity minimizes the force required in the first phase of tissue-cutting procedure, while minimizing tissue displacement in phase two. High velocity needle insertion also yields a greater improved histological sample quality by producing biopsy cores with a greater mean molecular weight.^[10]

The characteristics of the biopsy needle according to its manufacturing is another source of variability in obtaining quality biopsy core samples. One aspect of this is the design of the grooves and cannulas to accommodate a greater length of tissue sample. One study which compared the cancer detection rates of 19mm and 29mm cutting lengths concluded that taking the longer cores led to an improved cancer detection rate of nearly 20%.^[31] The process of developing a stainless-steel needle involves running a tube through a mandrel and a die to control the inner and outer diameters of needle, respectively. With the rise of a clinical preference for smaller diameter needles (i.e., 18-gauge) afforded by decreased trauma to the patient, not only are a greater number of passes required to obtain a sufficient amount of tissue for analysis, but the commercial

method of using a mandrel is not applicable, so the inner surface is often less smooth than larger diameter needles, negatively impacting sample quality. The development of polishing techniques for 18-gauge core biopsy needles has been shown to improve histological sample quality and decrease fragmentation due to a decreased insertion friction force.^[17] Aside from interior polishing, exterior sharpening of the needles using a trocar have been shown to be superior to industry standard needles in histological sample quality, targeting the planned position, and performing the biopsy in the proper time.^[32]

In order to optimize the prostate core biopsy procedure and produce quality samples with as high a frequency as possible, the factors negatively impacting needle insertion must be minimized. As friction plays a large role in the velocity of insertion, the displacement of the tissue, and the likelihood of fragmentation of the core, this study aims to reduce the friction force along the interface between the template guide and outer surface of the cannula. Some previous studies, including ones already described, have explored methods of reducing friction within the biopsy system. Sharpening the beveled needle tip, polishing the inner surface of the needle to minimize roughness, and other methods have been suggested. However, there seems to be a lack of data examining the interaction between the biopsy template and the needle itself. In the decades since the application of template guided biopsies, the needle guide has been unadvanced and disregarded as a potential source of friction in the system. This study will demonstrate this component as contributor to friction force and examine several different configurations for the internal pattern of the biopsy guide to determine which one contributes the least friction force to the insertion of the needle.

1.6 Simulation Background

This study will use the simulation software SIMULA Abaqus and conducting a Finite Element Analysis (FEA) to determine the difference in resulting friction forces of the various biopsy guide designs. The Abaqus software offers a unique analysis for dynamic interactions such as the ones in this study that make it preferable to alternative design software. Abaqus has a robust contact solver that allows for greater control over interaction parameters and has the ability to scan the model at each step of analysis to recognize potential interaction conflicts. This mechanism is not found in alternative software, such as SOLIDWORKS.^[33] Additionally, Abaqus allows precise control over the properties of materials used in the model. It contains a large library for material models with material calibration tools that allow specific characterization of materials.

The Abaqus software is programmed with several mathematical parameters to output accurate information regarding forces and deformation of parts. Friction force is given by the equation below;

$$F = \mu \cdot N \cdot (1 + f_A)$$

Equation 1: Friction Force with Surface Area Correction

Where F is the friction force in Newtons (N), μ is the coefficient of friction, N is the normal force in Newtons (N), and the quantity $\cdot (1 + f_A)$ reflects the correction of friction force due to surface area. The normal force is related to pressure by the equation below;

$$p = \frac{N}{A}$$

Equation 2: Pressure

Where N is the normal force and A is the area upon which the force is exerted in square meters (m²). Normal force is dependent upon the contact area, with a greater contact area between two surfaces contributing to a larger value and a smaller area of contact resulting in a lower value of the normal force. The coefficient of friction is dependent upon the material characteristics of the two surfaces in contact.

There are two additional parameters that the Abaqus software computes when determining the deformation of objects, being stress and strain. Stress, measured in Pascals (Pa), refers to the quantity of force spread out per unit area, and is designated by the symbol σ .

$$\sigma = \frac{F}{A}$$

Equation 3: Stress

Stress is a tensor made up of 6 Cartesian components, reflecting the different applications of a force on a three-dimensional object. The first index of stress indicates which face of the object is experiencing the force. The component σ_1 indicates the stress in the x-axis dimension, σ_2 indicates stress in the y-axis dimension, and σ_3 indicates stress in the z-axis dimension. These are collectively referred to as σ_i . The second index is denoted by σ_j , which refers to the direction the force is being applied on the object. This index follows the same conventions described for σ_i . Collectively, these stress components form the following matrix.

$$\begin{pmatrix} \sigma_{11} & \sigma_{12} & \sigma_{13} \\ \sigma_{21} & \sigma_{22} & \sigma_{23} \\ \sigma_{31} & \sigma_{32} & \sigma_{33} \end{pmatrix}$$

Equation 4: Stress Tensor

$$\sigma_{ij} = \sigma_{ji}$$

Equation 5: Stress Tensor Symmetry

The mean stress, σ_m , is equivalent to the average of σ_{11} , σ_{22} , and σ_{33} . Pressure is directly related to the average stress.

$$\sigma_m = \frac{\sigma_{11} + \sigma_{22} + \sigma_{33}}{3} = \frac{\sigma_1 + \sigma_2 + \sigma_3}{3}$$

Equation 6: Mean Stress

$$P = -\sigma_m$$

Equation 7: Relationship Between Pressure and Mean Stress

The second parameter that the Abaqus system utilizes is mechanical strain. Strain is a unitless value, represented by the symbol ε , referring to the deformation of an object when placed under stress. Strain is quantified as the change in length divided by the initial length of a target.

$$\varepsilon = \frac{\Delta l}{l_0}$$

Equation 8: Strain

Similar to stress, strain is a tensor with two indexes, ε_i and ε_j , with three components each reflecting the different surfaces on which the target may experience the deformation, and the direction of the deformation itself, respectively.

$$\begin{pmatrix} \varepsilon_{11} & \varepsilon_{12} & \varepsilon_{13} \\ \varepsilon_{21} & \varepsilon_{22} & \varepsilon_{23} \\ \varepsilon_{31} & \varepsilon_{32} & \varepsilon_{33} \end{pmatrix}$$

Equation 9: Strain Tensor

$$\varepsilon_{ij} = \varepsilon_{ji}$$

Equation 10: Strain Tensor Symmetry

The mean strain can be expressed in a parallel fashion to mean stress.

$$\varepsilon_m = \frac{\varepsilon_{11} + \varepsilon_{22} + \varepsilon_{33}}{3} = \frac{\varepsilon_1 + \varepsilon_2 + \varepsilon_3}{3}$$

Equation 11: Mean Strain

There are three additional variables related to stress and strain that need to be specified when designating material properties in the Abaqus software, those being Young's Modulus, yield stress, and Poisson's Ratio. Young's Modulus is a property of the material that indicates how easily it can stretch and deform. In essence, Young's Modulus gives the stiffness of the material, and is represented by the symbol E . This variable correlates stress to strain and is the slope of the graph plotting strain versus stress. It is measured in newtons per square meter (N/m^2) or pounds per square inch (psi) depending on the unit system.

$$\sigma = E \cdot \varepsilon$$

Equation 12: Young's Modulus

Yield stress (also referred to as yield strength) is the material property which marks the transition from elastic property to plastic property. The extent of a material's elastic property represents its ability to temporarily deform and then return to its original shape under a given amount of strain, whereas the point at which the material surpasses the yield stress and undergoes permanent deformation before fracturing is considered the extent of its plastic property. On a graph

plotting strain versus stress, yield stress would be represented by the first local peak as strain increases.

Poisson's ratio, represented by the symbol ν , measures the deformation of a material in the direction perpendicular to which the force was applied.

$$\nu = -\frac{\epsilon_t}{\epsilon_l}$$

Equation 13: Poisson's Ratio

When a material experiences strain due to a tensile force, it will elongate parallel with the force and shrink perpendicular to the force before fracturing, and Poisson's ratio is used to quantify this phenomenon. It is calculated as the negative ratio of transverse strain to axial strain.

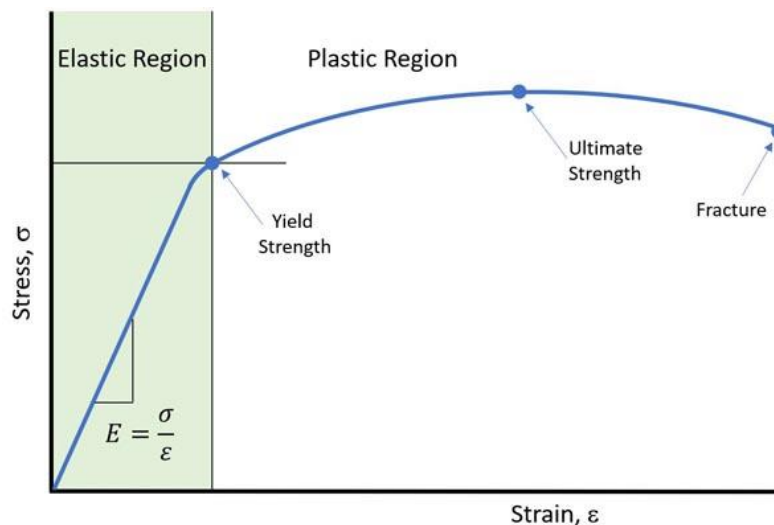


Figure 3: The Strain versus Stress Curve^[34]

As strain initially increases, the deformation of the material is linear and elastic, meaning that the deformation is temporary and the object will return to its initial shape if the stress is removed. This characteristic continues until the yield stress, the point at which the material property shifts to now experience permanent deformation. The curve is no longer linear, and a further increase in strain will result in fracture. The Young's Modulus is the slope of the linear portion of the graph.

The varying patterns of the internal surface of the biopsy template were designed to compare the effects of the number of contact points and orientation of contact points relative to the direction of needle insertion on the resulting friction force. Instead of a smooth inner surface, the pattern of the guides was designed as semicircular extrusions running in the direction of the specified condition. To examine a wide range of possibilities for friction reduction scenarios, models were tested with three and five of these internal patterns, running either parallel or perpendicular to the direction of needle insertion. In addition, a control condition is included with no internal surface pattern to represent the current industry template guide design. Due to the nature of the simulation software, it was predicted that simulating the needle with exactly the same diameter as the guide it was entering would not produce enough contact for the software to produce any measurable friction force values. To examine, this, a null control condition was performed first with the outer diameter of the needle and internal diameter of the guide being equal. If the results of this condition show a lack of measurable results, the diameter of the needle will be increased consistently by a known value in each of the remaining conditions.

In order to maintain the MRI compatibility of this simulated study, as is the standard of care in the medical field concerning prostate biopsies, the material used for the biopsy needle and the template guide must be MRI compatible. The biopsy needle was modeled as titanium according to prostate biopsy protocol.^[35] Because a template guide with an internal surface pattern is a novel concept, the potential materials had to be considered on the basis of aligning with medical safety protocol. Additionally, due to the small size of the guide (approximately 1.27mm in diameter) the most appropriate and practical method of large-scale production of these parts would be through injection molded plastics. As a result, the material nylon was chosen. It is a low friction, nontoxic material that is relatively cheap and may be used for injection molded plastics.^[36] A potential

application of this nylon template guide is that the biopsy template may be designed to allow to exchange of the internal guide component. After a certain number of uses, the deformation of the plastic may be to great enough to allow nonaxial movement to the needle while inserting, so this mechanism would allow the healthcare provider to easily swap out used guides for new ones.

Lastly, the characteristics of the needle part of the simulation model will be modified to fit within the scope of the study. Since there is an emphasis on examining the force of friction between the needle and the template guide and not the action of the needle once inside a phantom tissue, the needle tip will be designed as a short cone rather than a beveled tip that is typical of biopsy needles. Additionally, the needle will be represented as a solid cylinder rather than a hollow tube due to the fact that the predominant interaction will be the result of deformation of the nylon cylinder. As titanium is over fifty times stronger than nylon^{[37][38]}, any deformation of the surface of the titanium needle will be negligible and therefore can be simulated as solid.

2 Methods

2.1 Mathematical Derivation

Before carrying out a simulation, the physical scenario which the simulation claims to represent needs to be formulated into an equation that can be used to produce expected values. By doing this, the accuracy of the simulation to a physical circumstance can be assessed according to the degree of similarity between the expected and actual results.

The system that is to be represented by the simulation is one in which a cylindrical object is experiencing only internal pressure in the outward direction, reflecting the needle moving through the guide and causing deformation. In this system, there are two related stresses placed on the cylinder: tangential stress ($\sigma_{\theta\theta}$), which occurs tangent at every point on the cylinder, and radial stress (σ_{rr}) in which the force is applied along the radius of the cylinder beginning at the center and being expressed outwardly. Additionally, the needle guide can be approximated as a thin-walled vessel due to the fact that the thickness of the wall of the cylinder is around 1/10th the length of the radius of the cylinder (e.g., the radius of the guide is 1.27mm and the thickness is 0.17mm, making the ratio approximately 1/13). This allows us to disregard the radial stress, which will be negligible in magnitude. Therefore, maximum stress of the system can be given by the equation below.

$$\sigma_{\theta\theta} = \frac{P_i(d_i + t)}{2t}$$

Equation 14: Maximum Tangential Stress

The equations regarding stress and strain and the related variables, in addition to several other fundamental equations of material properties, will be used to derive an equation for the system that estimates friction force.

Fundamental Equations	Symbol	Variable
$\sigma_{rr} \approx 0$	P_i	Internal Pressure
$\sigma_{\theta\theta} = \frac{P_i(d_i + t)}{2t}$	$\sigma_{\theta\theta}$	Tangential stress
$\sigma = E \cdot \varepsilon$	σ_{rr}	Radial stress
$\varepsilon = \frac{\Delta\mu}{r_i}$	d_i	Inner diameter
$r_i = \frac{1}{2}d_i$	r_i	Inner radius
$F = \mu \cdot N(1+f_A)$	t	Thickness
$P = \frac{F}{A}$	E	Young's Modulus
$A = \pi d_i \cdot l$	μ	Coefficient of friction
	N	Normal force
	f_A	Area correction factor
	$\Delta\mu$	Overlap between contact surfaces

Figure 4: Derived Equation Components

These are the fundamental equations (left) and variables (right) that were used for the derivation.

The derivation begins with the equation for maximum tangential stress of the cylinder.

$$\sigma_{\theta\theta} = \frac{P_i(d_i + t)}{2t}$$

Equation 15: Derivation Step #1- Maximum Tangential Stress

The relationship between stress and strain through Young's Modulus, and the definition of strain through Young's Modulus is then applied.

$$\sigma_{\theta\theta} = E \cdot \varepsilon_{\theta\theta} \therefore \varepsilon_{\theta\theta} = \frac{\sigma_{\theta\theta}}{E}$$

Equation 16: Relationship of Tangential Stress and Strain

$$\epsilon_{\theta\theta} = \frac{\Delta\mu}{r_i}$$

Equation 17: Tangential Strain in Terms of a Cylinder

This allows the rearrangement of the equation to solve for tangential strain in terms of Young's Modulus.

$$\epsilon_{\theta\theta} = \frac{P_i(d_i+t)}{2 \cdot t \cdot E} \approx \frac{\Delta\mu}{r_i}$$

Equation 18: Derivation Step #2- Tangential Strain in Terms of Young's Modulus

The equation can then be rearranged to solve for internal pressure.

$$P_i = \frac{\frac{\Delta\mu}{r_i} (2 \cdot t \cdot E)}{(d_i + t)}$$

Equation 19: Derivation Step #3- Solving for Internal Pressure

In order to solve the equation for tangential strain in terms of a cylinder, the equation must be rewritten completely in terms of internal diameter for consistency.

$$r_i = \frac{1}{2} d_i$$

Equation 20: Relationship Between Radius and Diameter

Substituting this relationship and removing the complex fractions provides the following equation.

$$P_i = \frac{4 \cdot \Delta\mu \cdot t \cdot E}{d_i(d_i + t)}$$

Equation 21: Derivation Step #4- Simplification

Finally, since the quantity of interest is friction force, internal pressure must be substituted with the friction force equivalent.

$$F = \mu \cdot N(1+f_A)$$

Equation 22: Friction Force with Area Correction Factor

$$P_i = \frac{F}{A}$$

Equation 23: Relationship Between Friction and Internal Pressure

By applying the relationship between pressure and friction force and rearranging the equation to solve for friction force, the final form of the derived equation is achieved.

$$F = \frac{4\mu \cdot \Delta\mu \cdot t \cdot E \cdot A}{d_i(d_i + t)}(1 + f_A)$$

Equation 24: Final Derived Equation Solving for Friction Force

Since the internal pressure is being applied over an open cylindrical contact surface, the area quantity will be equivalent to the area of the internal surface of a tube.

$$A = \pi \cdot d_i \cdot l$$

Equation 25: Area of an Open Cylinder

This derived equation can be used to estimate the friction force associated with a needle passing through a cylinder and exerting an internal pressure along its inner surface. The degree of correlation between the resulting friction force of the simulation and the estimated values of the derived equation will indicate how accurately the simulation reflects physical conditions. Due to the fact that the experimental conditions vary widely in the orientation and number of contact

points, the result of the derived equation will have a high margin in representing the validity of the simulation. The control condition will have a smaller margin due to this lack of variability.

2.2 Simulation Parameters

The SIMULA Abaqus software was used to perform a finite element analysis on a simulation of a biopsy needle passing through a guide. Several constraints were placed on the study. Firstly, the simulation will take place under dry friction conditions, meaning the application of lubricants or similar friction-reducing substances will not be employed. The dimensions of the biopsy needle will follow the specifications of an 18-gauge biopsy needle. Needles of varying dimensions will produce different results.

Because Abaqus inputs do not specify units, a consistent set of units is required to be utilized across the entire simulation setup (i.e., International System of Units (SI), SI units with millimeters as length, etc.). In this simulation, the following units were used: length was designated in mm, force was designated in Newtons (N), time was designated in seconds (s), stress in MPa (N/mm^2), and energy in milli Joules (mJ).

Two parts will make up the simulation: first, a short, narrow, solid cylinder with a conical tip representing the outer cannula of the biopsy needle. The template guides were represented by hollow cylinders with varying internal surface patterns according to the condition. The needle was constructed as a rotation around the y-axis, with a length of 5mm and a shallow conical tip. The conical tip was utilized as opposed to the traditional beveled needle tip because any interaction between the needle tip and a target tissue is outside of the scope of this study. In order to determine the diameter of the needle, a null control condition was performed in which the radius of the needle was set equal to the radius of a guide with no internal surface pattern. If the interaction between

the guide and needle is approximately zero, this will indicate a need to increase the diameter of the needle for the purpose of simulation in order to produce quantifiable results. The outer diameter of the needle and the inner diameter of the guide were both dimensioned to 1.27mm for the null control condition, and the radius of the needle will be increased to 0.6395mm if the null condition produces a positive result. For conditions employing an internal surface pattern, the pattern was modeled as semicircular ridges with a radius of 0.11mm and running direction specified by the condition. All needle guides were 1mm in length.

In all conditions, the material of the needle was titanium and the material of the guide was nylon. The parts that both of these materials were applied to were solid and homogeneous. The titanium had a Young's Modulus of 113 GPa and a Poisson's ratio of 0.3. The nylon had only elastic material behavior, with a Young's Modulus of 2700 MPa and a Poisson's ratio of 0.39. The Nylon material also had a Yield Stress of 45 MPa.

The following five conditions were tested, reflecting the range of internal surface patterns of the needle guide for this study: Null Control, which had no internal surface pattern; Control, which had no internal surface pattern; Perpendicular 5-point contact, which had five ridges running perpendicular to the direction of insertion; Perpendicular 3-point contact, which had three ridges running perpendicular to the direction of insertion; and Parallel 3-point contact, with three ridges running parallel with the direction of insertion. Each of these conditions were placed in a separate model in Abaqus along with the needle, a total of two parts per model. Images of each step in the methodology of developing each simulation condition can be viewed in Appendices A-E.

All conditions were assembled with the direction of insertion going towards the positive y-axis direction, and those that contained internal ridges had them uniformly distributed along the

inner surface of the guide. All guides had a height of 1mm, and the distance between the innermost points of contact and the center of the cylinder were constantly dimensioned at 0.635mm to reflect the 1.27mm outer diameter of an 18-gauge needle.

The Abaqus software has an integrated pathway with an intuitive order of steps to allow the simulation to be developed successfully. First, the parts of the model had to be created in the Parts tab. In this step, the dimensions of the needle guide and needle were specified, and a three-dimensional model was developed. For the two needle guide conditions which had the internal pattern running perpendicular to the direction of needle insertion, the 360° revolution around the y-axis was used to create the cylinder. These conditions were initially sketched as an outline of the perimeter of the guide in one quadrant, and the revolution around the y-axis developed it into a three-dimensional part. For the two needle guide conditions in which the internal ridges were running parallel with the direction of needle insertion, an extrusion was used. These parts were initially sketched as a smaller circle inscribed in a larger circle with the ridges part of the internal circle, and an extrusion of a certain width (i.e., the height of the guide, 1mm) developed the condition into a three-dimensional part. Several constraints were used in the sketching of the guides. The internal ridges were constrained to be equal in radius and equally spaced apart from one another across the 1mm length of the guide. The outer and inner surfaces were parallel with one another, and the lower and upper surfaces of the guide were parallel with one another.

The next tab to be modified was the Properties tab. This tab was used to apply material properties to each of the parts in the model. The needle guide was assigned the plastic material Nylon. This material has isotropic elastic properties without compression or tension capabilities. The Young's Modulus was designated to be 2700 MPa (or 2.7GPa) and the Poisson's ratio 0.39, and the material was solid and homogeneous. The needle was assigned to be titanium with only

isotropic elastic properties as well. The Young's Modulus was designated to be 113,000 MPa (equivalent to 113 GPa), nearly fifty times that of nylon, and a Poisson's ratio of 0.3.

The following tab to be completed was the Assembly tab. In this tab, the parts of a model were placed in a three-dimensional space in the desired orientation. For all of the conditions, the direction of insertion was oriented as the positive y-axis direction, meaning the needle would move upward through the needle guide. The entry point of the guide was placed at 0.25mm above the origin, and the tip of the needle was placed at the origin facing upward to move through the guide. A reference point was also added at 0.25mm above the origin along the y-axis for later use.

The next tab to be completed was the Step tab. This tab contains options for different analysis types and output controls. In this tab, a new set and history output were created. The set is used to associate the dynamic part of the model with the reference point, and a history output of certain data is generated according to what forces that reference point experienced during the simulation. Under Tools, the reference point at 0.25mm above origin was created as a new set. Then the History Output Manager was used to create a new History Output that is correlated not with the entire model, but with the new reference point set that was just created. The variables that were selected to be outputted were the reactive forces in all three dimensions (RF1, RF2, and RF3), though the major force of interest is RF2 because this represents the friction force that the needle experiences as a result of entering through the guide. The guide will slightly deform upon entry of the needle, and as a result produce a small output of force in the x and z dimensions, but these values were expected to be approximately zero. Within the Step tab, the two interfaces that would result in the duration of the simulation were also specified. An initial step was created in which no propagation of the needle takes place, but was oriented in the correct position as in the assembly. A propagation step was also specified (called Step-1), where incrementation was set; the initial

increment was 0.05, the minimum was 1E-008, and the maximum was 1. The maximum number of increments was set to be 10,000, and the Nlgeom was turned on to account for nonlinear stress and strain in the simulation.

The next tab to be completed was the Interaction tab. In this tab, two interactions were designated: an initial and a Step-1 propagation interaction. The initial interaction type was a standard surface-to-surface contact in which the master surface was the entire outer surface of the needle and the slave surface was the inner surface of the guide, including the ridges and the non-contact areas. Three-dimensional surfaces were not smoothed. Also, within the Interaction tab, the reference point was coupled to the entire outer surface of the needle. This was done so that the reference point can be made to move under certain boundary conditions and allow the entire needle to move accordingly.

The following tab to be completed was the Load tab. Within this tab, boundary conditions are designated to fix certain aspects of the model and apply an initial force in the desired direction. Three boundary conditions were used for this simulation. Firstly, a single point of the guide was constrained to be fixed in place; the boundary condition type was Symmetry/Antisymmetry/Encastre. This was done so that the needle guide would not move when contact with the needle was established. The second boundary condition type was also Symmetry/Antisymmetry/Encastre. Here, the bottom surface of the needle guide (the face pointing in the direction of the needle) was restricted to allow no movement in the y-direction. By doing this, the cylinder will be allowed to expand and contract when in contact with the needle, but the combination of the fixed point and the lack of vertical movement of the bottom surface will fix the entire cylinder in place. The third boundary condition type was Displacement/Rotation, and was

placed on Step-1. This third boundary condition moved the reference point, and therefore the entire needle, 2.0mm in the U2 direction (upward, positive y-axis).

The final tab to be completed before running the simulation was the Mesh tab. Here, each part of the model would be covered in a grid of certain sized seeds that would allow visualization of the varying deformation on different parts of the model. The needle guide was designated to have a seed size of 0.01, and each condition had a different number of total elements due to the difference in shape. The needle was given a seed size of 0.02 equaling approximately 1300 total elements.

The tabs described above were completed for each condition, and the simulations were run under the Job tab. After the simulation was completed, the Visualization tab showed how different elements of the mesh experienced different deformation, indicated by a color gradient. An XY plot of the friction force over time in the U1, U2, and U3 directions (i.e., RF1, RF2, and RF3, respectively) were generated for each model for comparison.

3 Results

3.1 Mathematical Correlation

The input and output parameters of the equation were made into a function in an Excel spreadsheet and values for each input variable the control condition and experimental conditions were specified (Figures 5 and 6, respectively). The control condition will have an inserted contact length of 1mm because the needle will be contacting the inner surface of the guide for the whole length of the guide. The experimental conditions which have a smaller contact area will not be in contact with the needle in the same manner, so a lower contact length is estimated. Additionally, the area correction factor will be smaller for the experimental conditions compared to the control condition due to the smaller number of contact points and total area of contact in the experimental conditions. The inner diameter of the guide, thickness of the guide, and overlap between the needle and the guide remain constant for all conditions. According to the derived equation, the control condition should produce a relative friction force of approximately 8.43N, while the experimental conditions are estimated to have a friction force of around 3.09N. These values provide a rough estimation of the friction force and are expected to vary in magnitude in the actual simulation, especially in the case of the experimental conditions, since this single equation is used to correlate all the different experimental conditions and their associated variability of the contact surfaces (i.e., number and orientation of contact point). The friction force of the control condition estimated by the equation should be more accurate in comparison. Therefore, a margin of 50% for the average of the friction forces of the experimental conditions (i.e., 3.09 ± 1.55) and a margin of 30% for the control condition (i.e., 8.43 ± 2.53) will be used to evaluate the validity of the simulation.

	A	B	C	D
1	Control			
2	Input parameters	Variable	Theoretical Value	Unit
3	Young's modulus	E	2700	MPa
4	Friction coefficient	μ	0.4	-
5	Area correction factor	f_A	0.2	-
6				
7	Inner diameter	d_i	1.27	mm
8	Thickness	t	0.165	mm
9	Overlap distance	$\Delta\mu$	0.0045	mm
10	Inserted contact distance	Δl	1	mm
11				
12	Output parameters	Variable	Theoretical Value	Unit
13	Contact area	A	3.98982267	mm ²
14	Internal pressure	P_i	4.400120717	MPa
15	Friction force	F	8.426736665	Newton

Figure 5: Excel Derivation Spreadsheet 1
Results of the Control condition as estimated by the derived equation.

	A	B	C	D
1	Experimental			
2	Input parameters	Variable	Theoretical Value	Unit
3	Young's modulus	E	2700	MPa
4	Friction coefficient	μ	0.4	-
5	Area correction factor	f_A	0.1	-
6				
7	Inner diameter	d_i	1.27	mm
8	Thickness	t	0.165	mm
9	Overlap distance	$\Delta\mu$	0.0045	mm
10	Inserted contact distance	Δl	0.4	mm
11				
12	Output parameters	Variable	Theoretical Value	Unit
13	Contact area	A	1.595929068	mm ²
14	Internal pressure	P_i	4.400120717	MPa
15	Friction force	F	3.089803444	Newton

Figure 6: Excel Derivation Spreadsheet 2
Results of the experimental conditions as estimated by the derived equation.

However, the results of the derived equation demonstrate that a lower contact area is expected to produce a lower friction force, already providing theoretical and mathematical justification for the simulation. The results of the simulation following a parallel trend will also factor into its evaluation of validity. The dimensions, constants, and values applied to the derived equation were specified as represented in the simulation itself.

3.2 Simulation Results

The Null Control condition was the first condition simulated. This condition was designed to have the outer diameter of the needle and the inner diameter of the guide both be 1.27mm to determine if a manual overlap needed to be simulated. The color deformation map and plot of the resulting friction force RF2 are shown below. As shown in Figure 7, the deformation map depicts no deformation of the needle guide as all of the seeds remains at the initial baseline value and associating representative color. The needle itself experienced some reactive force, not as a result of interaction with another surface but due to the movement of the needle upwards through space. This is shown by the live deformation values on the left side of the image equaling approximately zero. The apparent lack of interaction between the two surfaces was confirmed by the plot of the friction force over the course of the simulation.

As shown at the top left corner of the plot of friction force (Figure 8), the scale for the reactive forces was at an order of magnitude of 10^{-9} N. This represents an extremely small friction force that is far outside the margin of the predicted values of the derived equation, and effectively represents no interaction between the needle and the guide. The oscillating trend of the plot also suggests that the force was experienced due to motion and not contact with the other surface, as the expected trend (i.e., a gradual increase in friction force before leveling off at a maximum value)

was not seen. Therefore, the remaining experimental conditions were be conducted with a slightly larger diameter needle to induce an overlap between the two parts in order to appropriately compare the conditions.

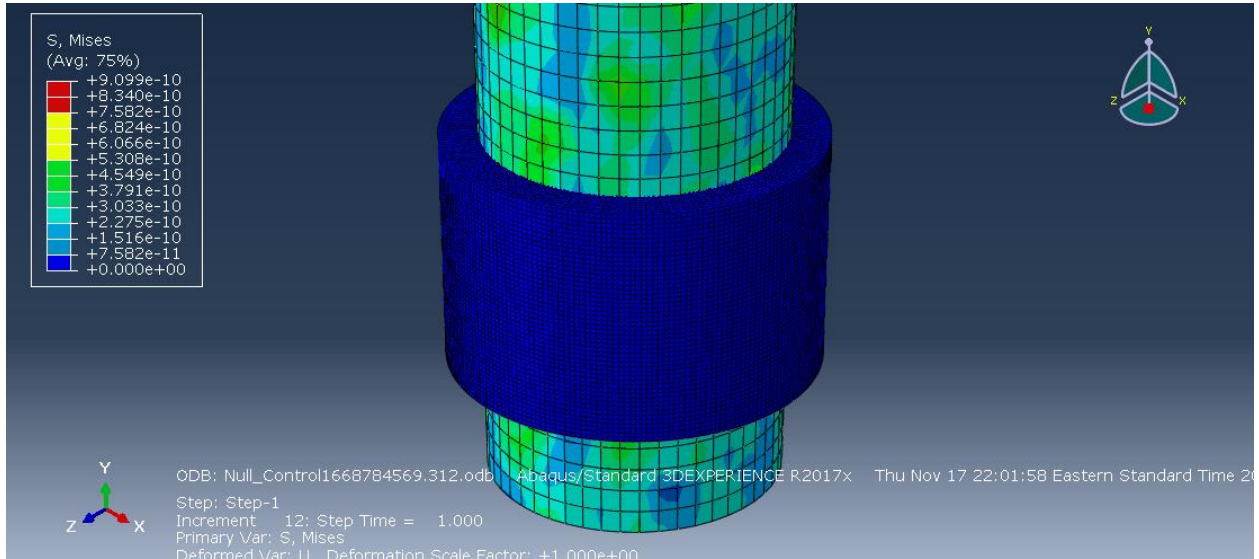


Figure 7: Deformation Map of the Null Control Condition

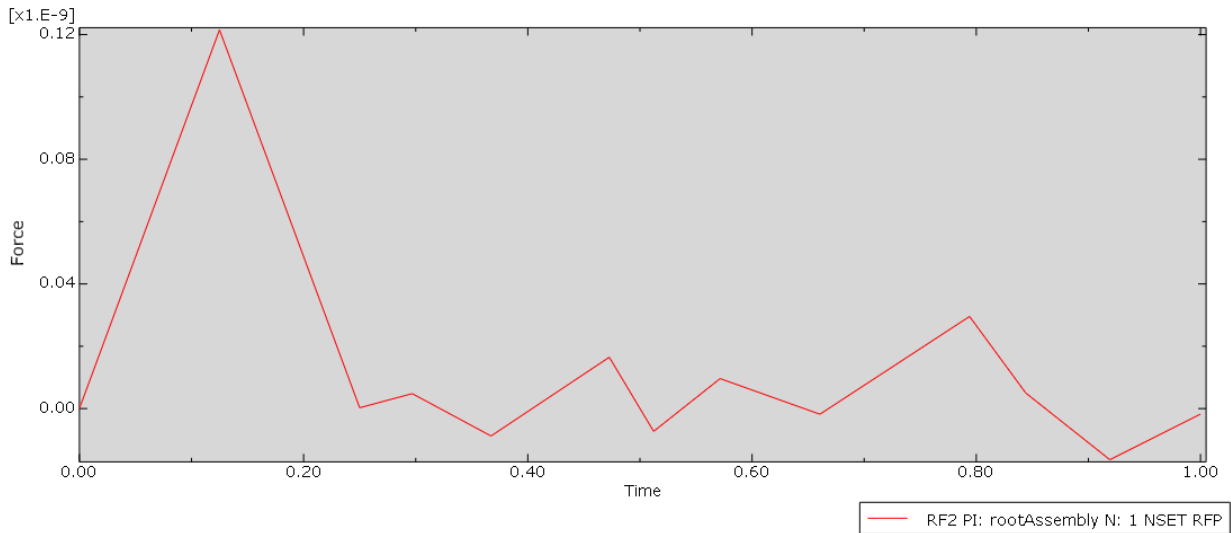


Figure 8: Plot of Friction Force versus Time for the Null Control Condition

The control condition included the induced overlap of 0.0045mm similar to the other experimental conditions. The depicted deformation map (Figure 9) shows expected results, with the deformation taking place in the nylon needle guide rather than the much harder titanium needle. The distribution of deformation shows that the greatest force was experienced at the interface between the needle and the guide, with diminishing friction force moving superficially. The plot of the friction force over time of the Control condition (Figure 10) showed a peak friction force of over 6.0N at the point where the needle tip had just exited the guide and the entire guide was occupied by the needle base (t=0.5s). This is within an appropriate range of the value predicted by the derived equation for the Control values.

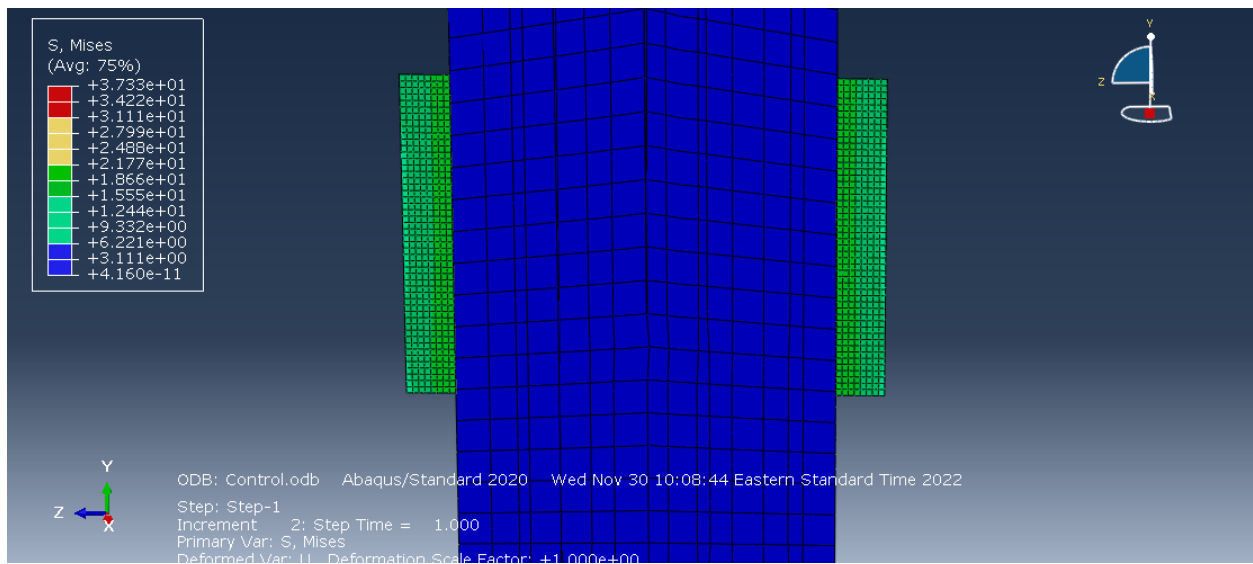


Figure 9: Deformation Map of the Control Condition

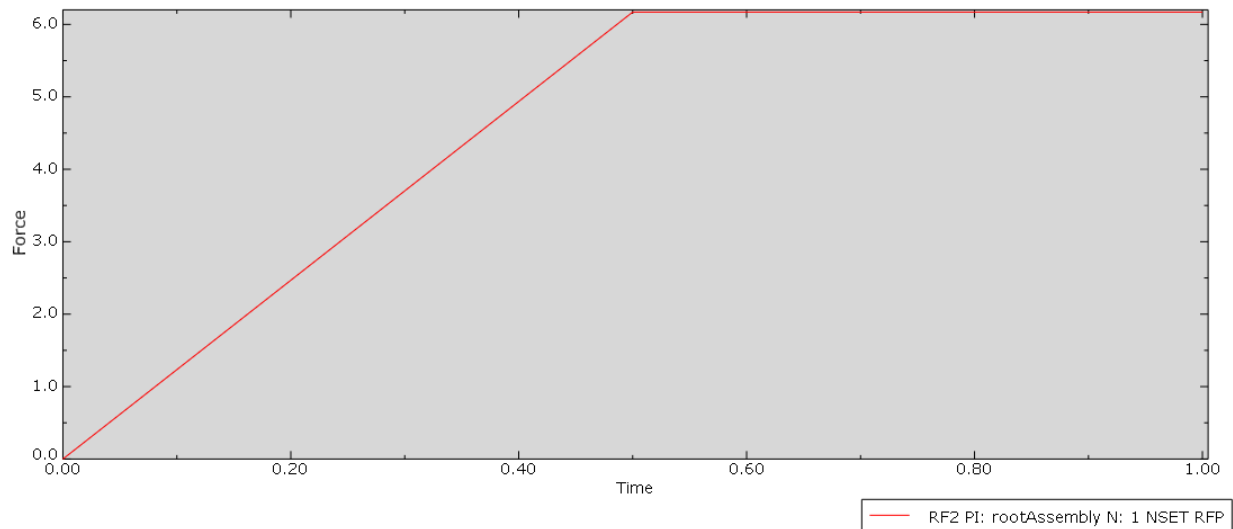


Figure 10: Plot of Friction Force versus Time for the Control Condition

The conditions with ridges oriented perpendicularly to the direction of insertion also followed the theoretical parameters demonstrated by the derived equation. The deformation map of the Perpendicular 5-point condition (Figure 11) showed an expected distribution of friction force, as the contact points experienced the greatest deformation and the reactive force radiated outward away from these points. The plot for this condition (Figure 12) showed a peak friction force of approximately 4.0N, showing a 33% reduction in friction force between these two surfaces compared to the Control condition.

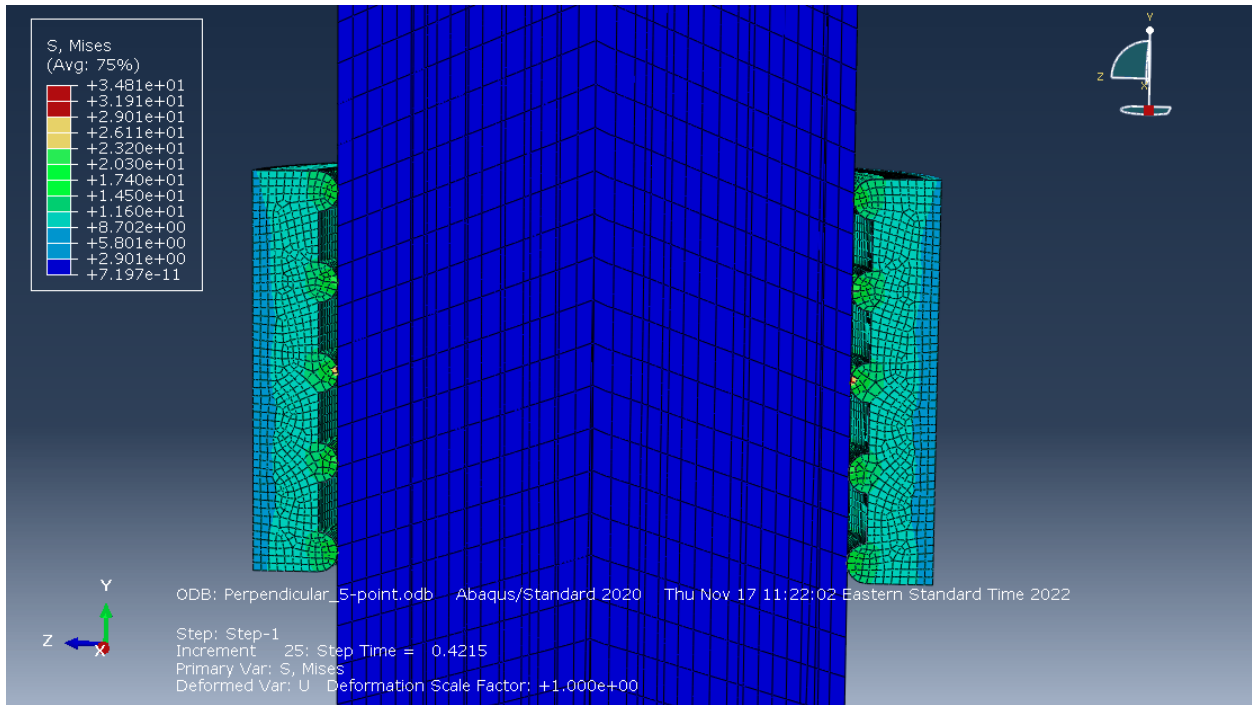


Figure 11: Deformation Map of the Perpendicular 5-point Condition

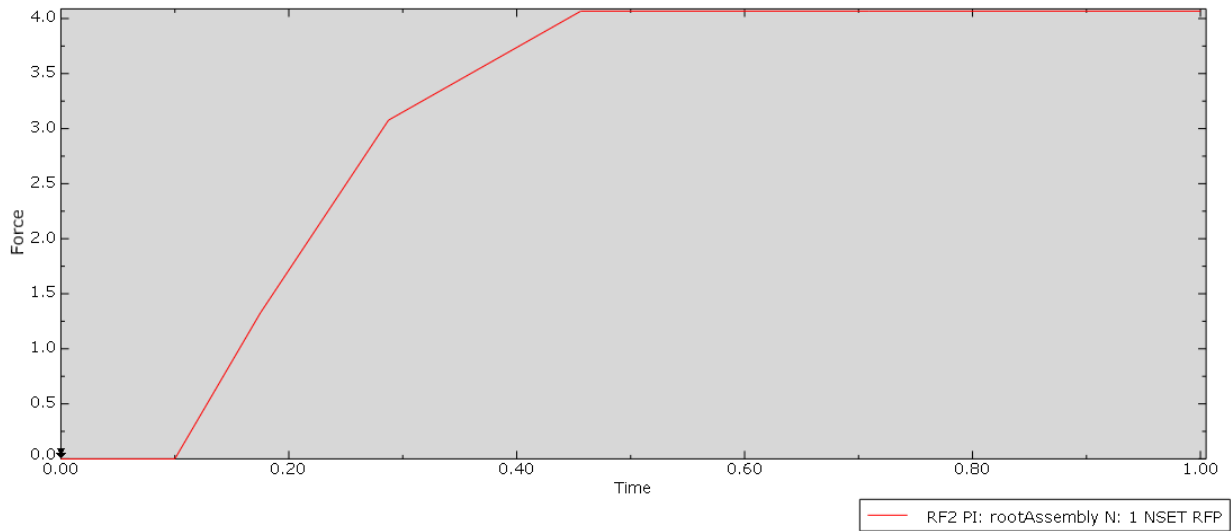


Figure 12: Plot of Friction Force versus Time for the Perpendicular 5-point Condition

The Perpendicular 3-point condition had a lower peak friction force compared to the Perpendicular 5-point condition. The deformation map (Figure 13) similarly showed a reasonable

spread of the stress on the needle guide, with the needle itself not undergoing deformation. However, the plot for the Perpendicular 3-point condition (Figure 14) showed a peak friction force of approximately 1.2N, showing a reduction in friction force of nearly 80% compared with the Control condition. This is consistent with the derived equation, which suggests that a decrease in contact area will result in a lower associated friction force of the interaction.

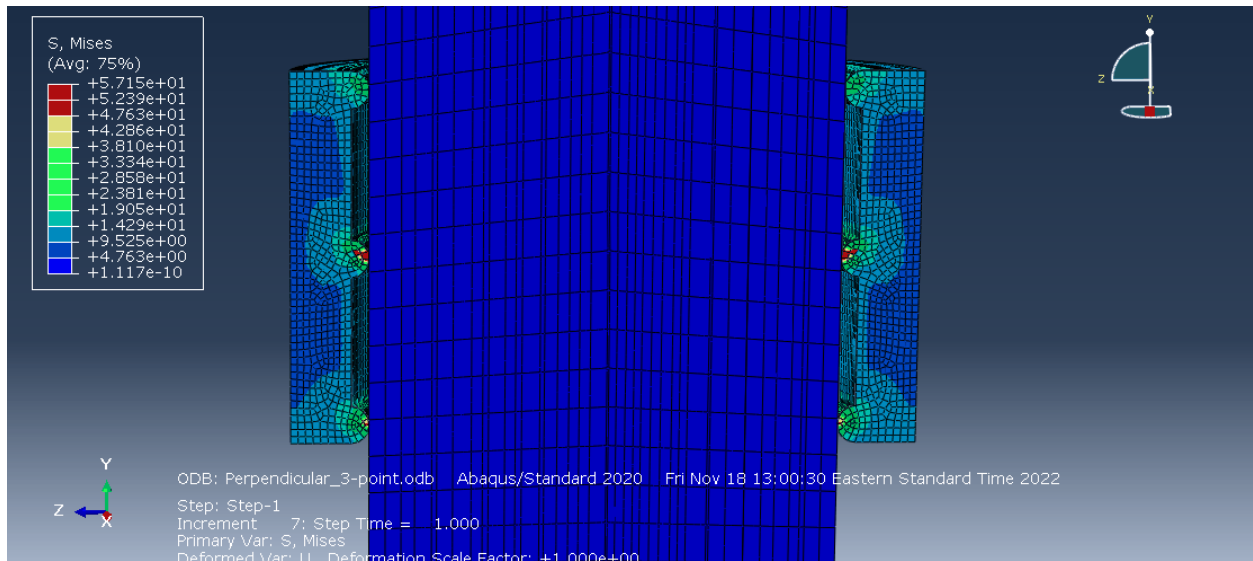


Figure 13: Deformation Map of the Perpendicular 3-point Condition

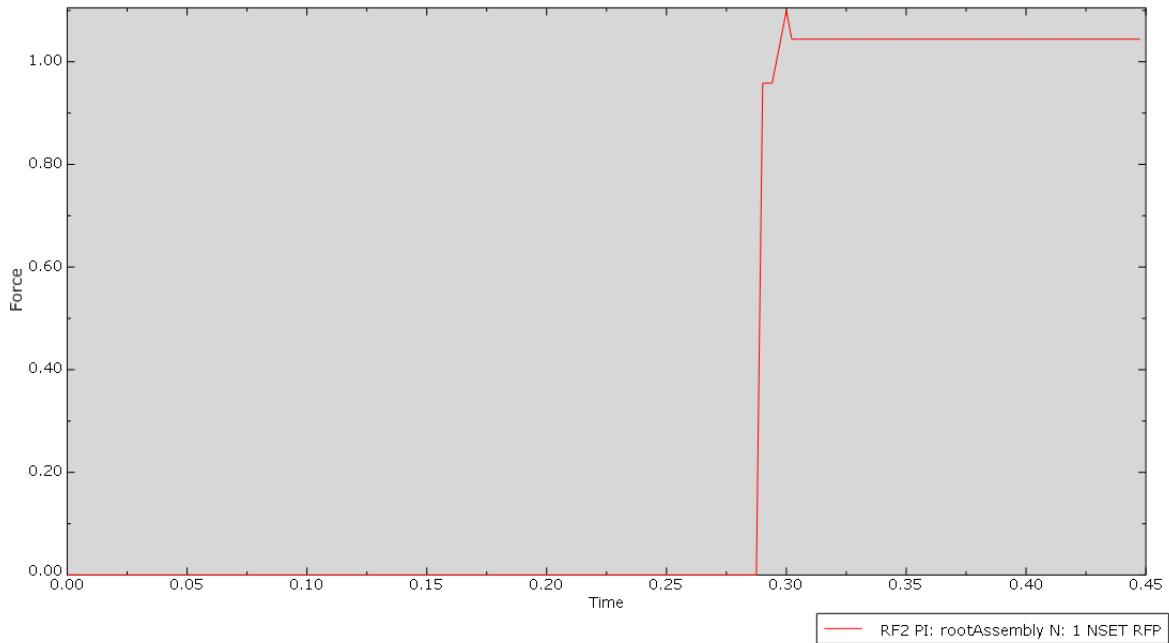


Figure 14: Plot of Friction Force versus Time for the Perpendicular 3-point Condition

Due to the fact that the Perpendicular conditions followed the trend of the derived equation, namely that a lower contact area and number of contact points will yield a lower friction force, the next condition was used to determine the effect of the orientation of the ridges on friction force. Therefore, only a 3-point condition was carried out with the Parallel orientation, as a Parallel 5-point condition would be redundant.

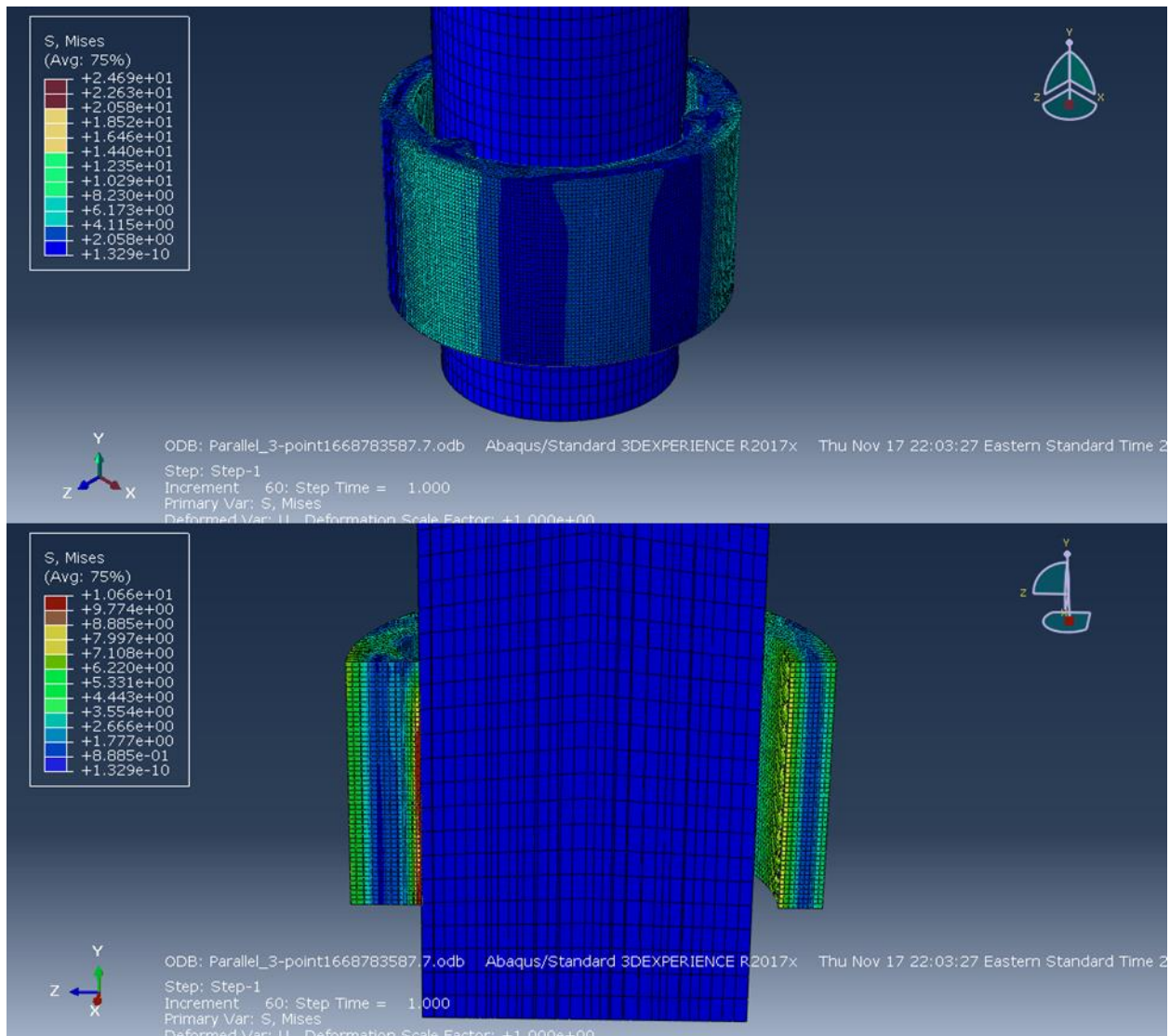


Figure 15: Deformation Map of the Parallel 3-point Condition
 The top image depicts the natural perspective, while the bottom image depicts a cross section of the interaction.

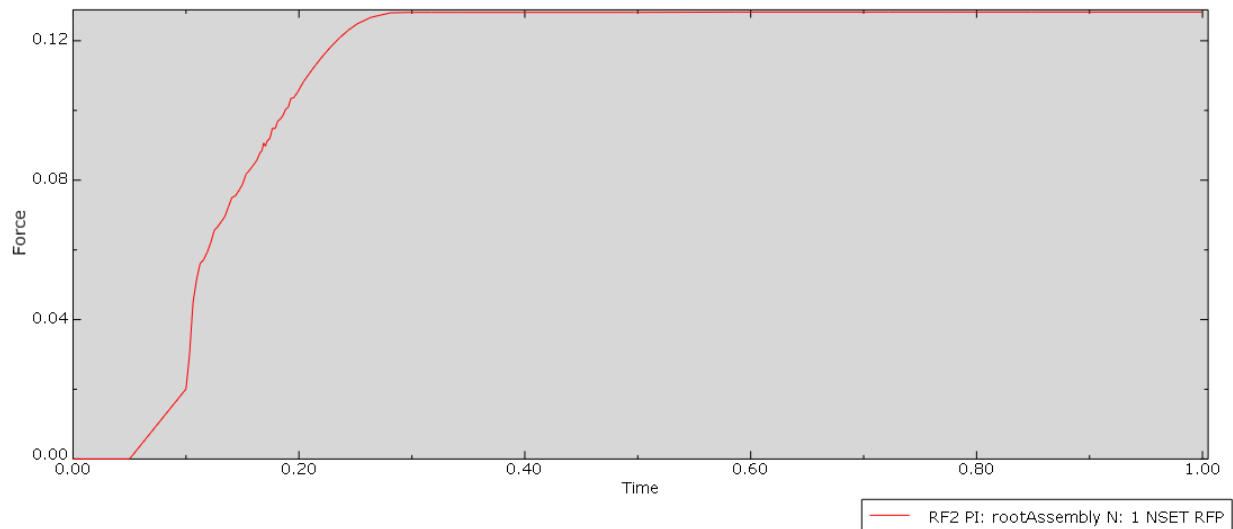


Figure 16: Plot of Friction Force versus Time for the Parallel 3-point Condition

The Parallel 3-point deformation maps (Figure 15) showed a slightly different pattern of interaction between the two objects, as the inner and outer surfaces near the contact areas experienced deformation, while the core of the guide was relatively unchanged. The plot of the friction force over the course of this condition (Figure 16) showed that the peak friction force of this condition was approximately 0.13N. This presents an even greater reduction compared to the previous two experimental conditions, reducing the peak friction force by nearly 98% from the Control condition.

4 Discussion

4.1 Interpretation of Results

This study was done to gather information regarding the interaction between the biopsy template and biopsy needle to optimize core biopsy procedures, specifically transperineal prostate biopsies, and introduce the concept of modifying the needle guide to reduce the friction force associated with the biopsy system.

The purpose of the Null Control condition was to determine if an overlap between the needle and guide needed to be induced in the simulation. A physical needle guide would not be perfect smooth, but contain small deformities on the surface that would translate into several small contact points. The result of the Null Control condition having an order of magnitude of 10^{-9} N demonstrates that these small interactions cannot be similarly simulated in the software, meaning a constant induced overlap between the needle and guide in each condition would need to be created by slightly increasing the diameter of the needle.

The Control condition was used to represent the traditional needle guide currently in use. Though the micro-texture could not be simulated, the slight overlap was used to account for the fact that the two surfaces would not be sliding across one another without resistance. The Control condition will be used as a baseline against which the experimental conditions will be compared to determine if the theoretical reduction in friction force took place. The Control condition saw a peak friction force of approximately 6.0N. This falls within the margin of the derived equation for the control parameters (i.e., 8.43 ± 2.53), suggesting that the methodology in designing the simulation did reflect a true physical scenario. The Control condition had the greatest area of contact between the needle and guide since the entire inner surface was in contact with the needle

(approximately 3.99mm^2 as calculated by Equation 25, the area of an open cylinder). The experimental conditions were expected to have a lower friction force due to the decreased contact area compared with the Control condition.

The Perpendicular 5-point condition produced a peak friction force of around 4.0N and the Perpendicular 3-point condition produced a peak friction force of around 1.2N. This data follows the trend seen in the derived equation which suggested that a lower number of contact points, and therefore a smaller total contact area between the two surfaces, will result in a decreased value for the magnitude of associated friction force. Due to this, the following simulation condition (Parallel 3-point) was performed to assess the effect of a change in orientation of the contact points on the friction force. The Parallel 3-point condition had the lowest resulting friction force of approximately 0.13N. The plots of friction force over time for all the conditions followed a similar trend, in that friction force increased as the needle was being inserted into the guide, and once the body of the needle was completely in contact with the guide the friction force stabilized at a maximum value. According to the derived equation, the decreased friction value of the Parallel 3-point condition was likely due to a decreased overall contact area between the two surfaces when compared to the Perpendicular 3-point model. The average of the friction force over all the experimental conditions was approximately 1.71N, which falls within the margin estimated by the derived equation (i.e., 3.09 ± 1.55). This suggests that the simulation was designed to accurately represent the physical scenario which it intended to simulate.

The area of contact for each ridge in the experimental conditions converts from line contact for area contact as the needle interacts with it due to the deformation of the semicircular ridges. In the perpendicular conditions, the overlap between the two surfaces will cause the ridges to deform so that the contact becomes the area of a rectangle spanning the circumference of the inner surface

of the guide, rather than a line spanning the inner surface of the guide. The area of this contact (Equation 26) can be calculated by the circumference of the inner surface of the needle guide (representing the length of the rectangle) multiplied by the overlap between the two surfaces (representing the height of the rectangle, which converted the contact area from a one-dimensional line to a two-dimensional area). The area of contact for the Parallel condition will be calculated the same way, expect that the length of the needle guide (1mm) will represent the height and the overlap between the two surfaces will represent the width of the rectangular contact area (Equation 27).

$$A_{\perp} = \pi \cdot d_i \cdot \Delta\mu$$

Equation 26: Area of Contact per Perpendicular Ridge

$$A_{\parallel} = l \cdot \Delta\mu$$

Equation 27: Area of Contact per Parallel Ridge

Therefore, the area of contact for each ridge in the perpendicular conditions are calculated to be approximately 0.018mm² per ridge, while the parallel condition had a calculated 0.0045mm² contact area per ridge. The total contact area of each condition is shown in Figure 17. According to these metrics, a plot comparing the contact area versus resulting friction force for the system (Figure 18) can be developed.

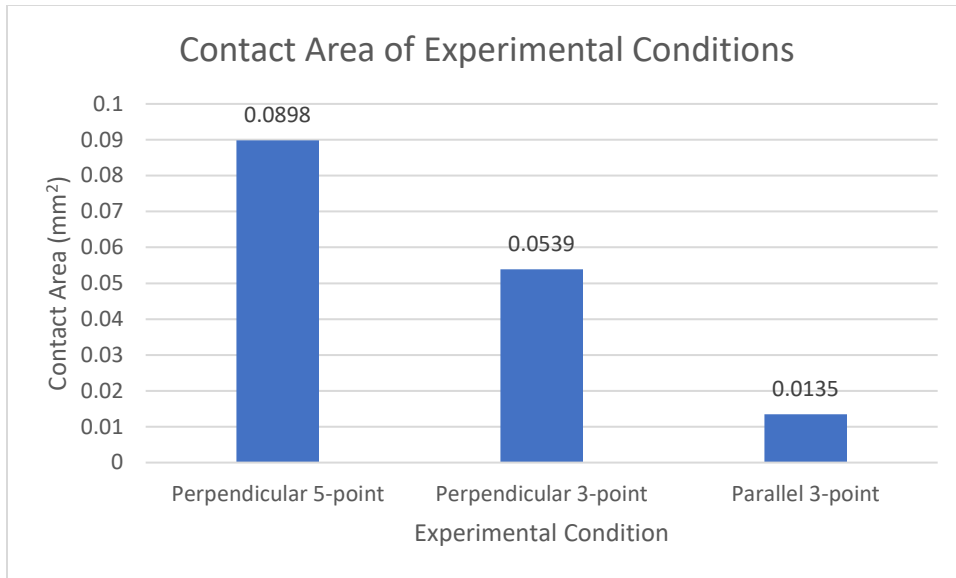


Figure 17: Contact Area of Experimental Conditions

Both of the 3-point conditions had lower contact area than the 5-point condition, but the orientation of the parallel ridges produced a lower contact area than perpendicular ridges.

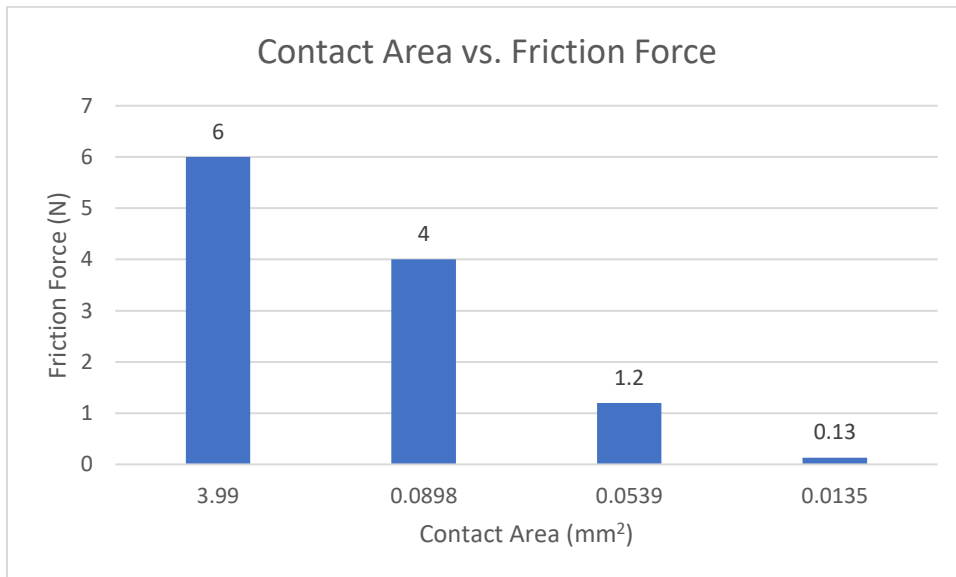


Figure 18: Contact Area vs. Friction Force

There is a correlation between a smaller contact area between two surfaces and a lower resulting friction force at their interface.

The Parallel 3-point condition was able to produce a lower friction force because the orientation of the ridges allowed for a lower total contact area when compared with the

Perpendicular 3-point condition. The Perpendicular 5-point condition had the greatest resulting friction force because of the increased number of contact points, and therefore a greater contact area between the two surfaces when compared with either of the two 3-point conditions. This indicates that the Parallel 3-point condition was the most effective configuration of the internal surface of the needle guide in reducing friction force between the needle and the guide.

4.2 Application

The simulation and mathematical correlation demonstrate that a decreased contact area between two surfaces will result in a lower friction force, and that conditions with ridges oriented parallel with the direction of insertion are advantageous over conditions with perpendicular contact points due to the decreased contact area.

By identifying the biopsy template as an additional source of friction in the biopsy system, friction reduction scenarios can be developed. Reducing the overall friction of the biopsy procedure would produce better quality biopsy cores that may be used for histopathological analysis due to the decreased frequency of fragmentation, decreased tendency for needle deflection due to higher needle insertion velocities, and decreased deformation of the soft tissue which will aid in accurately targeting prostate lesions. Obtaining better quality core biopsy specimens in less insertions would result in less passes being made into the patient, decreasing trauma and the risk for infection.

These unique configurations of the biopsy needle guide may be incorporated into the existing procedure without significant modification of the procedure itself. The needle guides may be manufactured by injection molding using nylon material to precisely create the internal surface pattern within such small dimensions. The template grid itself may be manufactured with the

ability to exchange the needle guides so that as the needle guides are used over time and the ridges experience deformation, then may simply be removed and replaced with new guides to maintain the original tightness to the needle. The nylon material of the needle guides also makes them compatible with MRI guided biopsy procedures. This same concept can be applied to core biopsy procedures of multiple anatomical structures, including renal and breast biopsies.

When applying the optimization of the needle guide in this manner, there are sacrifices that will be made in exchange for this reduction in friction force. An additional component to the procedure would need to be manufactured, sterilized, and delivered to the healthcare provider, which introduces additional cost. The incorporation of an additional component may also slightly increase the length of preparation for the procedure and could introduce the opportunity for user error.

The simulation examined 5-point and 3-point contact models in the experimental conditions, and the 3-point models were intended to suggest the minimum amount of contact points necessary to maintain the tightness of the needle to the guide while introducing the lowest friction. Both accuracy and insertion velocity are separately and inversely affected by the tightness of the needle to the guide, and though the direct relationship between these two variables was not examined in this study, the effect of the distribution of contact points may be significant factor affecting this. Assuming the orientation of the contact points that produces the lowest friction force possible, a greater number of contact points will increase accuracy and reduce insertion velocity, while a lower number of contact points will increase insertion velocity without necessarily reducing accuracy unless below a threshold number of contact points. Since the needle is a rigid object, there exists a minimum number of contact points that will maintain substantial contact between the two surfaces that will prevent bending and movement of the needle during insertion,

which presents a future area of study. This study only examined the effects of longitudinal ridges as contact points on friction force, but a series of dot contact points would follow the trend of decreasing contact area according to the derived equation. By clustering a series of dot contact points near the entry and exit site of the needle guide, there may be sufficient interaction so as to maintain tightness and reduce the contact area even more significantly than ridges along the inner surface.

4.3 Limitations and Future Study

The study was carried out as a simulation rather than an *ex vivo* study, which has certain limitations in its parameters. The Control condition in the simulation was intended to represent the current needle guide design. However, the Abaqus software is unable to simulate the roughness and microridges present in the physical needle guide. This was shown through the application of the Null Control condition, and the necessity of applying a slightly larger diameter to the needle. Though the friction force indicated by the simulation of the Control condition was within the margin estimated by the derived equation, the Control condition itself did not reflect the exact roughness found on materials naturally.

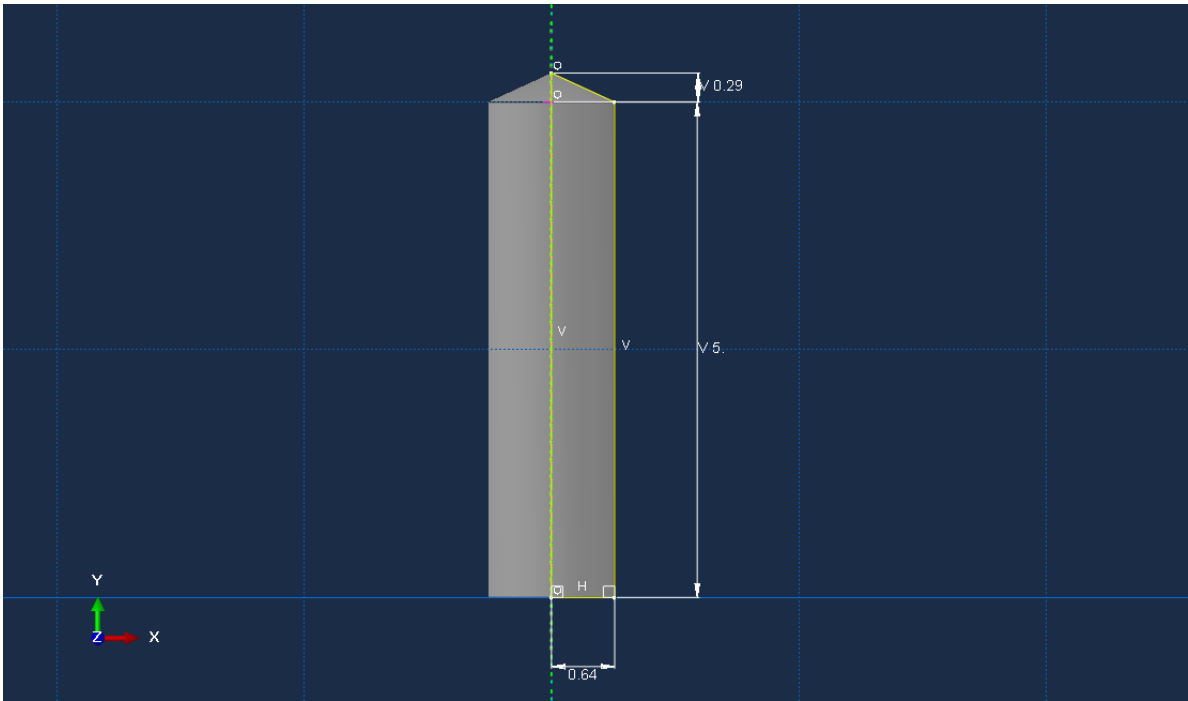
An additional limitation of the simulation method is that the needle was inserted through the needle guide exactly along the y-axis as specified. In a physical scenario, the clinician performing the biopsy will undoubtedly insert the needle slightly deviated from this axis, producing nonaxial forces. This simulation was unable to examine the effects of nonaxial forces on the configurations of the needle guide and the resulting friction force. This concept may be examined in a future study.

The study was interested in introducing the needle guide as a source of friction that has been overlooked in the optimization of the core biopsy procedure. As a result, the simulations were designed with the intent of comparing friction force when the number and orientation of contact points was modified. This simulation did not examine the relationship between needle stability and insertion velocity. A decreased contact area was shown to reduce friction force upon the needle, but a baseline amount of contact is needed to maintain the accuracy of the needle as it is being inserted. This consideration may reveal an optimal range for the total contact area of the system examined in this study.

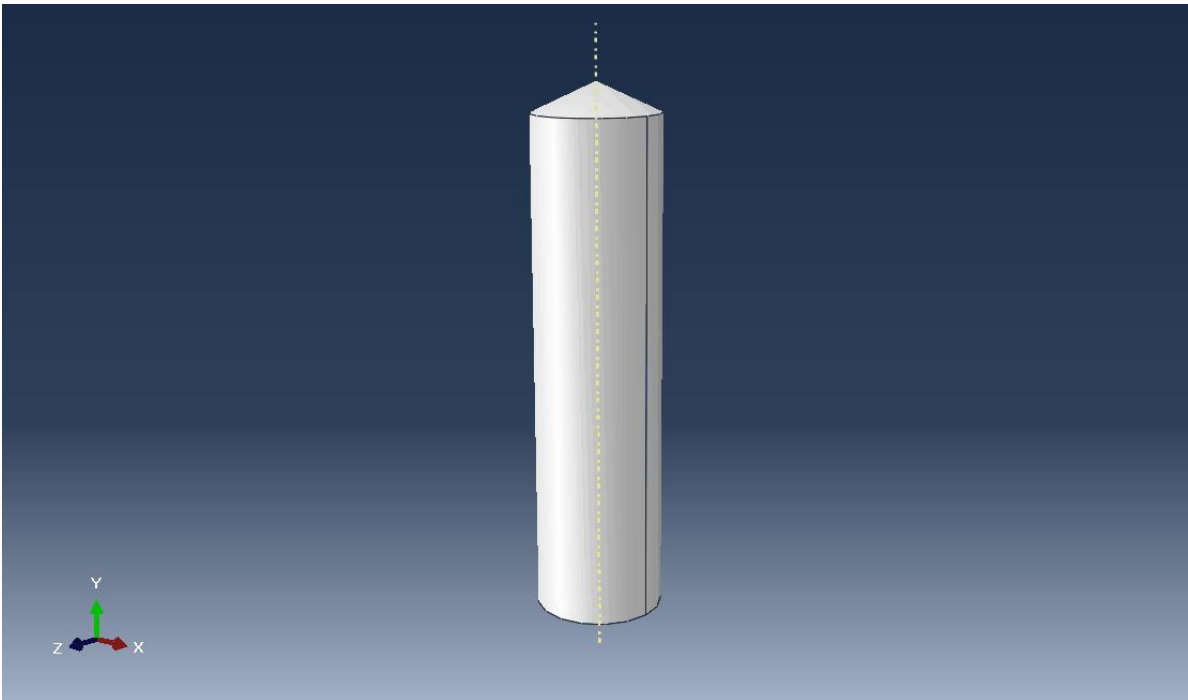
The study was designed to test the Perpendicular conditions first, and if the results of these conditions followed the trend shown by the derived equation (namely that as contact area decreases, friction force will decrease), then the effects of the orientation of the contact points will be assessed by performing a single Parallel 3-point condition. One area of future study could be to examine the effects of a wider variety of contact points on friction force, such as including a Parallel 5-point condition or studying the effects of different geometric configurations along the inner surface of the needle guide.

Finally, a total of five conditions were examined in this study. While these conditions were sufficient in demonstrating the advantage of certain configurations of the needle guide over the traditional model, there were not enough data points to assemble a comprehensive plot showing the change in friction force as contact area is increased. Such a plot may show a nonlinear relationship between these two characteristics that suggest a certain total contact area will be most beneficial when aiming to reduce friction force.

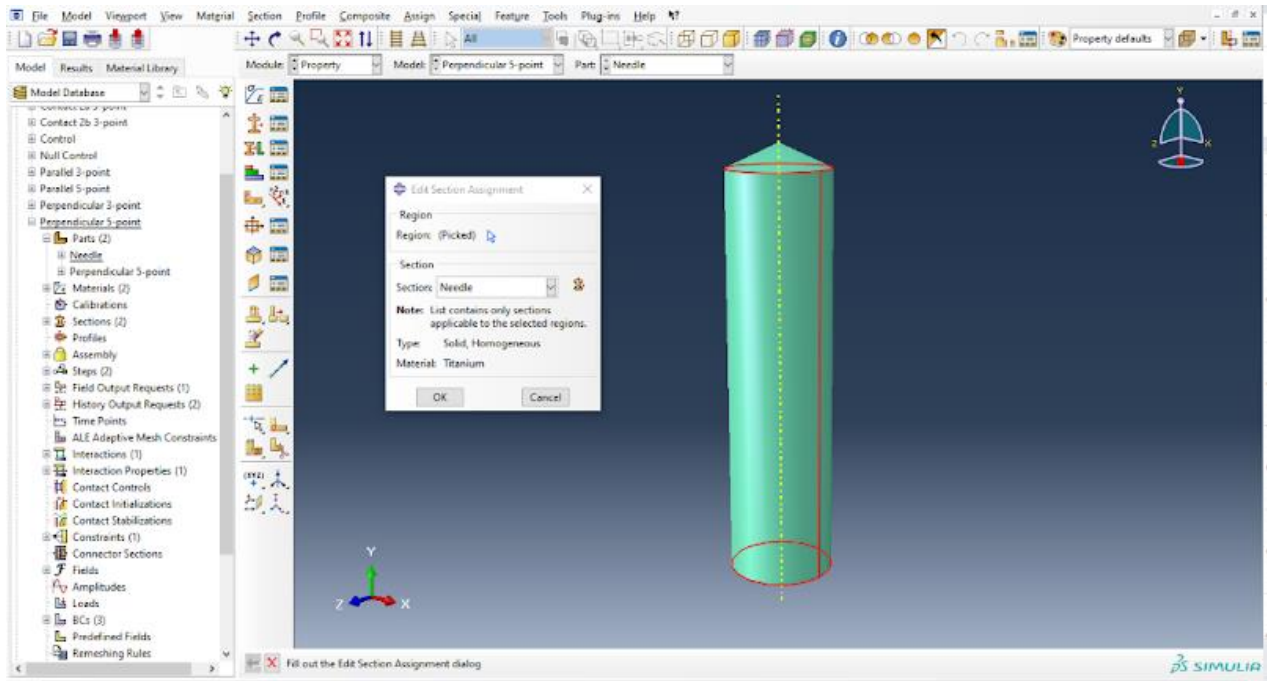
Appendix A: Null Control Simulation Methodology



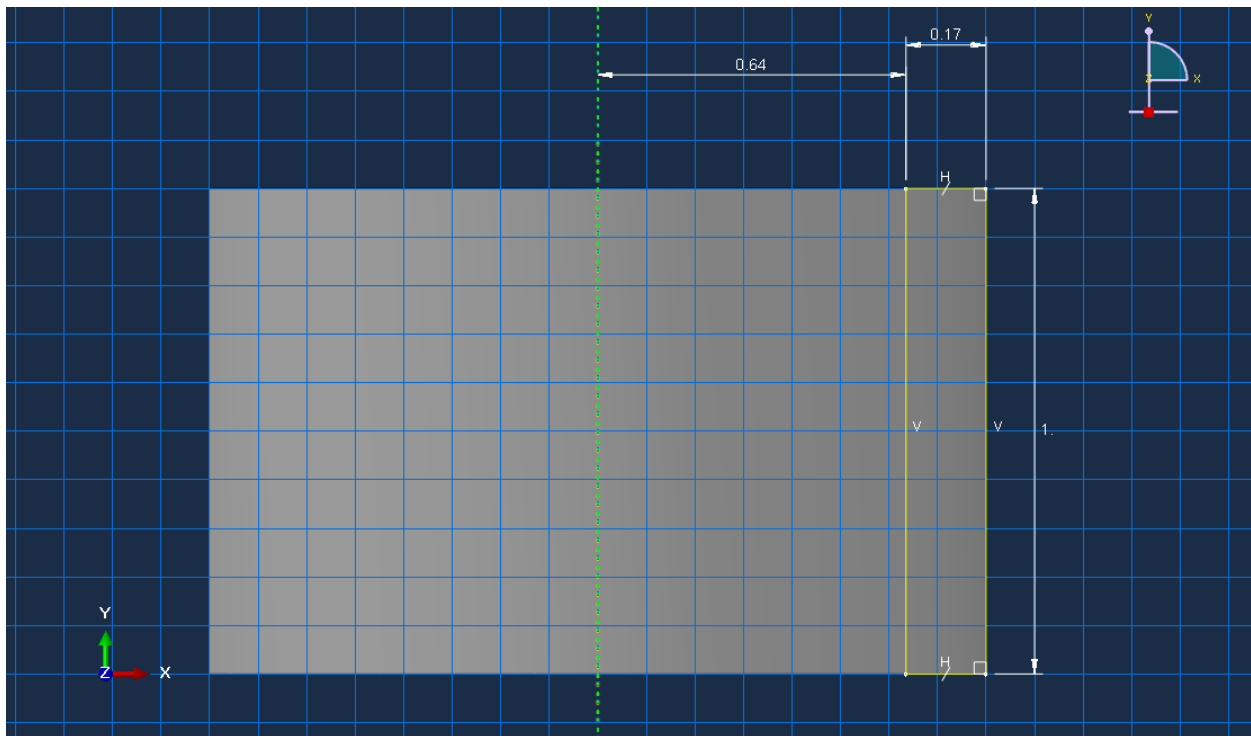
Appx. A. Figure 1: Needle Dimensions



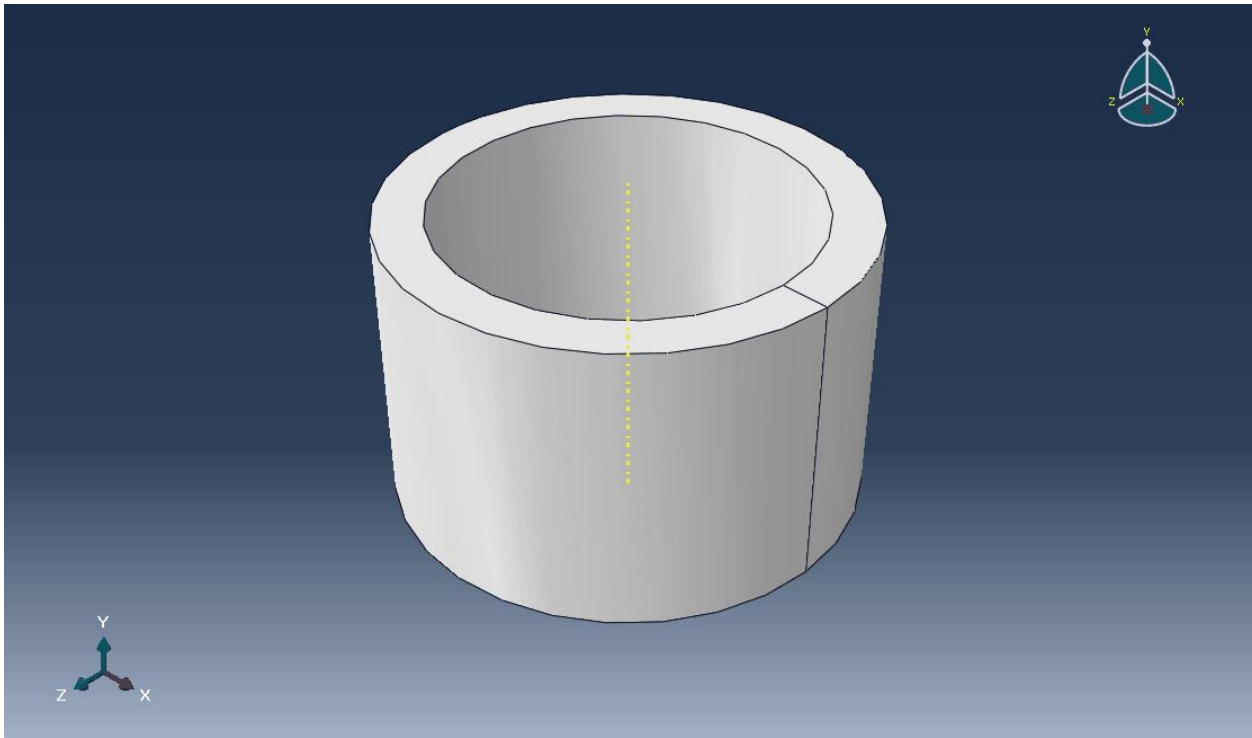
Appx. A. Figure 2: Needle Part Image



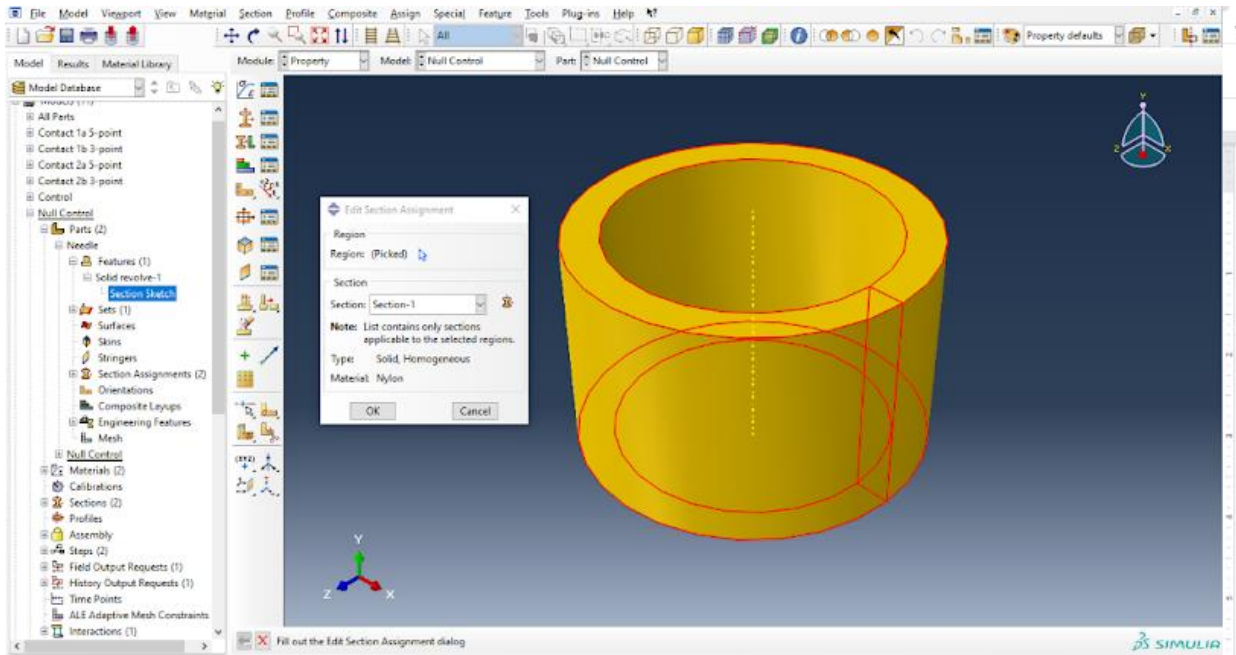
Appx. A. Figure 3: Needle Material Property



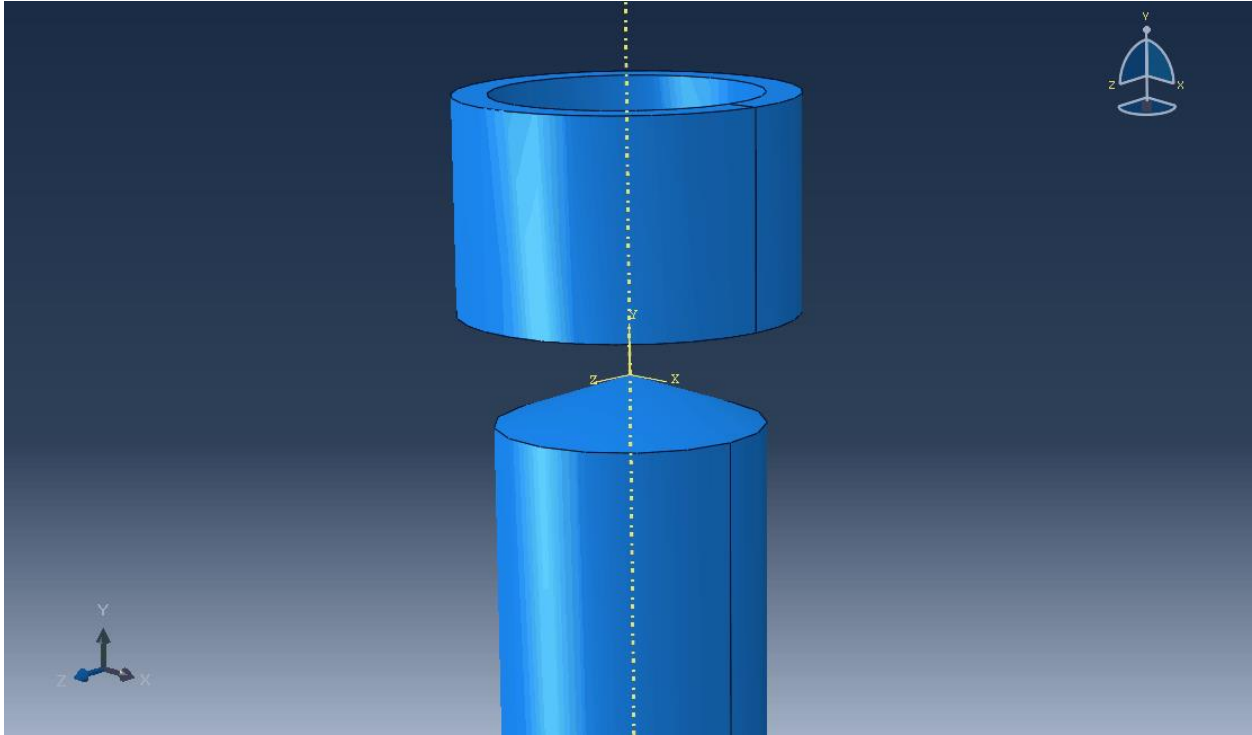
Appx. A. Figure 4: Null Control Dimensions



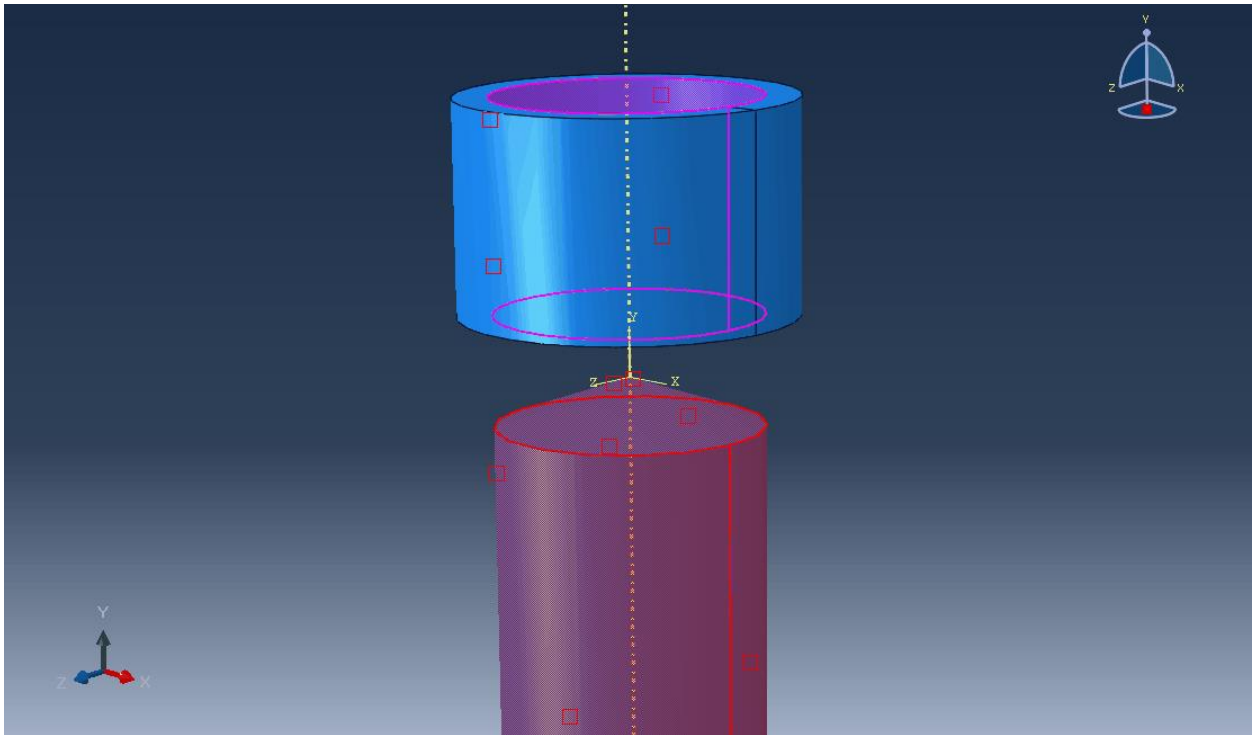
Appx. A. Figure 5: Null Control Part Image



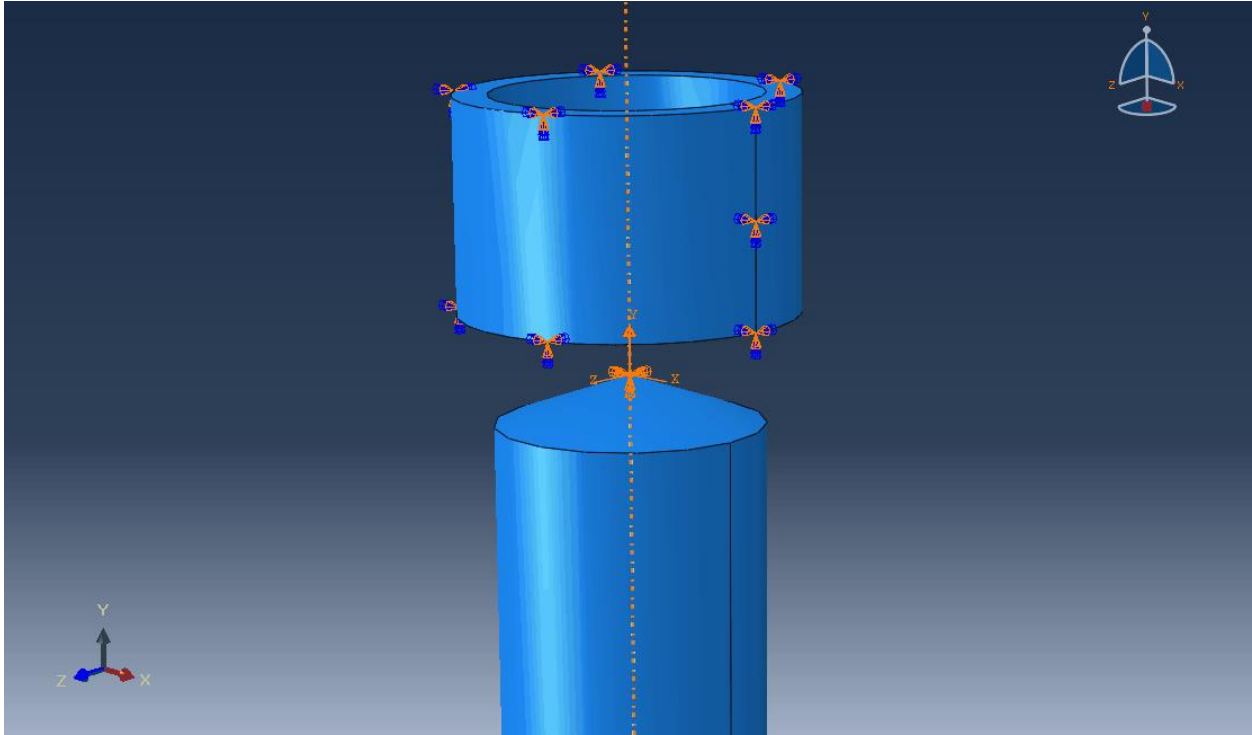
Appx. A. Figure 6: Null Control Material Property



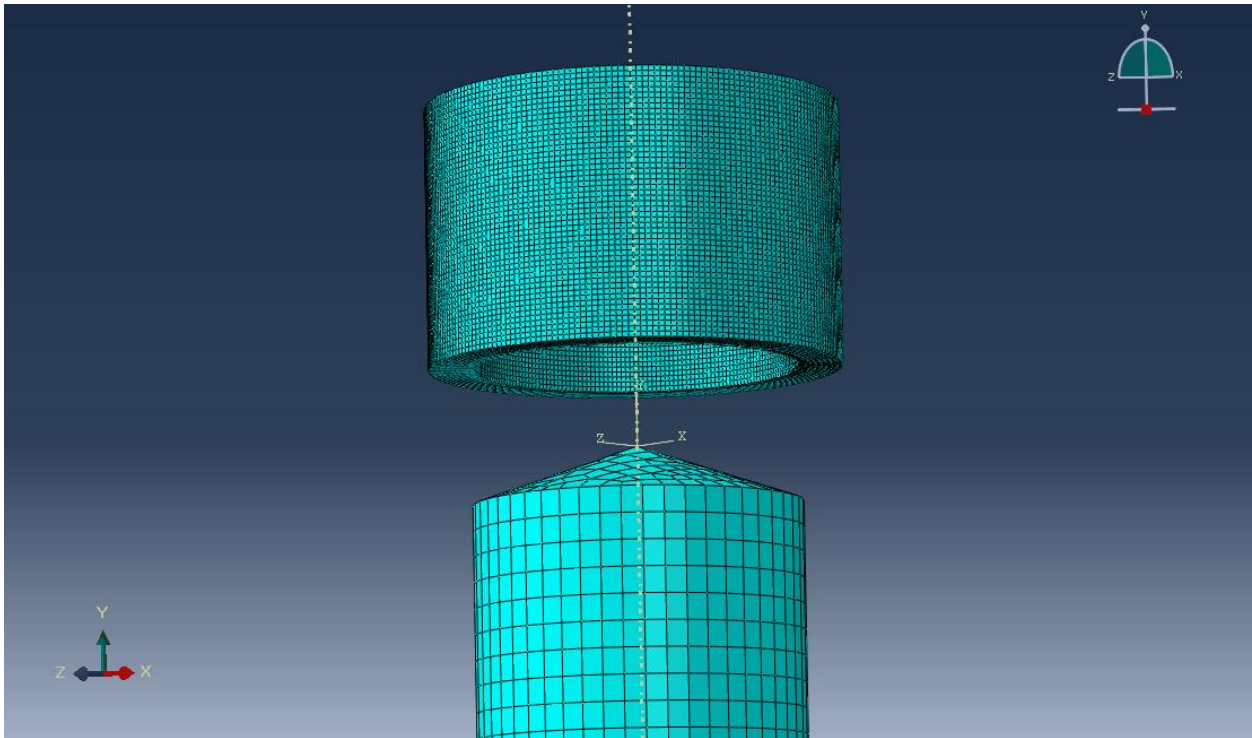
Appx. A. Figure 7: Null Control Assembly



Appx. A. Figure 8: Null Control Interaction

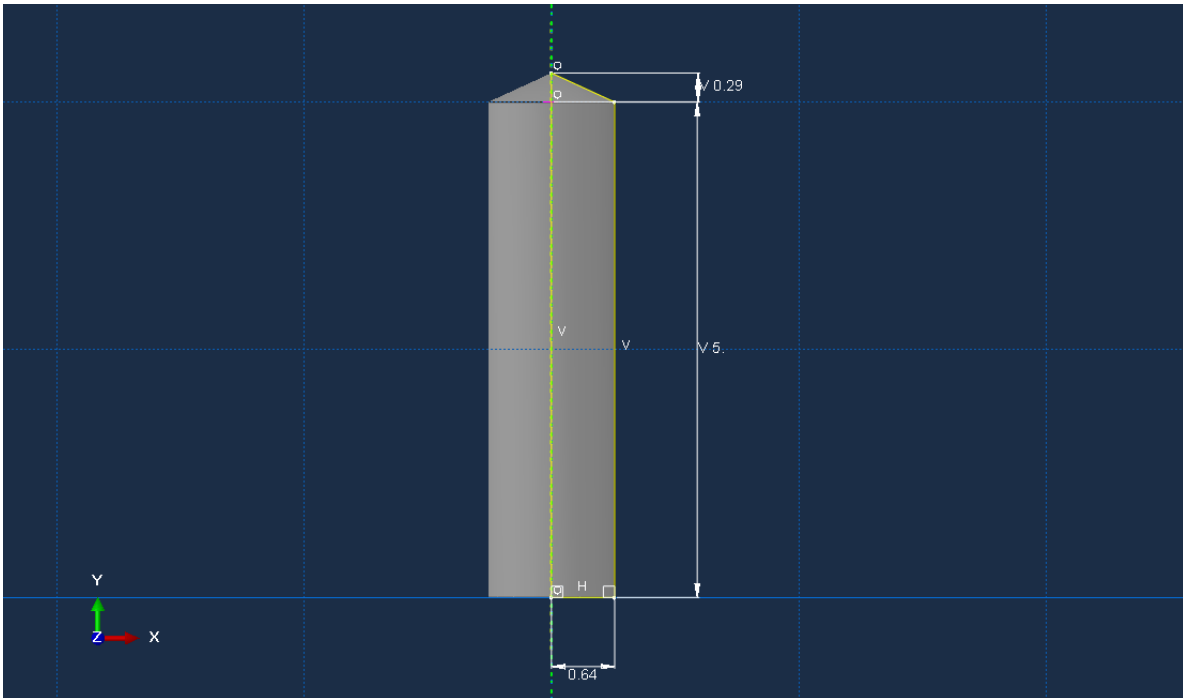


Appx. A. Figure 9: Null Control Boundary Conditions

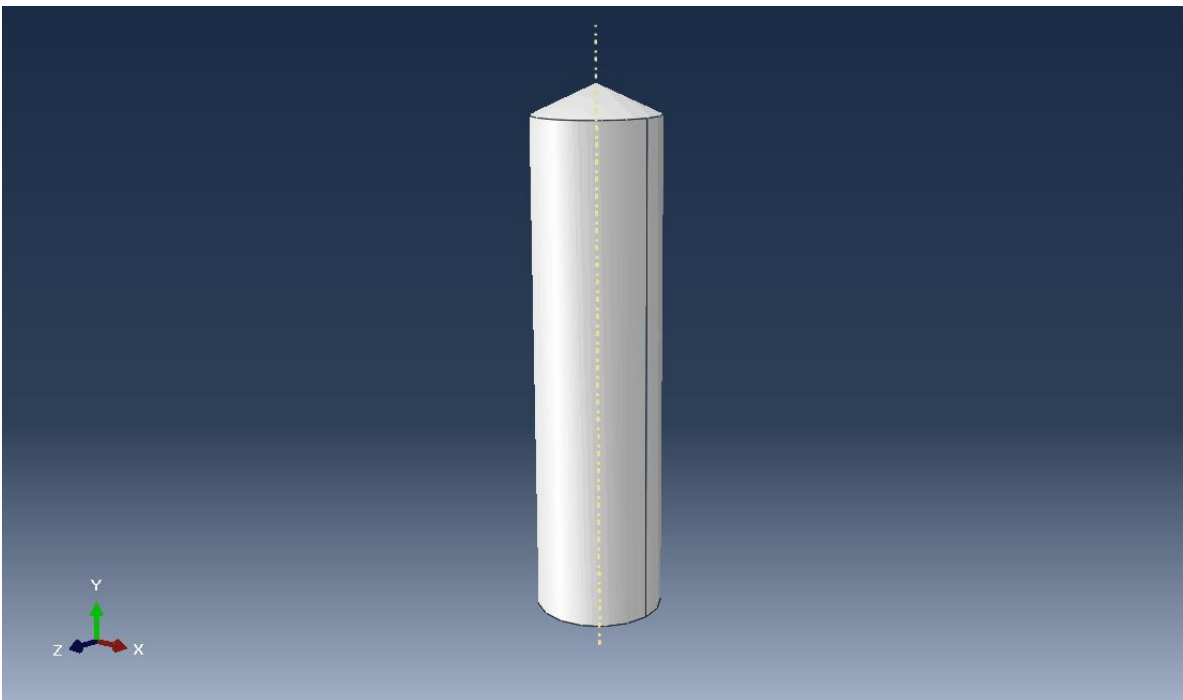


Appx. A. Figure 10: Null Control Mesh

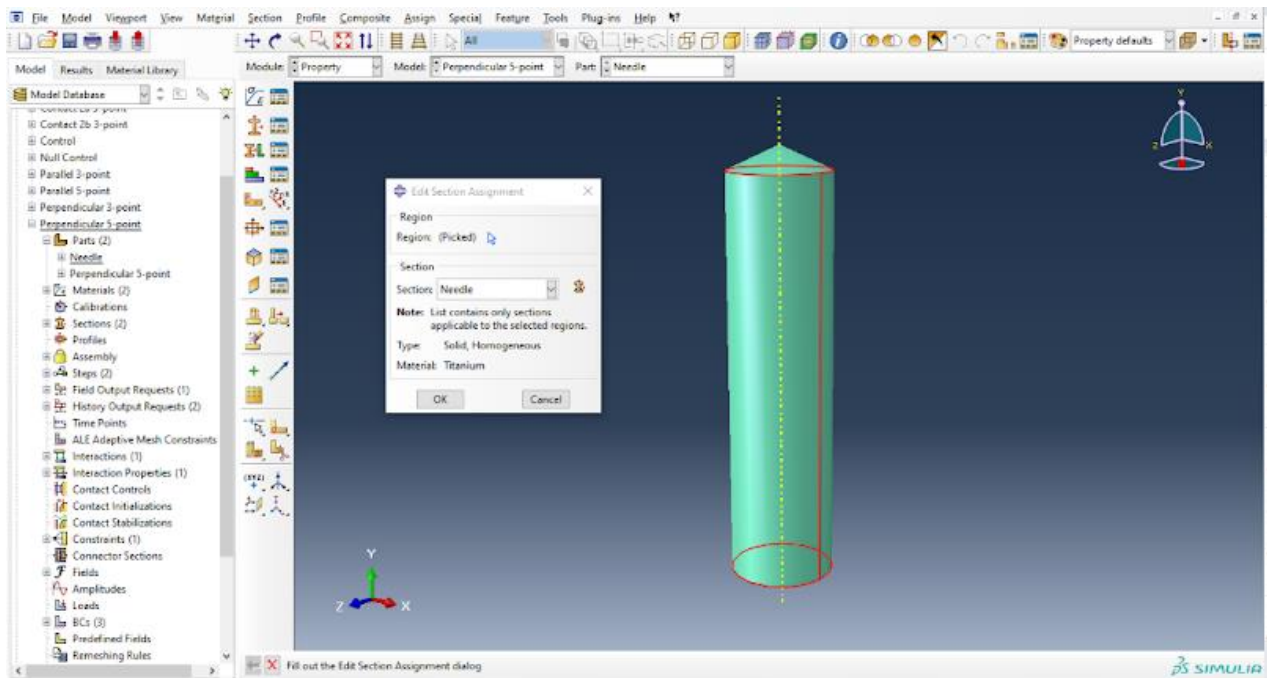
Appendix B: Control Simulation Methodology



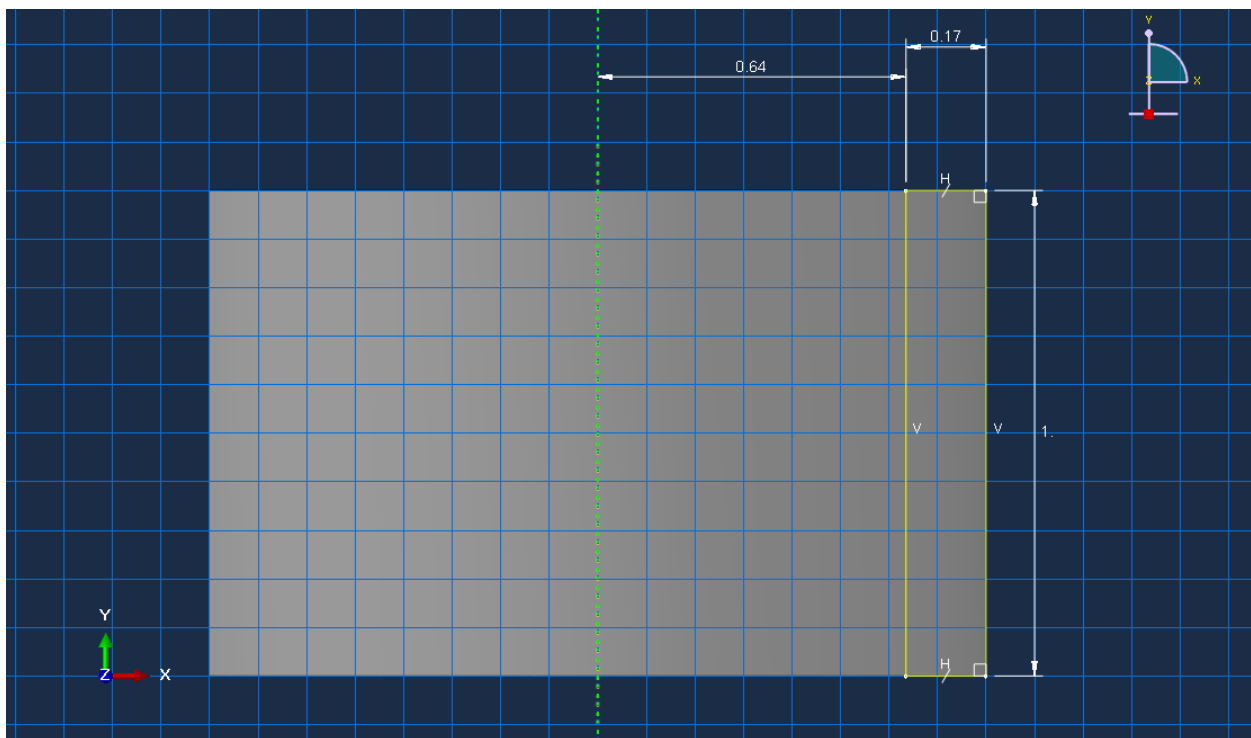
Appx. B. Figure 1: Needle Dimensions



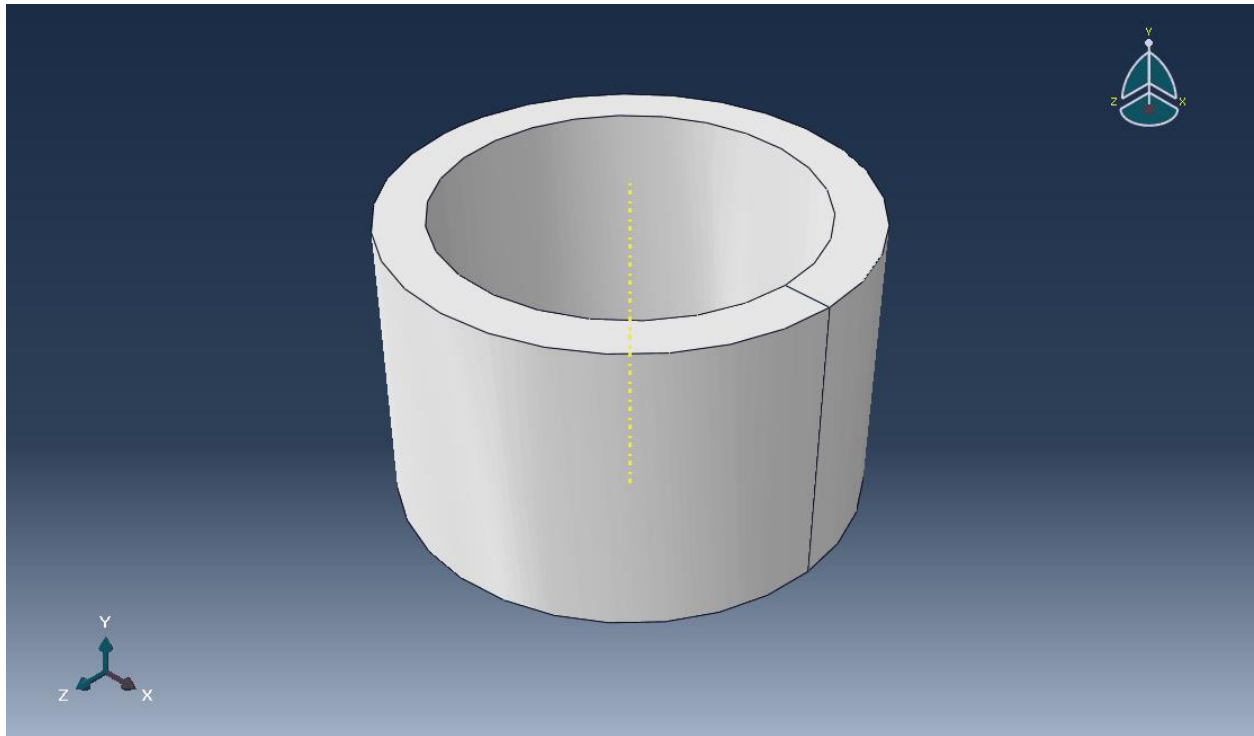
Appx. B. Figure 2: Needle Part Image



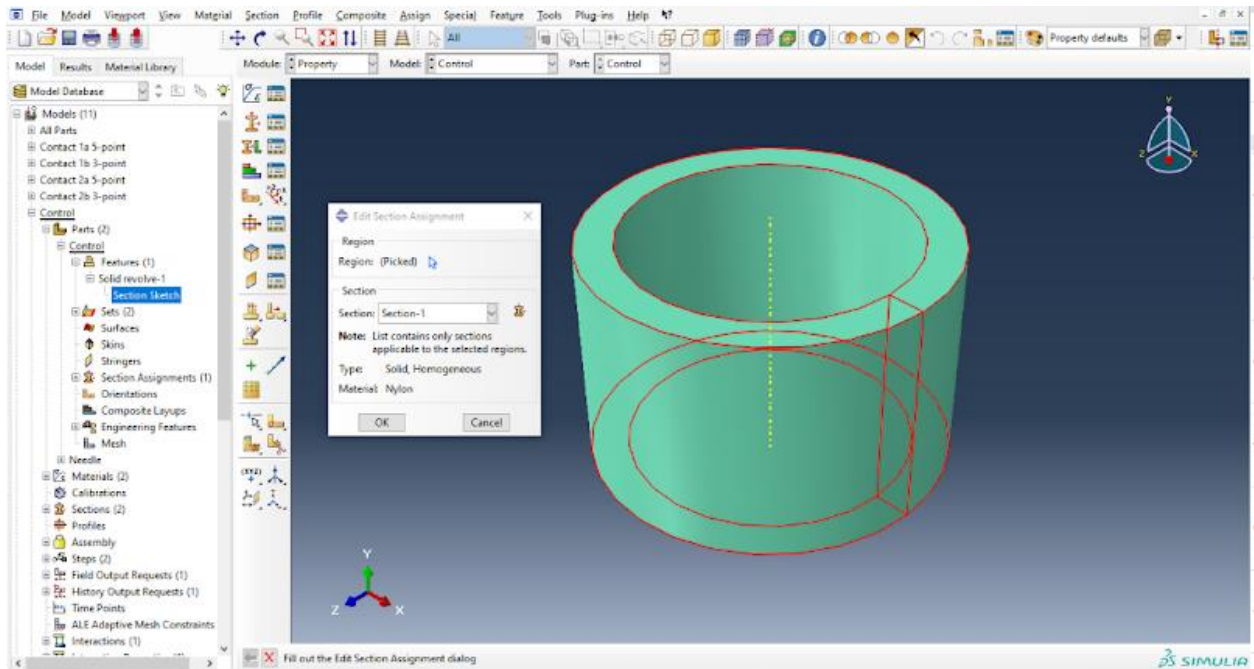
Appx. B. Figure 3: Needle Material Property



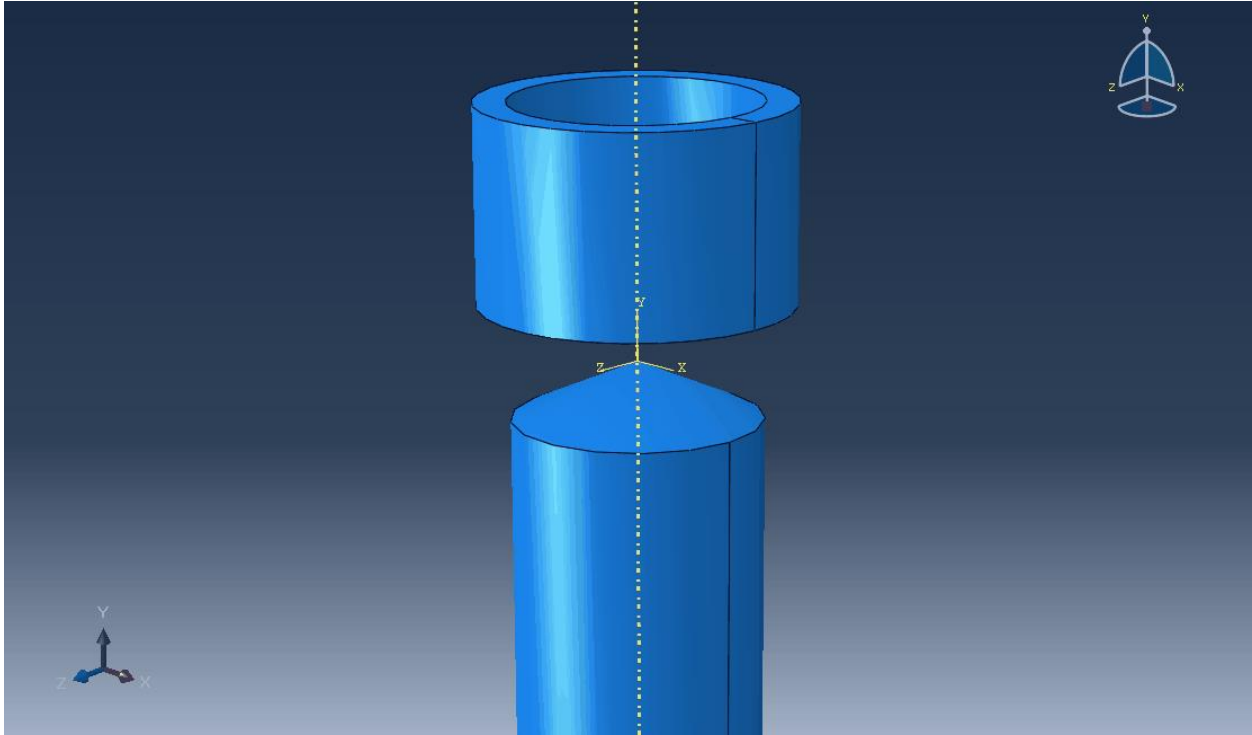
Appx. B. Figure 4: Control Dimensions



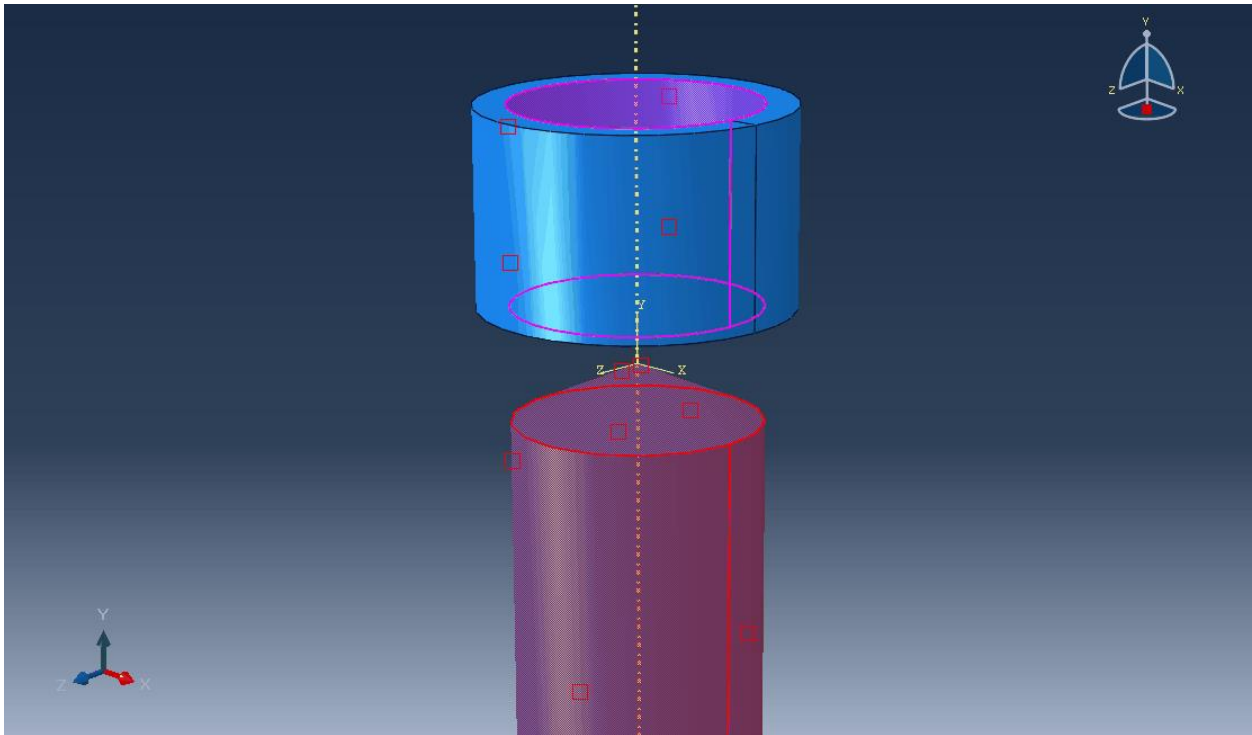
Appx. B. Figure 5: Control Part Image



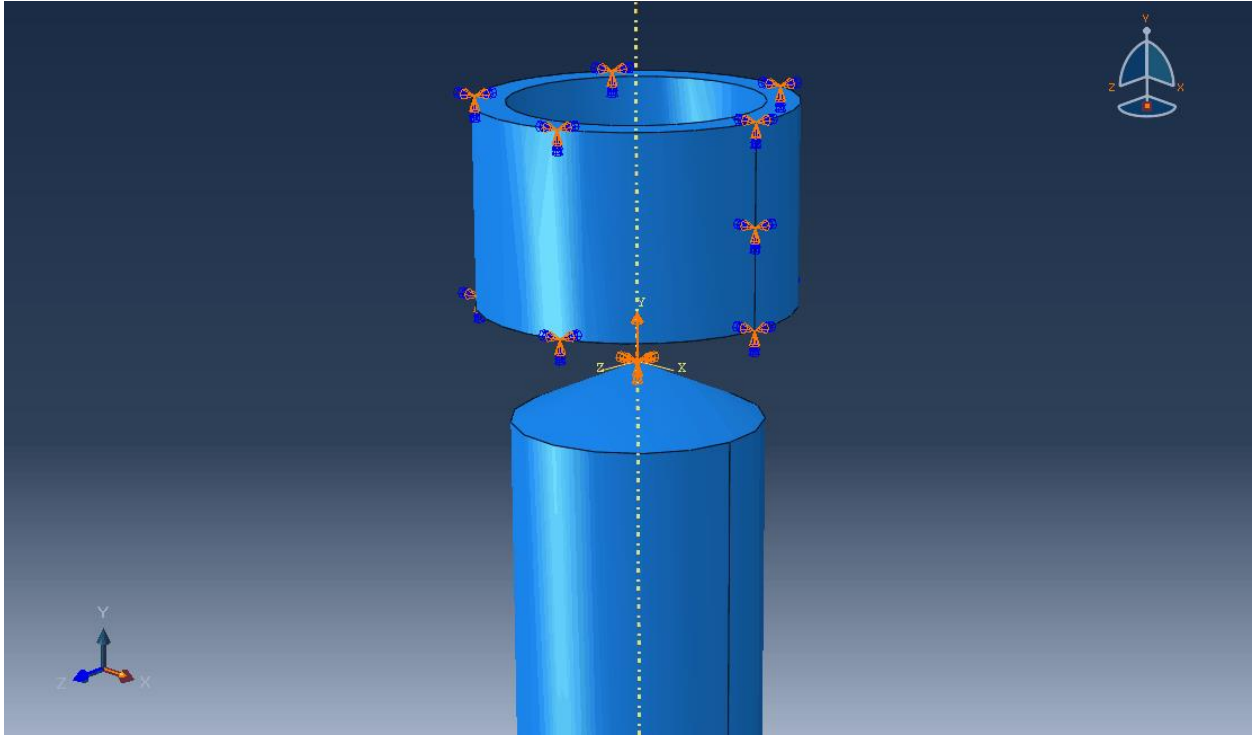
Appx. B. Figure 6: Control Material Property



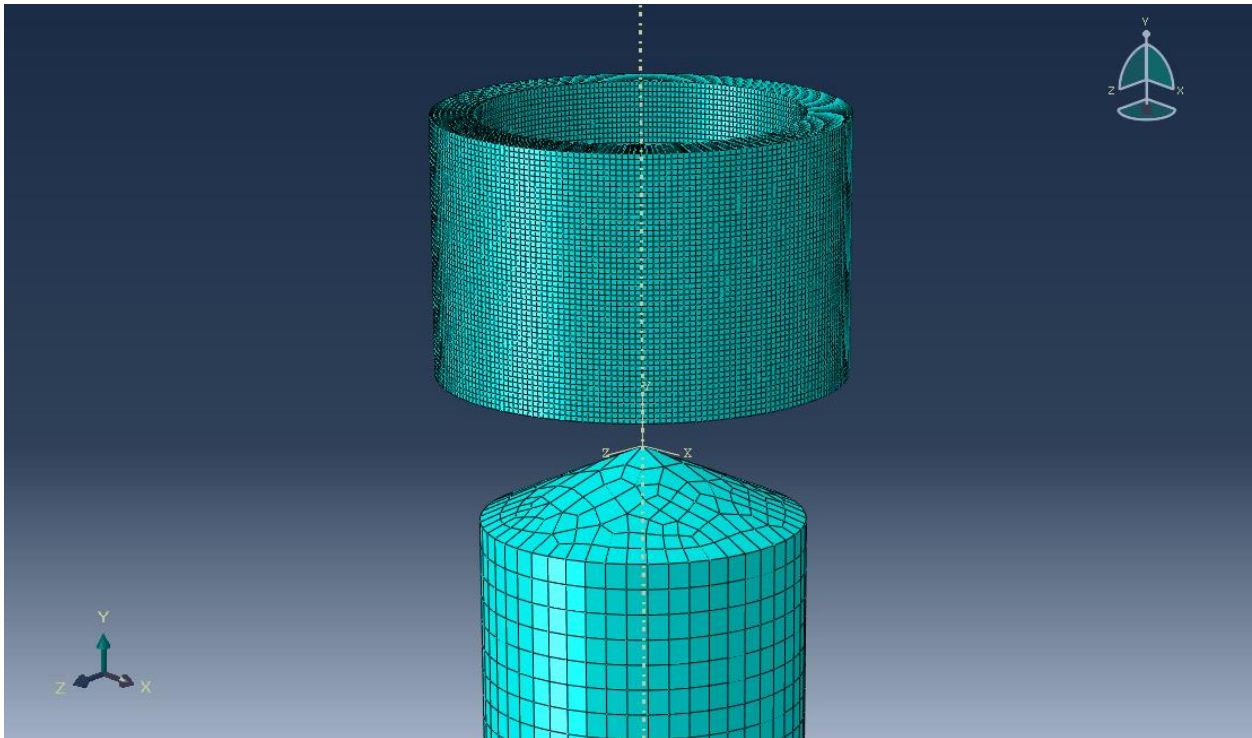
Appx. B. Figure 7: Control Assembly



Appx. B. Figure 8: Control Interaction

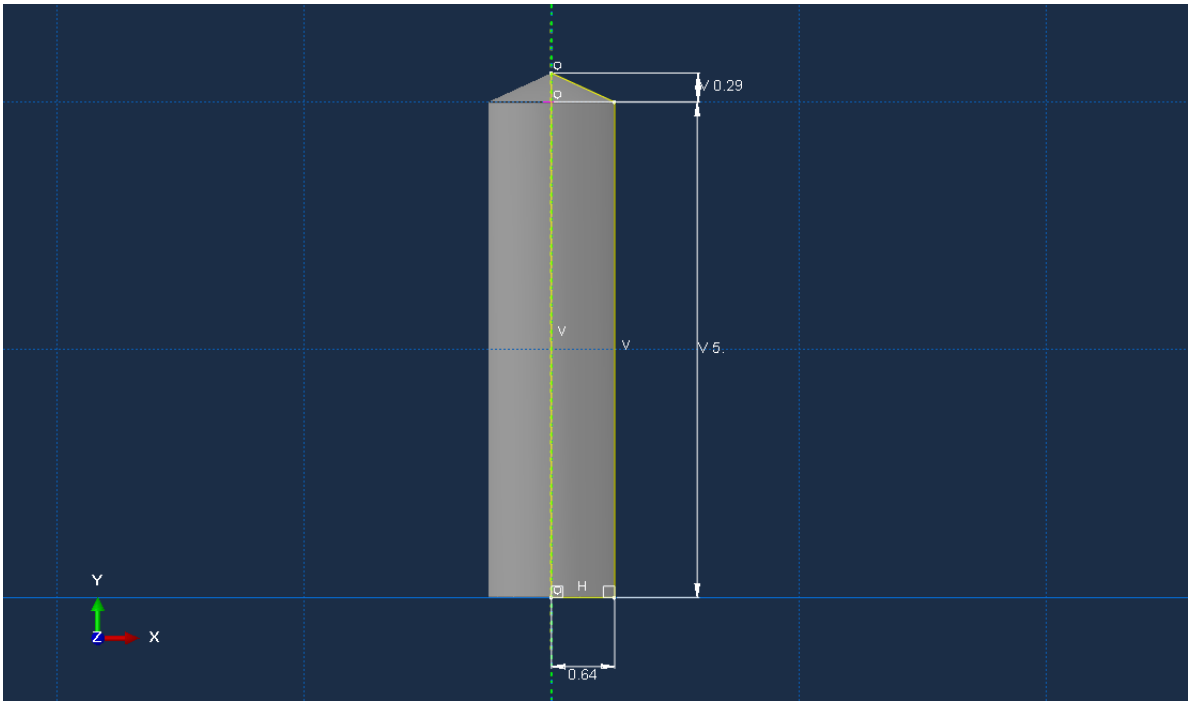


Appx. B. Figure 9: Control Boundary Conditions

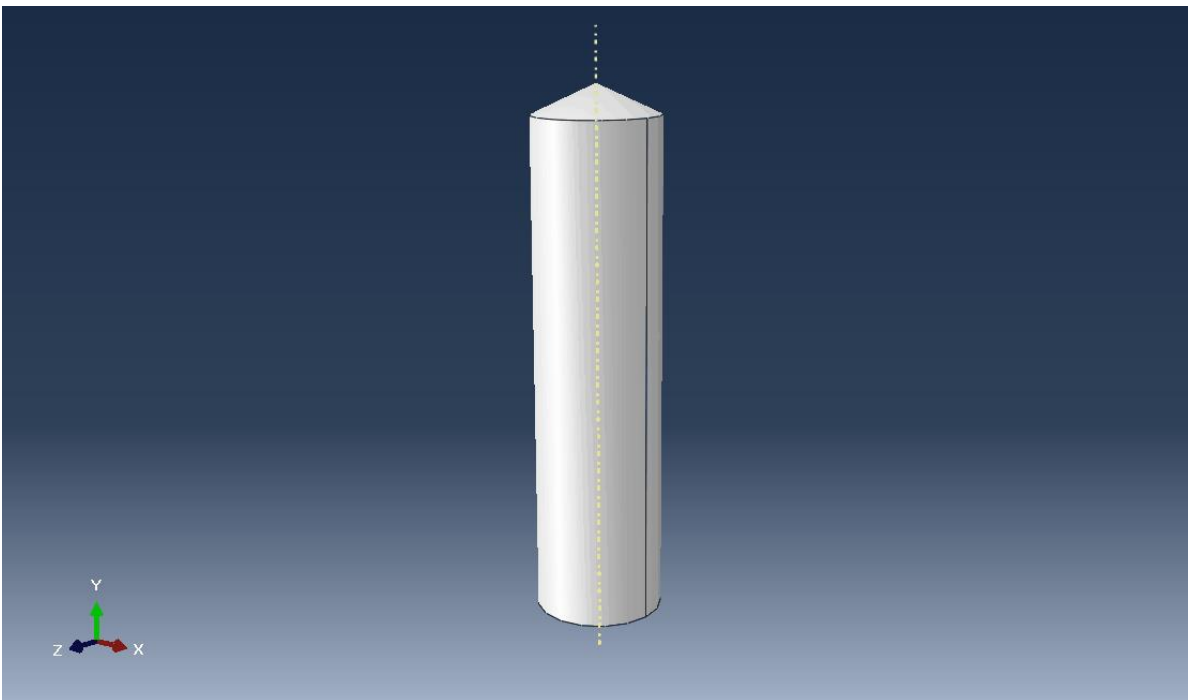


Appx. B. Figure 10: Control Mesh

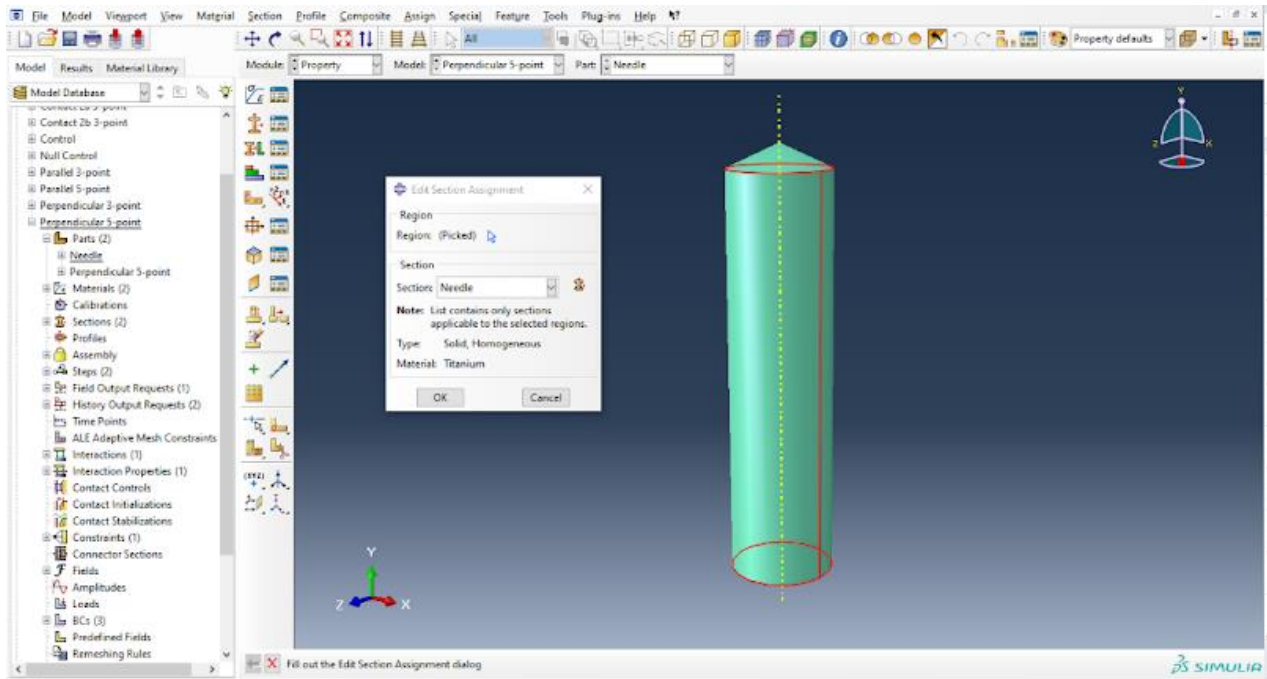
Appendix C: Perpendicular 5-point Simulation Methodology



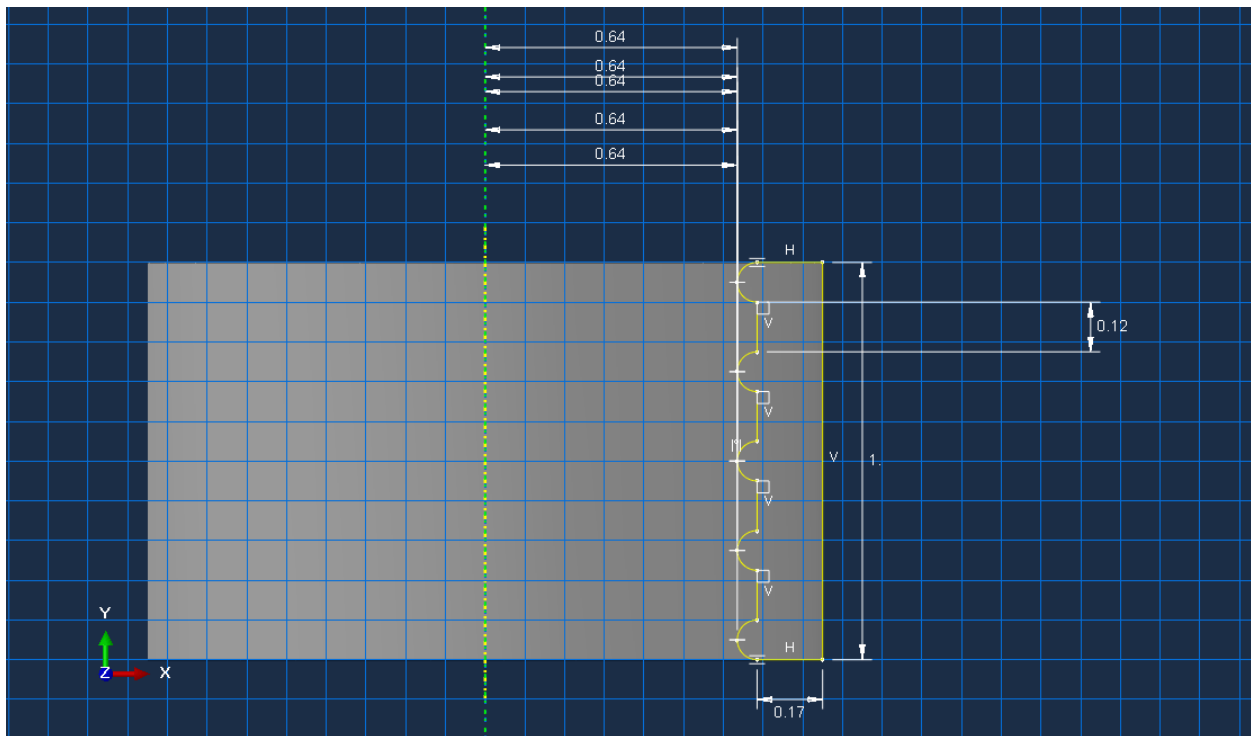
Appx. C. Figure 1: Needle Dimensions



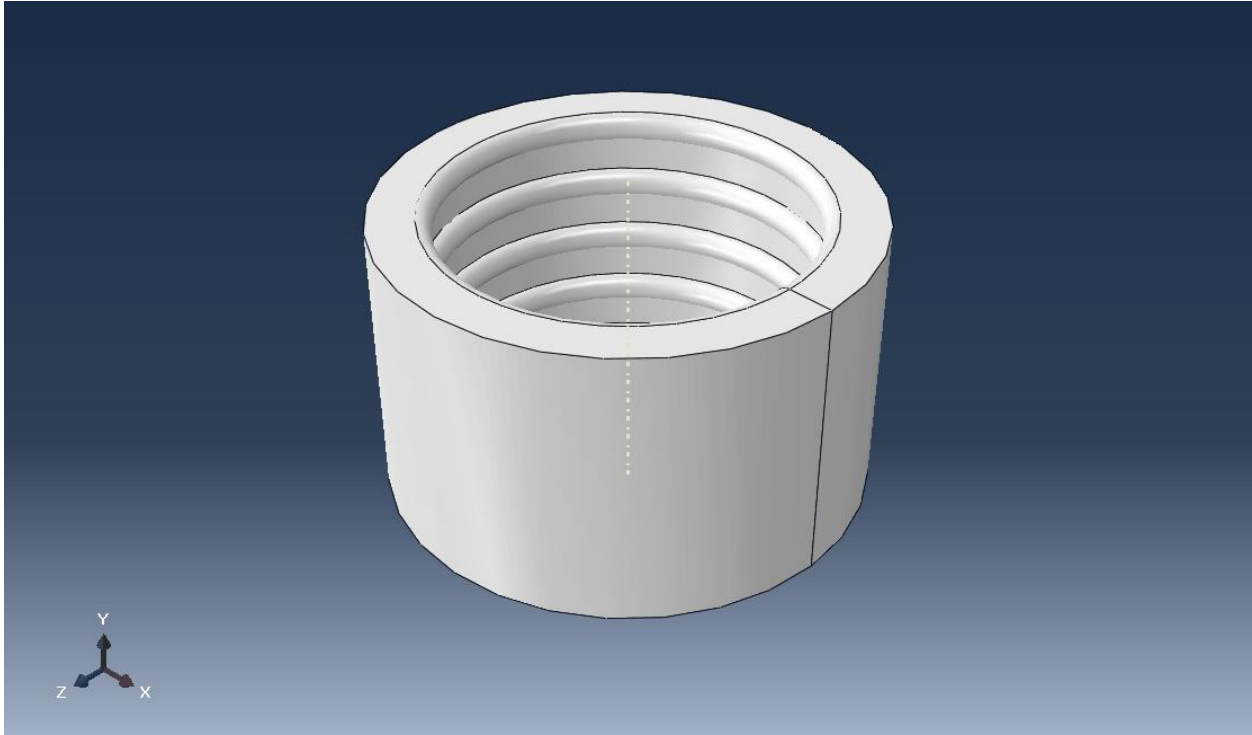
Appx. C. Figure 2: Needle Part Image



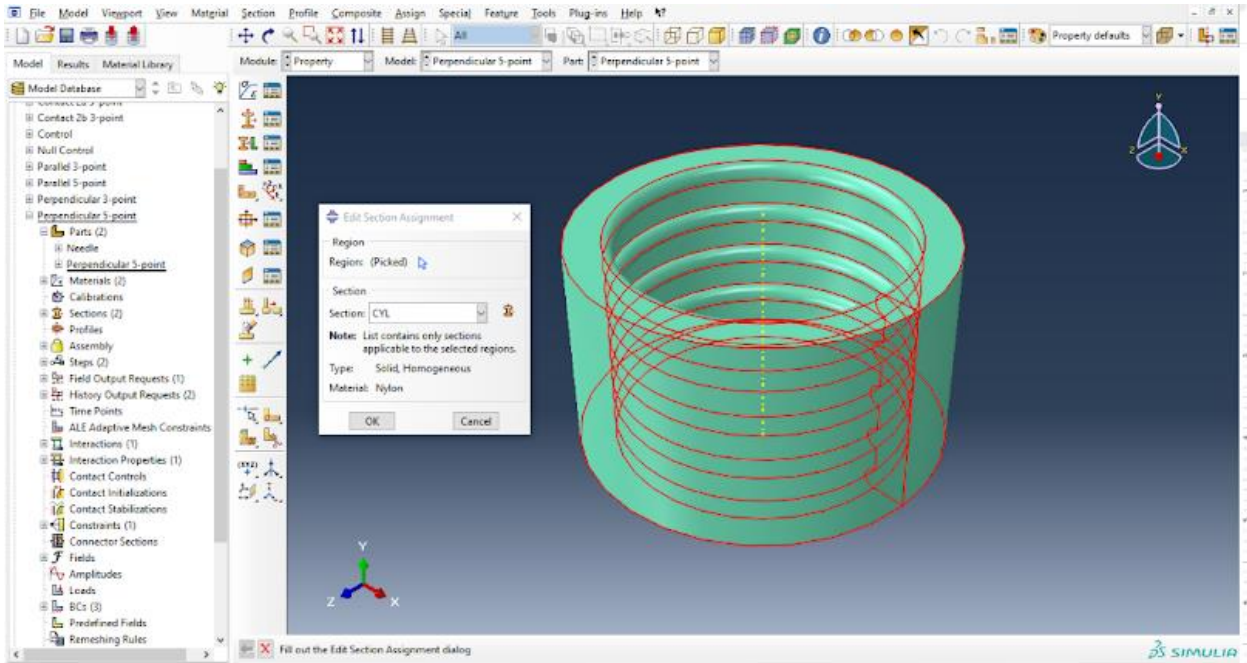
Appx. C. Figure 3: Needle Material Property



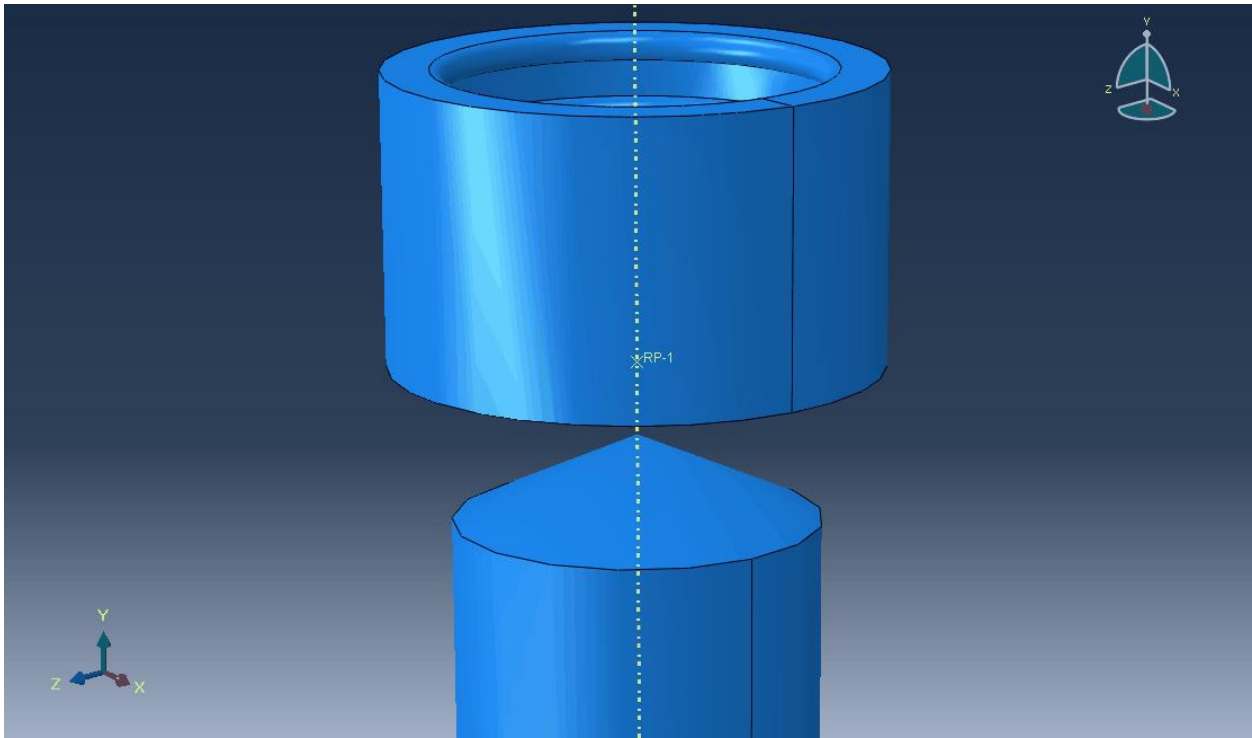
Appx. C. Figure 4: Perpendicular 5-point Dimensions



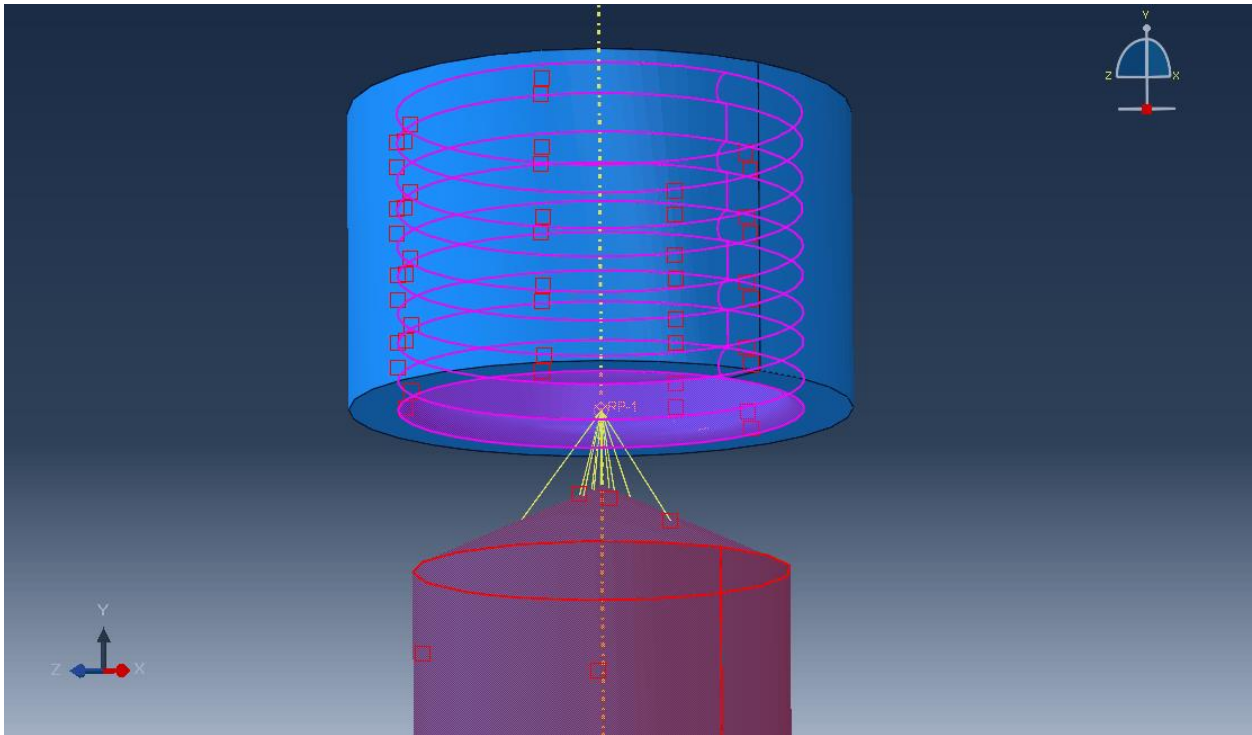
Appx. C. Figure 5: Perpendicular 5-point Part Image



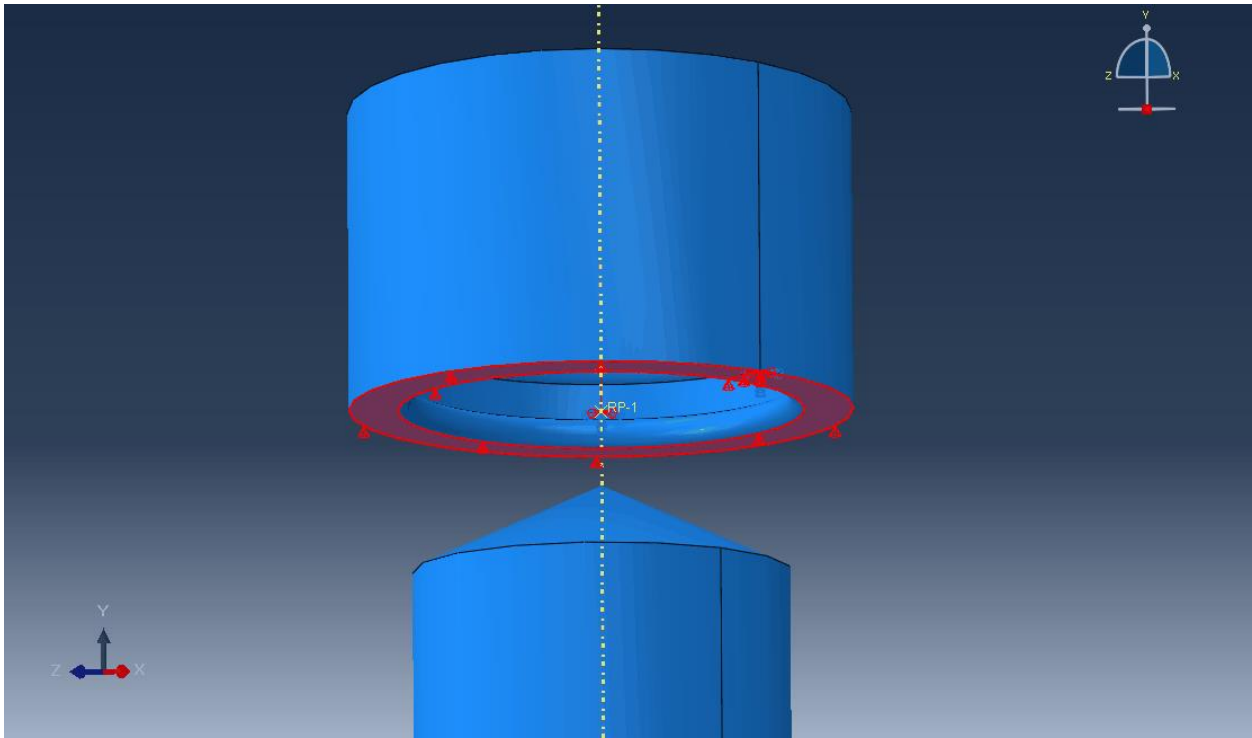
Appx. C. Figure 6: Perpendicular 5-point Material Property



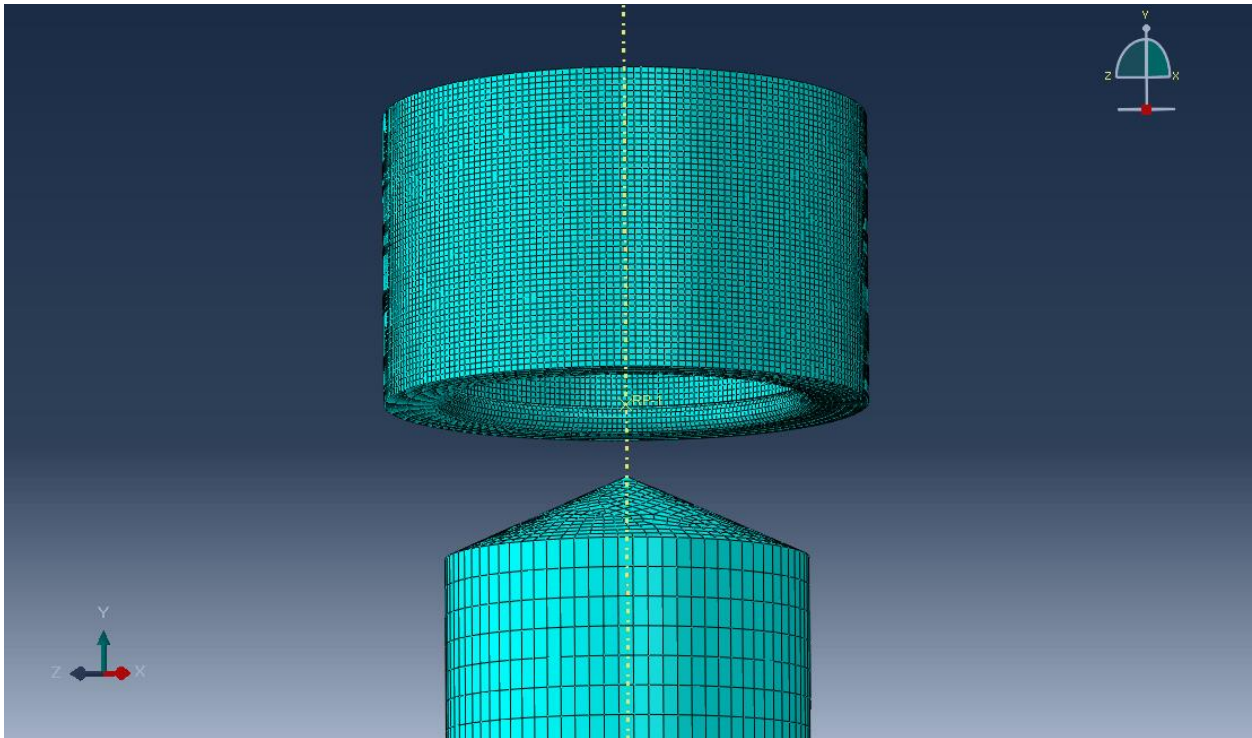
Appx. C. Figure 7: Perpendicular 5-point Assembly



Appx. C. Figure 8: Perpendicular 5-point Interaction

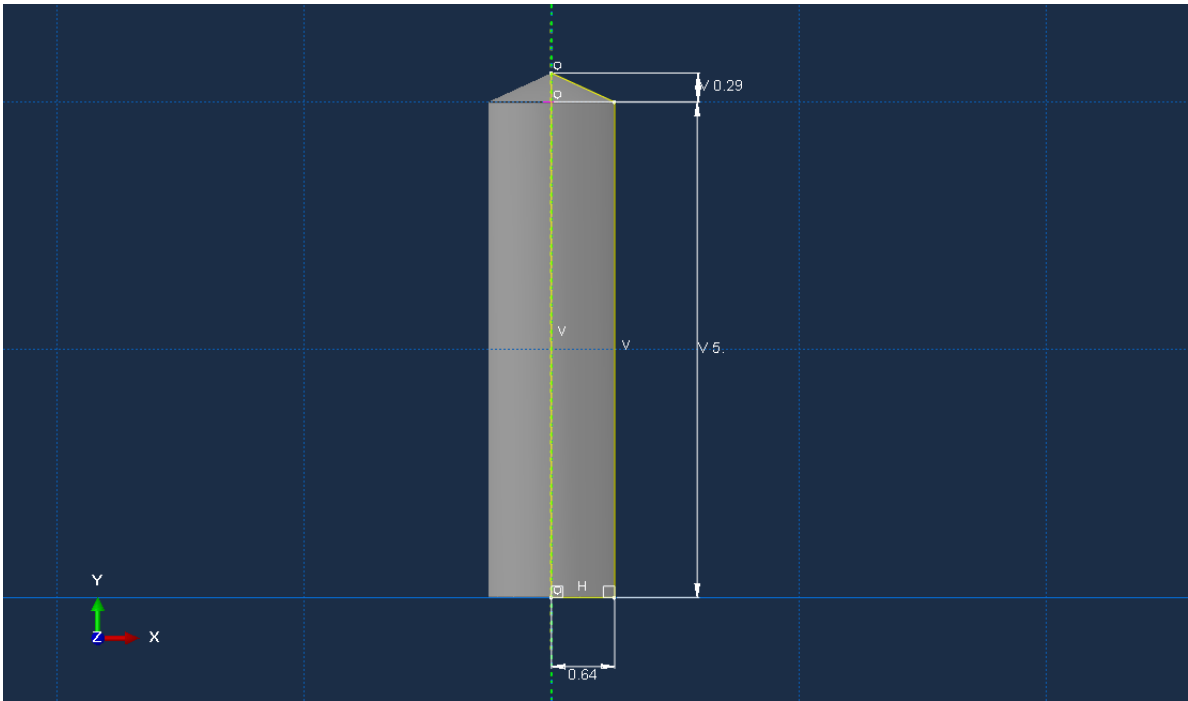


Appx. C. Figure 9: Perpendicular 5-point Boundary Conditions

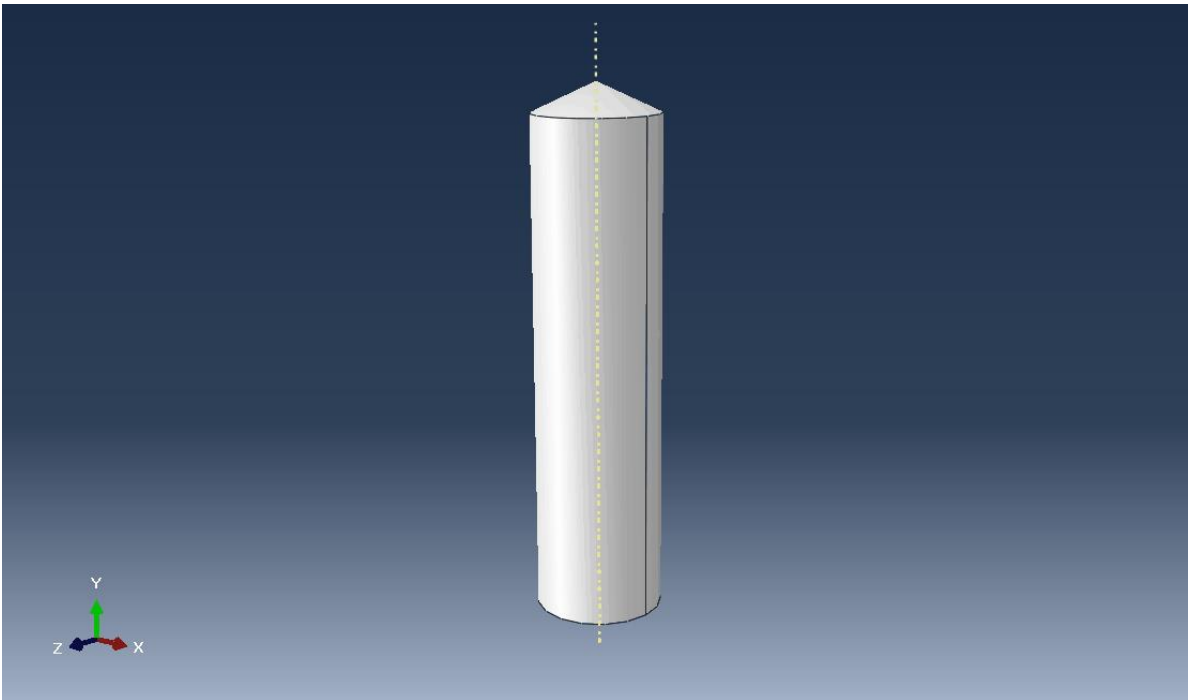


Appx. C. Figure 10: Perpendicular 5-point Mesh

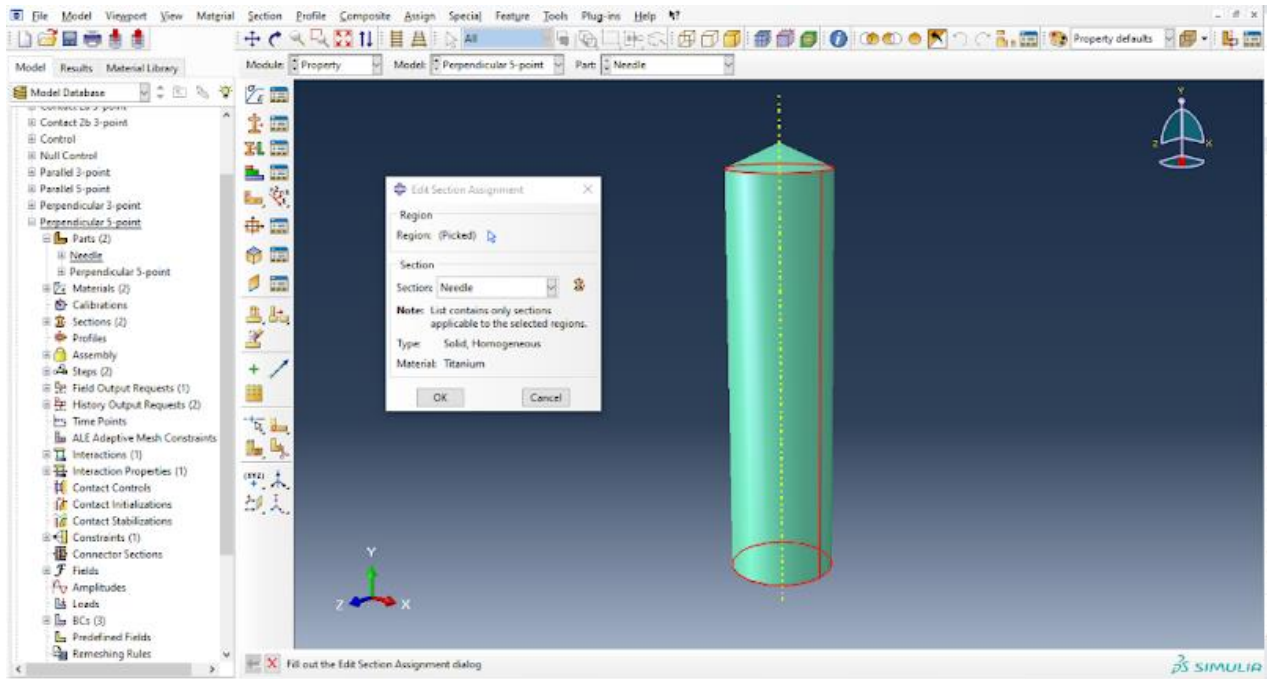
Appendix D: Perpendicular 3-point Simulation Methodology



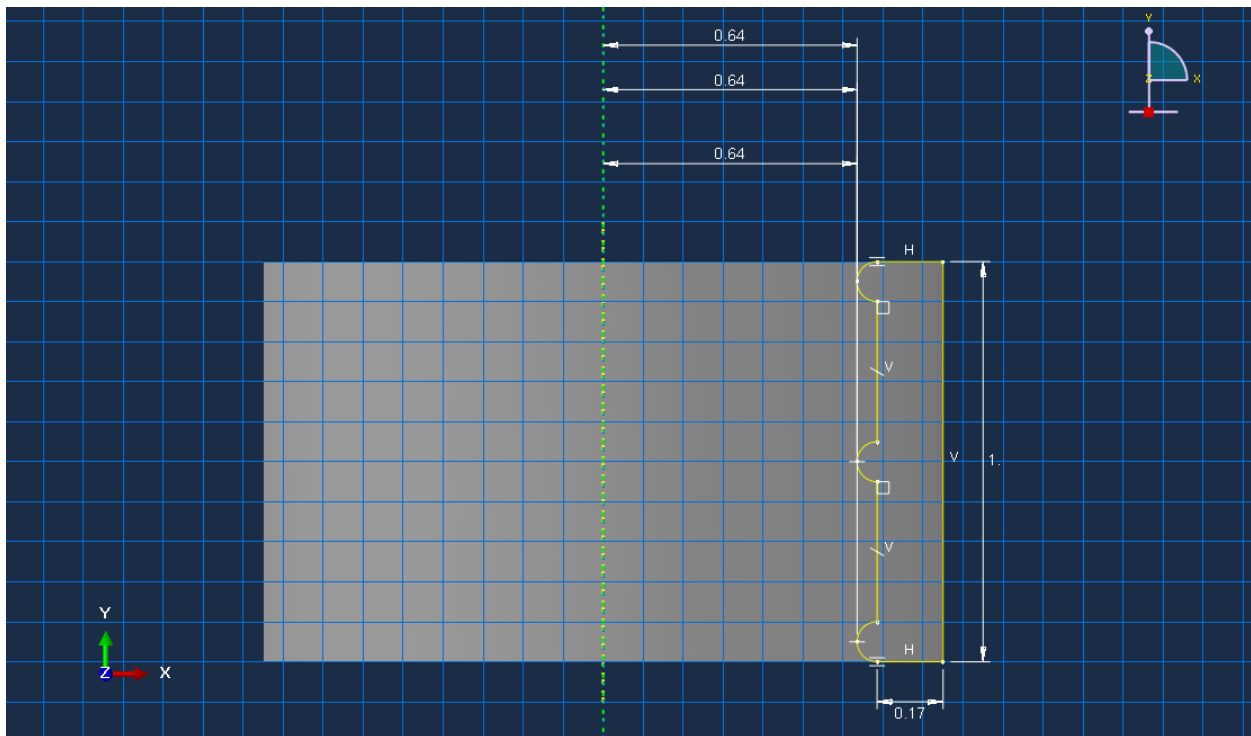
Appx. D. Figure 1: Needle Dimensions



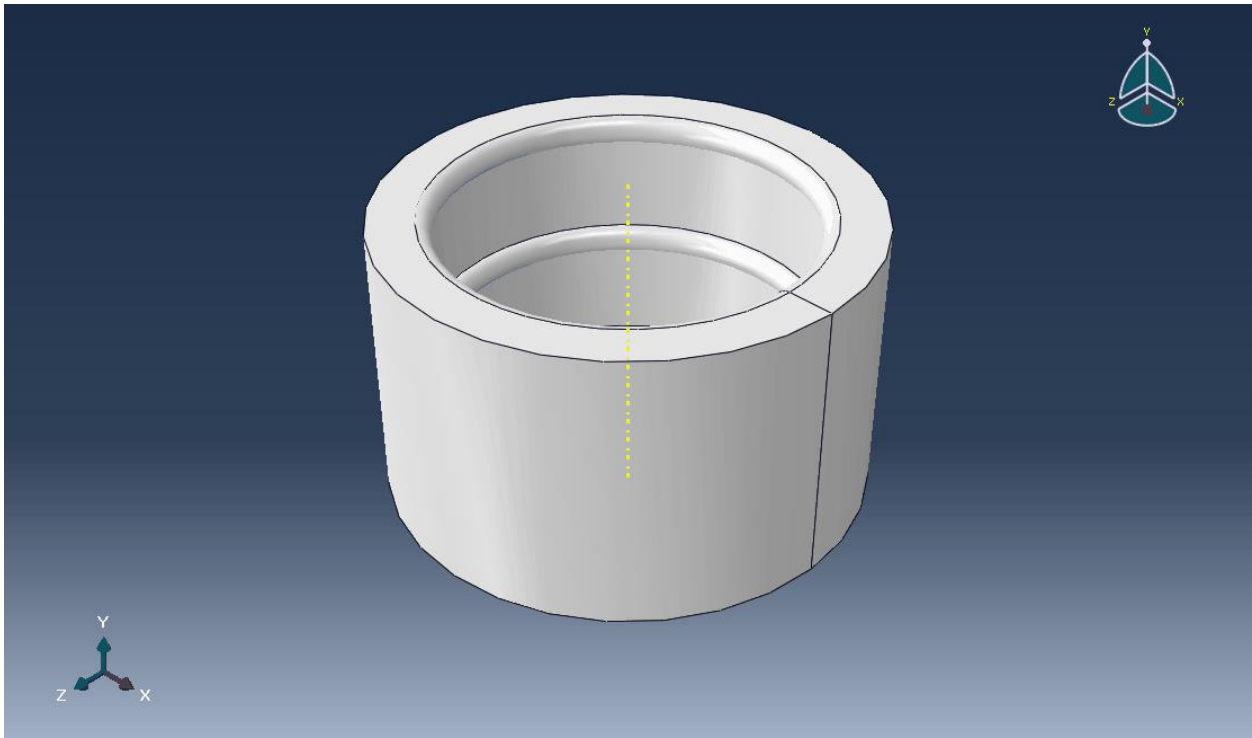
Appx. D. Figure 2: Needle Part Image



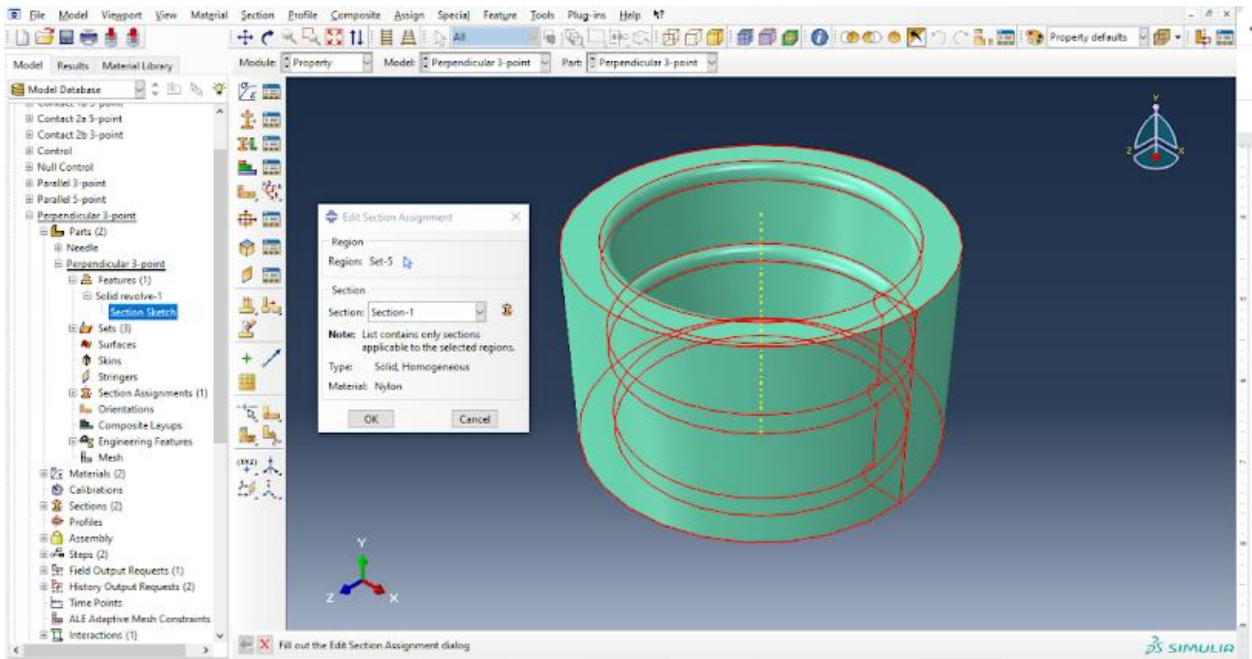
Appx. D. Figure 3: Needle Material Property



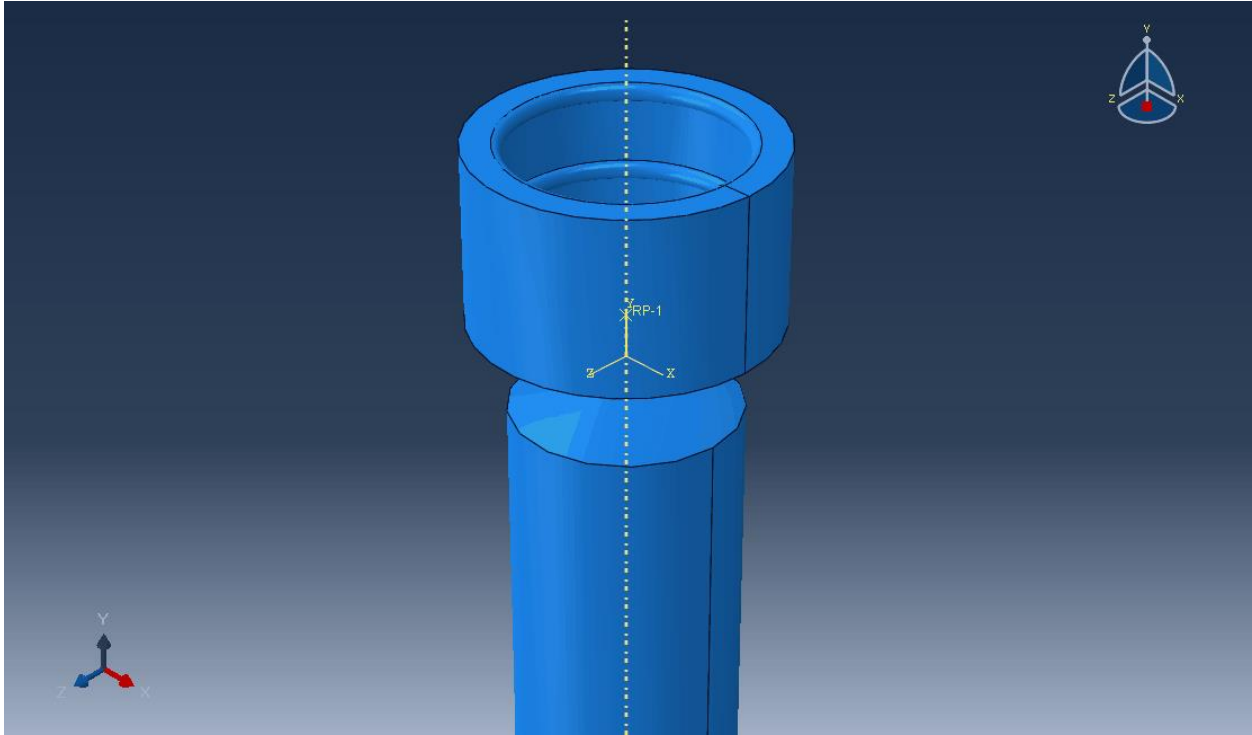
Appx. D. Figure 4: Perpendicular 3-point Dimensions



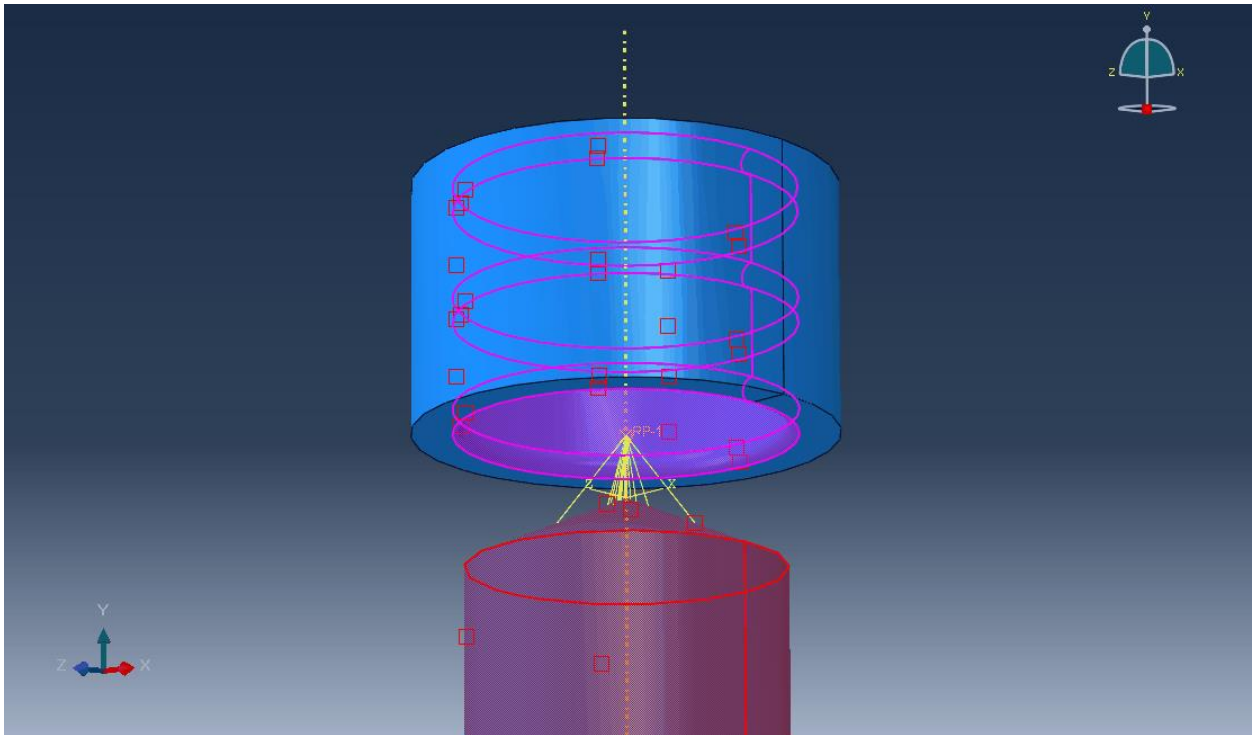
Appx. D. Figure 5: Perpendicular 3-point Part Image



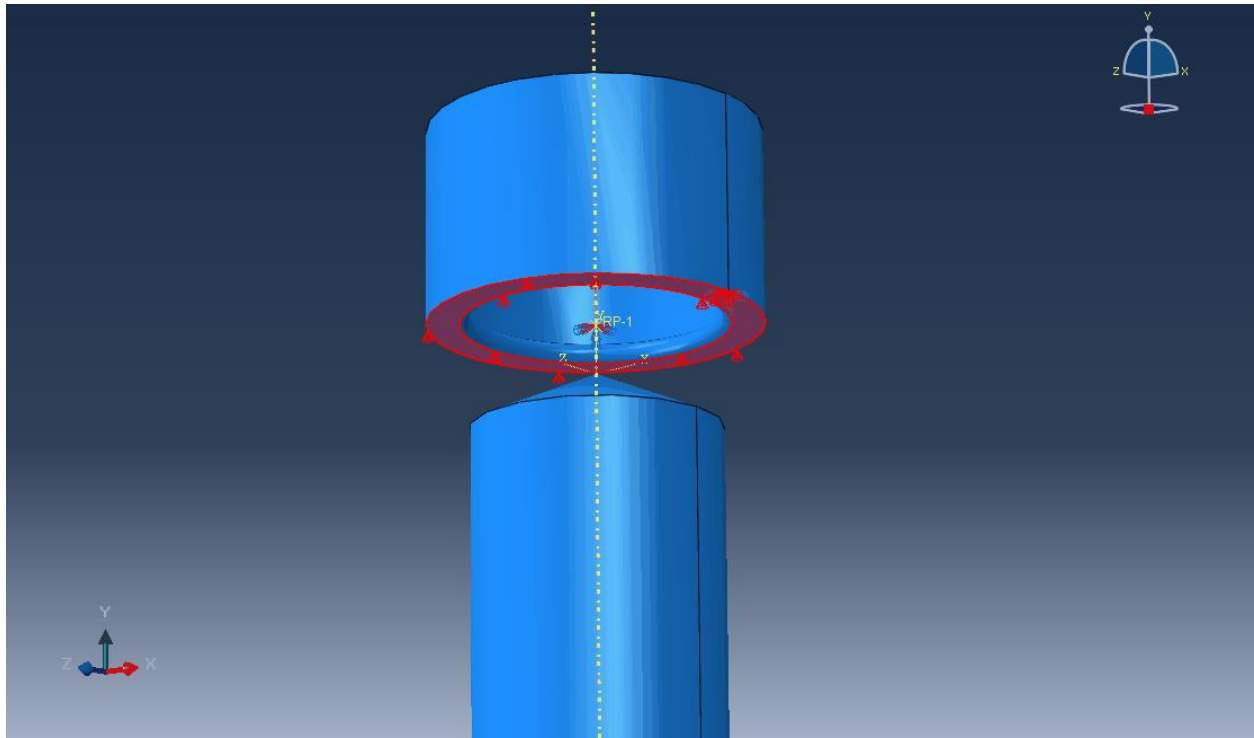
Appx. D. Figure 6: Perpendicular 3-point Material Property



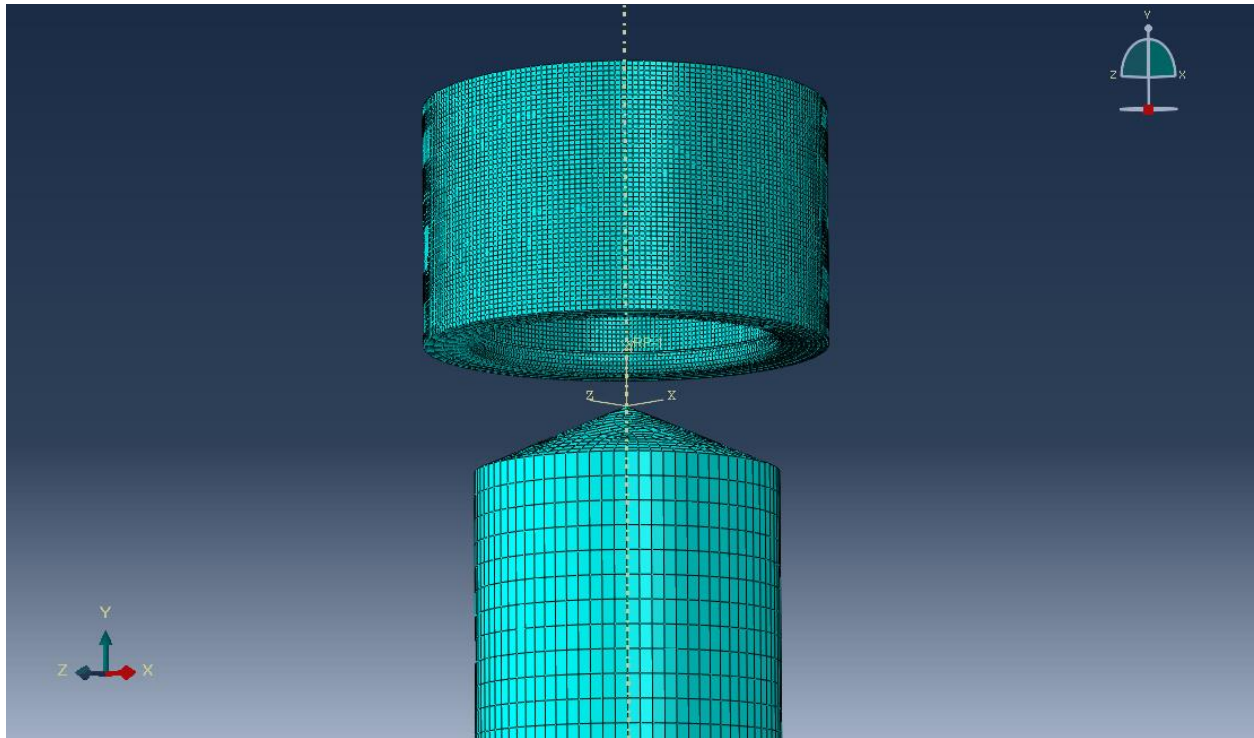
Appx. D. Figure 7: Perpendicular 3-point Assembly



Appx. D. Figure 8: Perpendicular 3-point Interaction

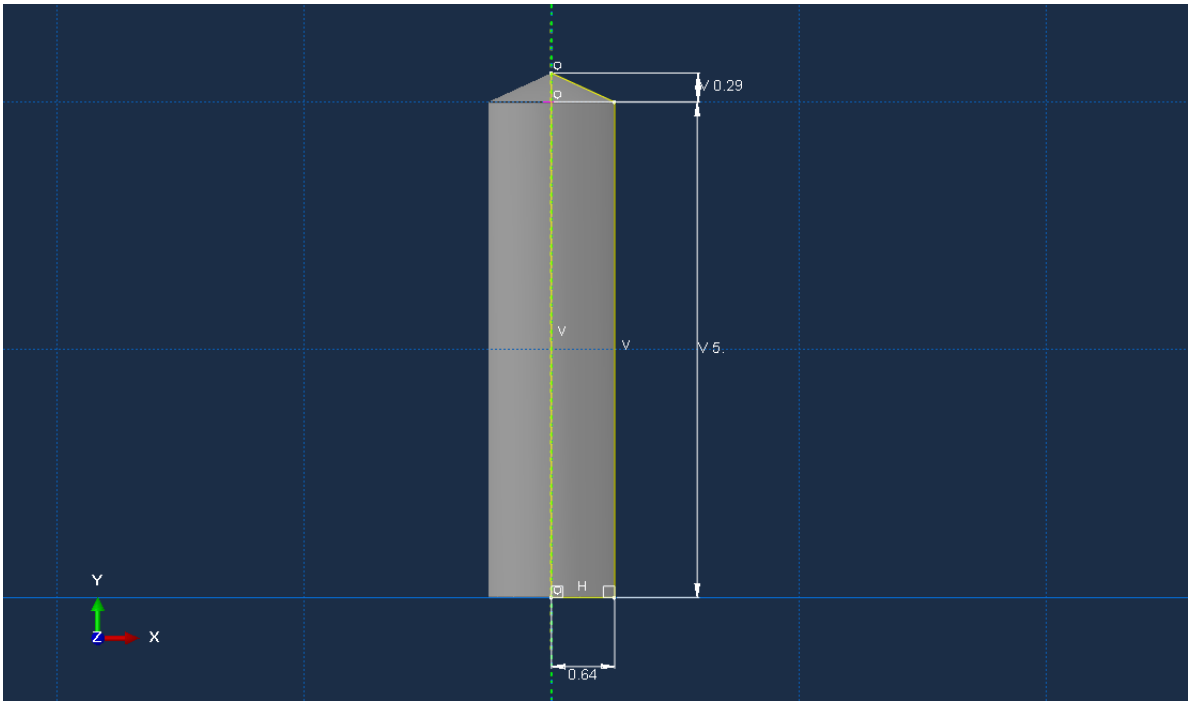


Appx. D. Figure 9: Perpendicular 3-point Boundary Conditions

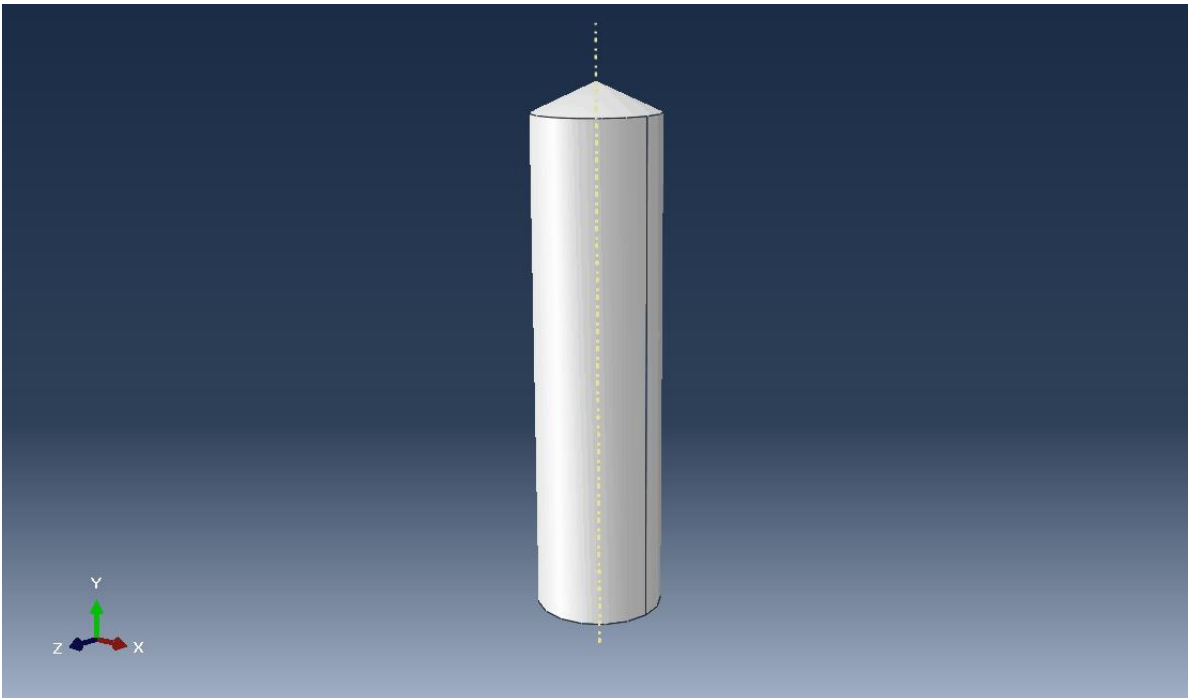


Appx. D. Figure 10: Perpendicular 3-point Mesh

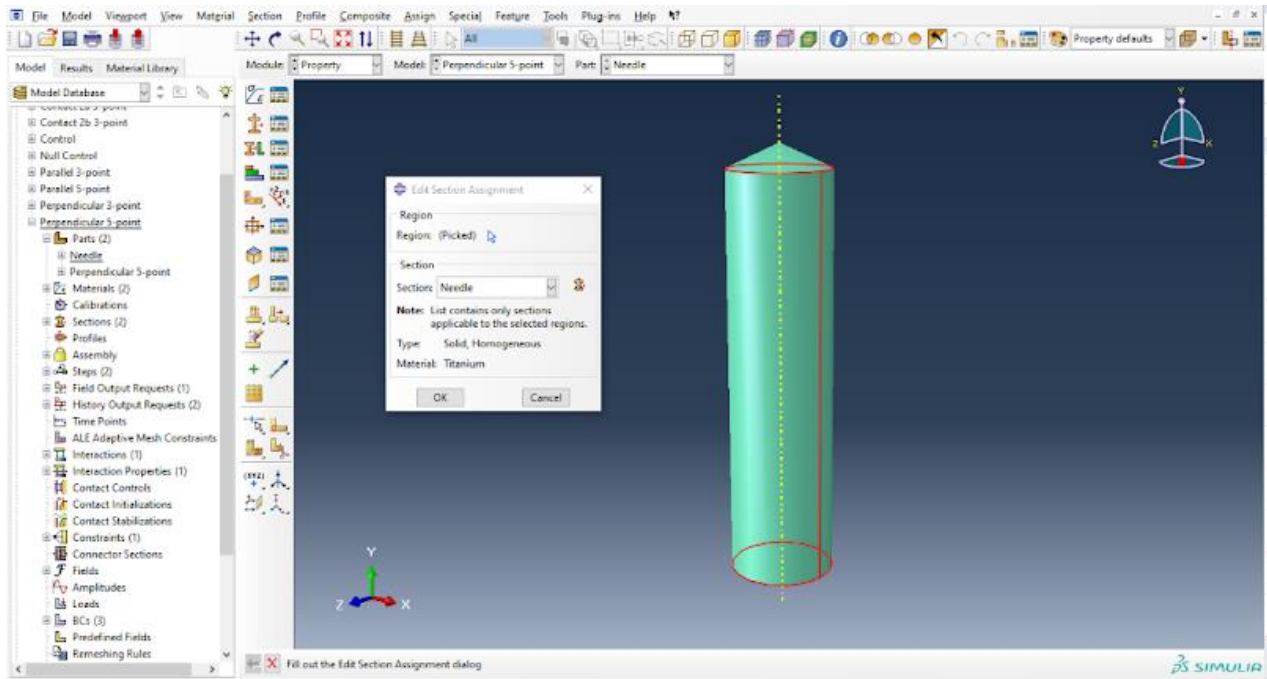
Appendix E: Parallel 3-point Simulation Methodology



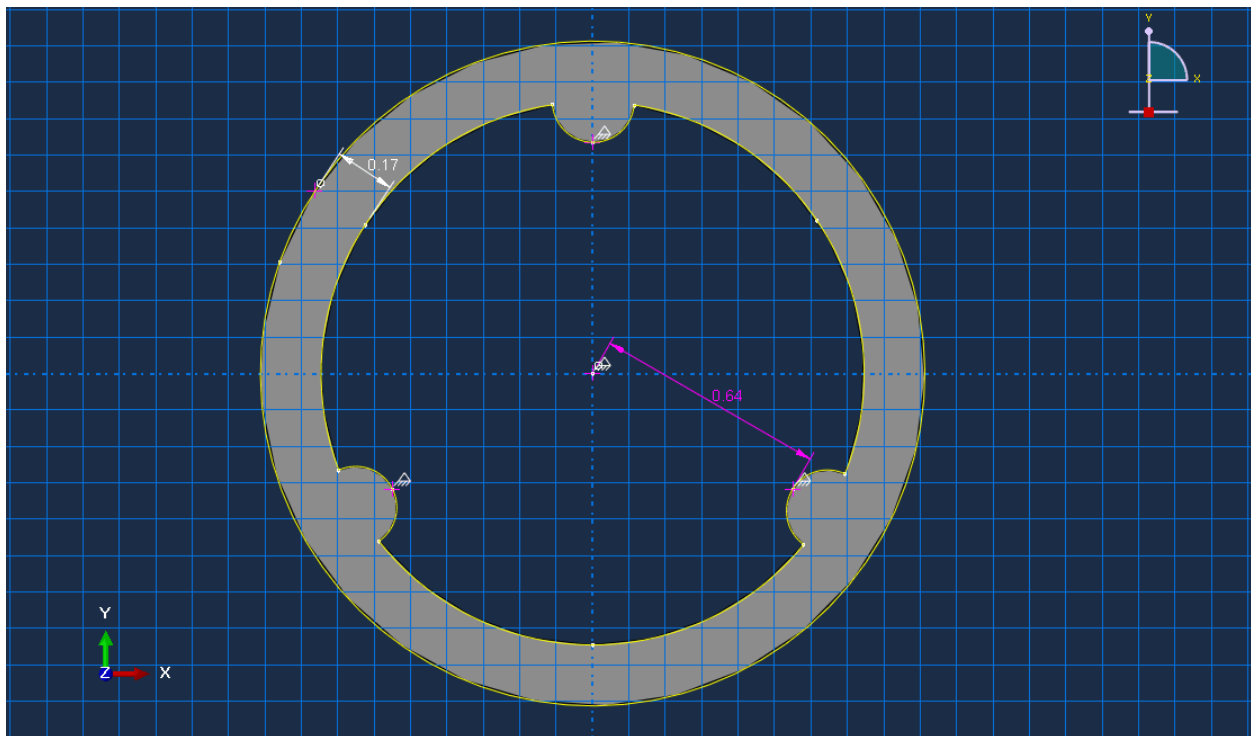
Appx. E. Figure 1: Needle Dimensions



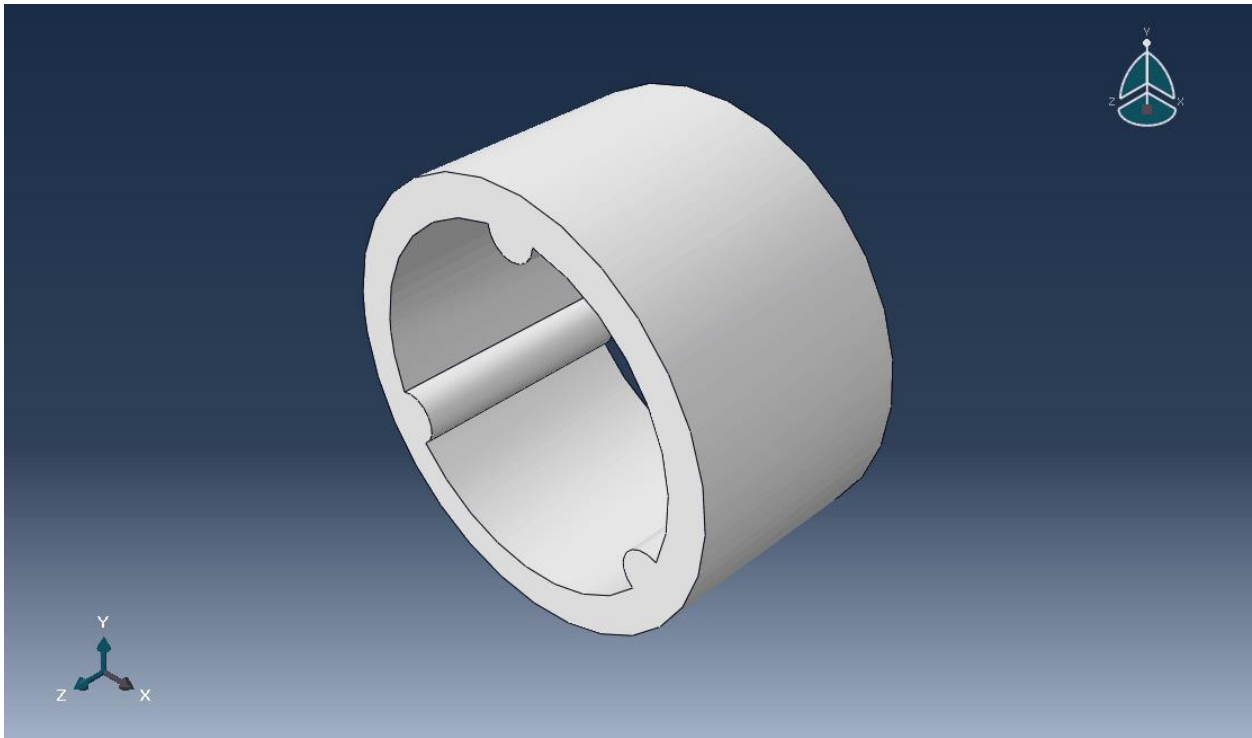
Appx. E. Figure 2: Needle Part Image



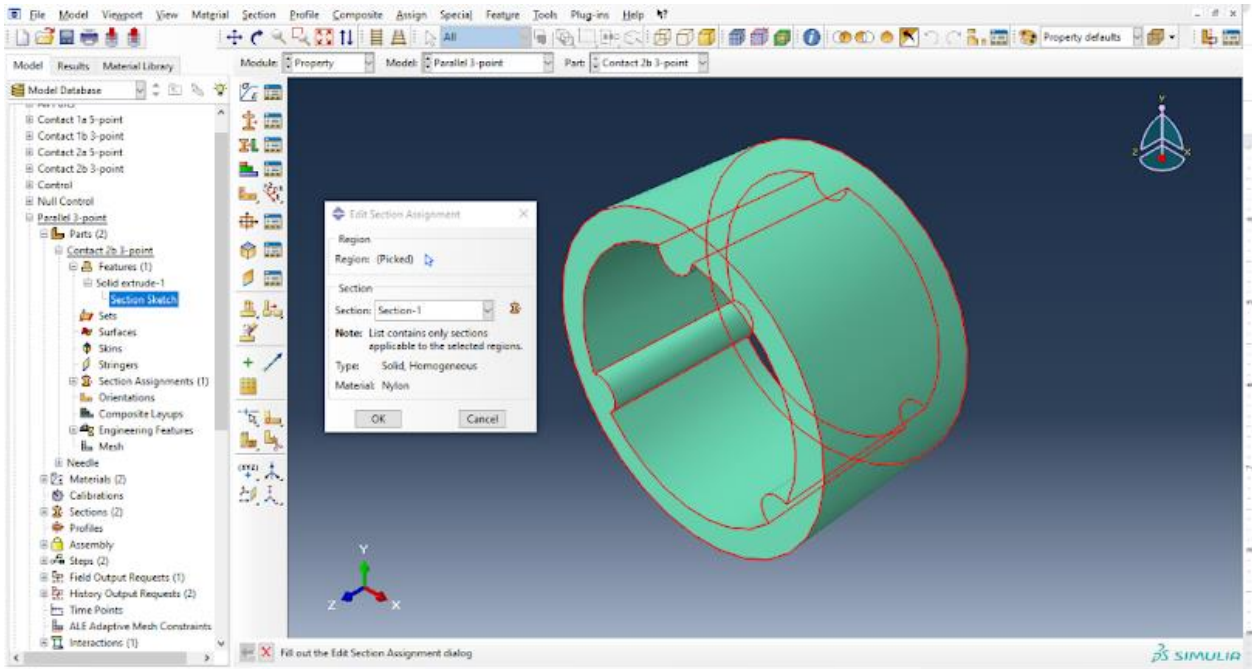
Appx. E. Figure 3: Needle Material Property



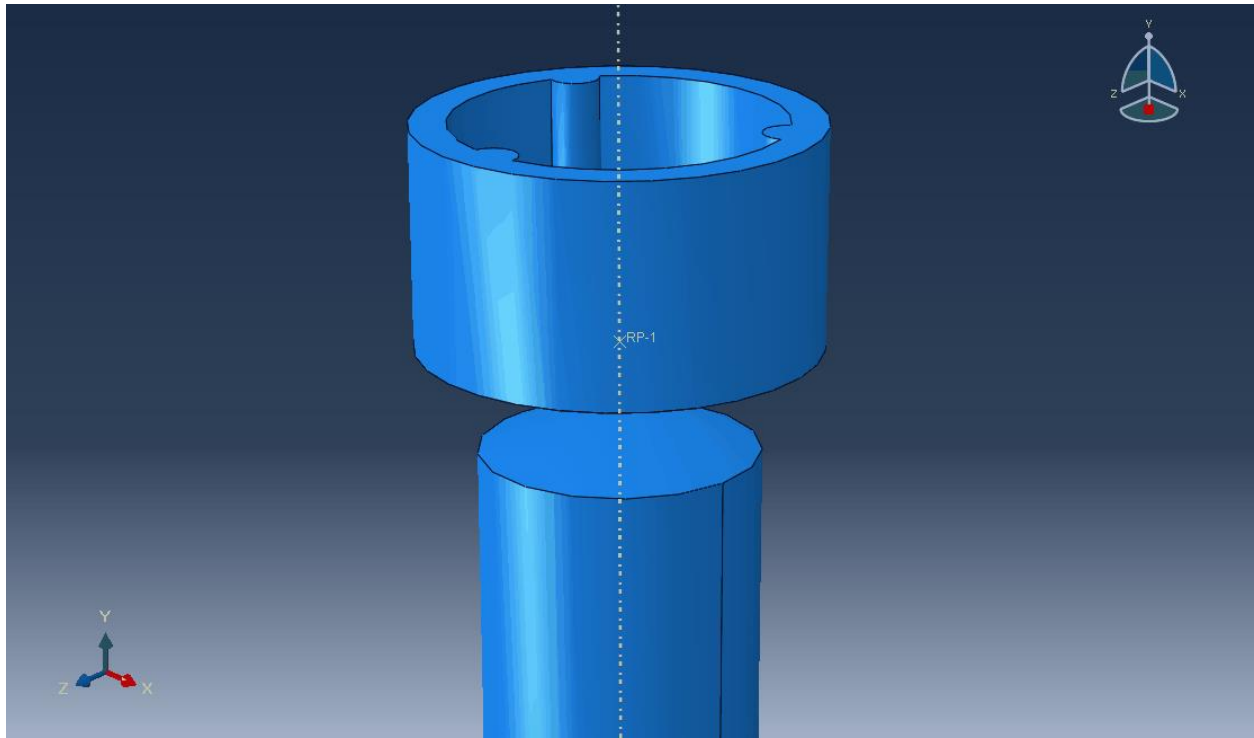
Appx. E. Figure 4: Parallel 3-point Dimensions



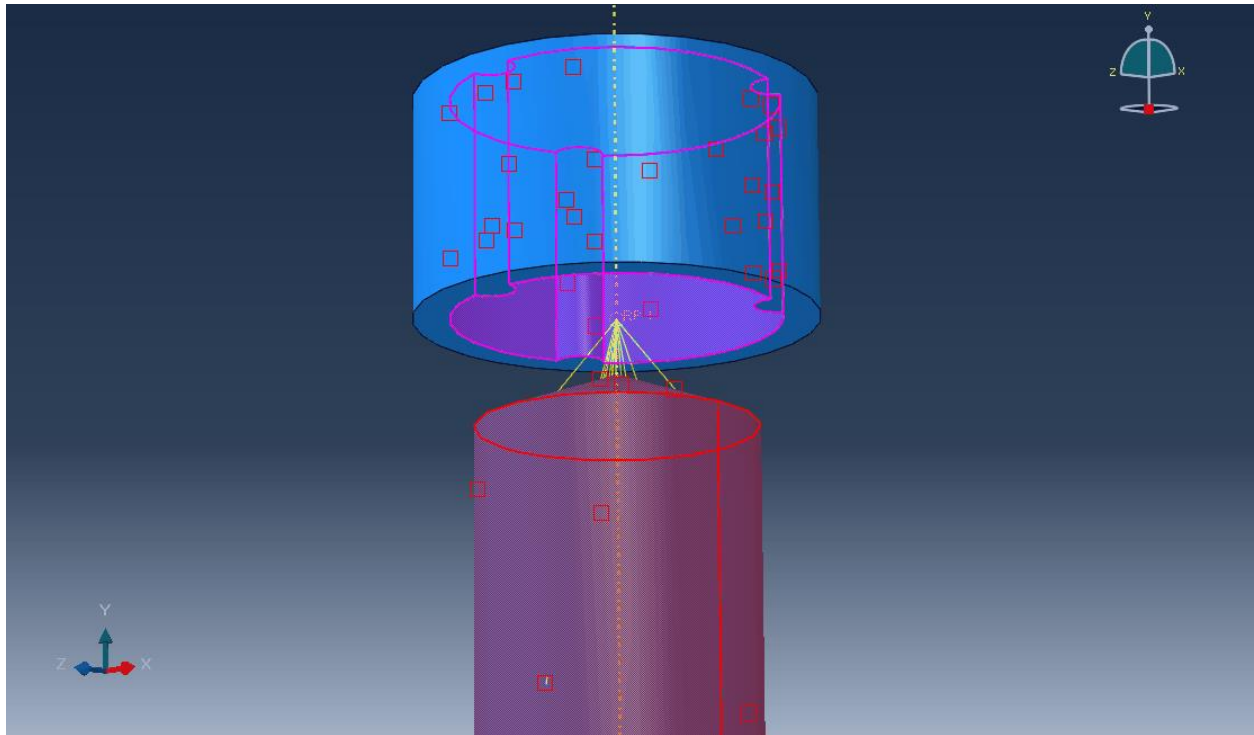
Appx. E. Figure 5: Parallel 3-point Part Image



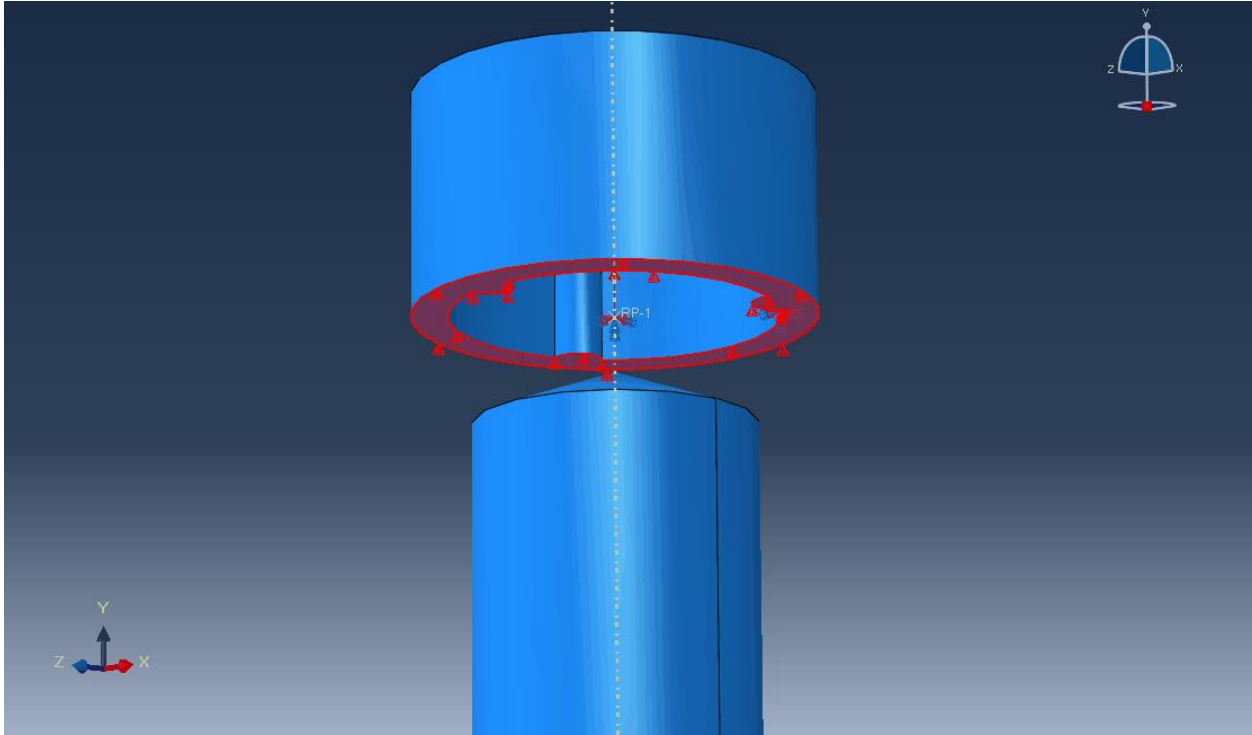
Appx. E. Figure 6: Parallel 3-point Material Property



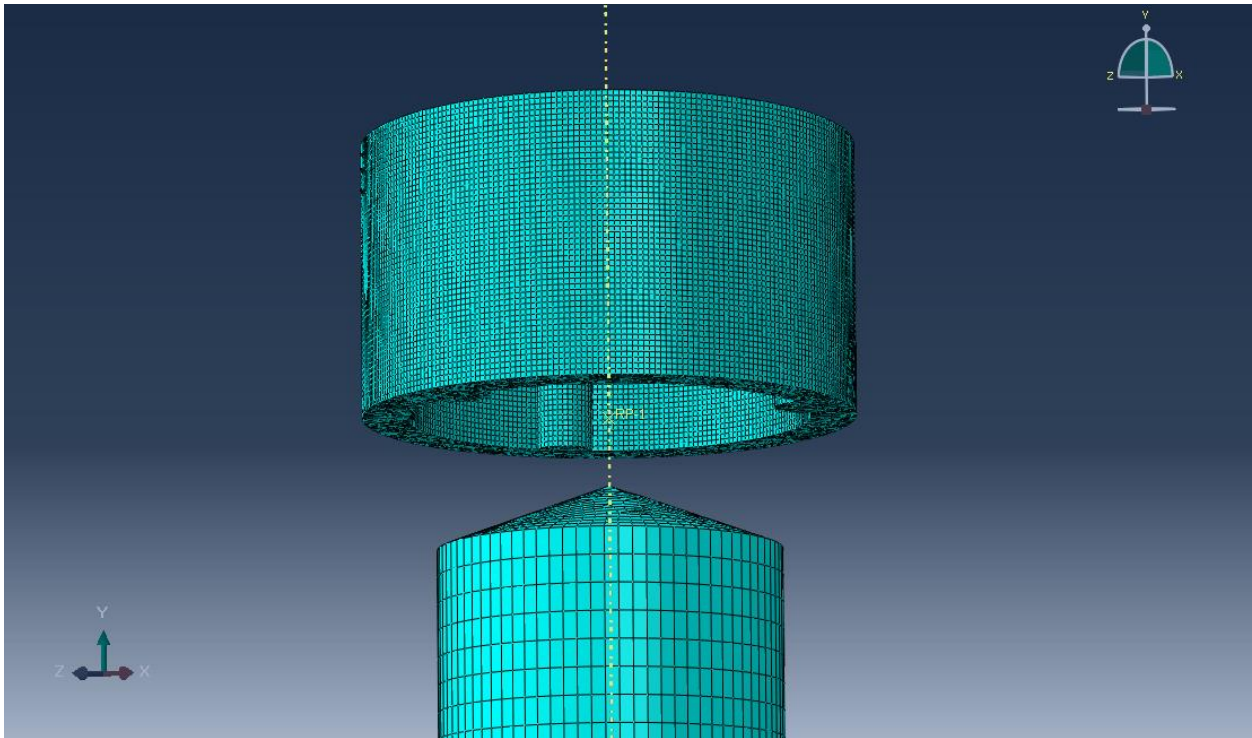
Appx. E. Figure 7: Parallel 3-point Assembly



Appx. E. Figure 8: Parallel 3-point Interaction



Appx. E. Figure 9: Parallel 3-point Boundary Conditions



Appx. E. Figure 10: Parallel 3-point Mesh

List of References

- [1] Samsam, M., *Functionally Oriented Regional Anatomy*, 5th edition, 2019, page 332, Publisher: Hayden-McNeil-Macmillan Learning Curriculum Solutions, Plymouth, MI, USA, ISBN: 978-153391175-9.
- [2] Moore K.L., Dalley A.F., Agur A.M.R., *Clinically Oriented Anatomy*, 8th edition, 2018, page 604-606, Wolters Kluwer Health. Kindle Edition, USA, ISBN:9781496347213.
- [3] Singh O., Bolla S.R., *Anatomy, Abdomen and Pelvis, Prostate*, StatPearls [Internet]. Treasure Island (FL): StatPearls Publishing; 2022 Jan., 2021 Jul 26. PMID: 31082031; Bookshelf ID: NBK540987.
- [4] “Cancer Facts & Figures 2021.” *American Cancer Society*, American Cancer Society, <https://www.cancer.org/research/cancer-facts-statistics/all-cancer-facts-figures/cancer-facts-figures-2021.html>.
- [5] D. C. Grossman *et al.*, “Screening for prostate cancer US Preventive servicetaskforcerecommendation statement,” *JAMA - J. Am. Med. Assoc.*, vol. 319, no. 18, pp. 1901–1913, 2018, doi: 10.1001/jama.2018.3710.
- [6] Balk, S. P., Ko, Y.-J., & Bubley, G. J. (2003). Biology of prostate-specific antigen. *Journal of Clinical Oncology*, 21(2), 383–391. <https://doi.org/10.1200/jco.2003.02.083>.
- [7] J. Hugosson *et al.*, “A 16-yr Follow-up of the European Randomized study of Screening for Prostate Cancer(Figure presented.)” *Eur. Urol.*, vol. 76, no. 1, pp. 43–51, 2019, doi: 10.1016/j.eururo.2019.02.009.
- [8] T F. H. Schröder *et al.*, “Screening and Prostate-Cancer Mortality in a Randomized European Study,” *N. Engl. J. Med.*, vol. 360, no. 13, pp. 1320–1328, 2009, doi: 10.1056/nejmoa0810084.
- [9] Kilpeläinen, T. P., Tammela, T. L. J., Roobol, M., Hugosson, J., Ciatto, S., Nelen, V., Moss, S., Määttänen, L., & Auvinen, A. (2011). False-positive screening results in the European randomized study of screening for Prostate cancer. *European Journal of Cancer*, 47(18), 2698–2705. <https://doi.org/10.1016/j.ejca.2011.06.055>.
- [10] K. U. Schässburger, S. Paepke, A. Saracco, E. Azavedo, C. Ekström, and H. Wiksell, “High velocity pulse biopsy device enables controllable and precise needle insertion and high yield tissue acquisition,” *Phys. Medica*, vol. 46, no. October 2017, pp. 25–31, 2018, doi: 10.1016/j.ejmp.2017.12.014.

- [11] J. Xiang, H. Yan, J. Li, X. Wang, H. Chen, and X. Zheng, “Transperineal versus transrectal prostate biopsy in the diagnosis of prostate cancer: A systematic review and meta-analysis,” *World J. Surg. Oncol.*, vol. 17, no. 1, pp. 1–11, 2019, doi: 10.1186/s12957-019-1573-0.
- [12] J. Grummet, L. Pepdjonovic, S. Huang, E. Anderson, and B. Hadaschik, “Transperineal vs. transrectal biopsy in MRI targeting,” *Transl. Androl. Urol.*, vol. 6, no. 3, pp. 368–375, 2017, doi: 10.21037/tau.2017.03.58.
- [13] T. Mkinen, A. Auvinen, M. Hakama, U. H. Stenman, and T. L. J. Tammela, “Acceptability and complications of prostate biopsy in population-based PSA screening versus routine clinical practice: A prospective, controlled study,” *Urology*, vol. 60, no. 5, pp. 846–850, 2002, doi: 10.1016/S0090-4295(02)01864-2.
- [14] Donahue, T., & Moul, J. (2002). Diagnostic accuracy of prostate needle biopsy. *Current Urology Reports*, 3(3), 215–221. <https://doi.org/10.1007/s11934-002-0067-7>.
- [15] Bjurlin, M. A., Carroll, P. R., Eggener, S., Fulgham, P. F., Margolis, D. J., Pinto, P. A., Rosenkrantz, A. B., Rubenstein, J. N., Rukstalis, D. B., Taneja, S. S., & Turkbey, B. (2020). Update of the Standard Operating Procedure on the Use of Multiparametric Magnetic Resonance Imaging for the Diagnosis, Staging and Management of Prostate Cancer. *The Journal of urology*, 203(4), 706–712. <https://doi.org/10.1097/JU.0000000000000617>.
- [16] L. C. Brown *et al.*, “Multiparametric MRI to improve detection of prostate cancer compared with transrectal ultrasound-guided prostate biopsy alone: The PROMIS study,” *Health Technol. Assess. (Rockv)*, vol. 22, no. 39, pp. 1–175, 2018, doi: 10.3310/hta22390.
- [17] W. Li, Y. Wang, V. Nteziyaremye, H. Yamaguchi, and A. J. Shih, “Measurement of the Friction Force Inside the Needle in Biopsy,” *J. Manuf. Sci. Eng. Trans. ASME*, vol. 138, no. 3, 2016, doi: 10.1115/1.4031050.
- [18] J J. K. Sehn, “Prostate Cancer Pathology: Recent Updates and Controversies.,” *Mo. Med.*, vol. 115, no. 2, pp. 151–155, 2018, [Online]. Available: <http://www.ncbi.nlm.nih.gov/pubmed>.
- [19] D. Gao, Y. Lei, and B. Yao, *Analysis of dynamic tissue deformation during needle insertion into soft tissue*, vol. 46, no. 5. IFAC, 2013.
- [20] Mahvash, M., & Dupont, P. E. (2009). Fast Needle Insertion to Minimize Tissue Deformation and Damage. *IEEE International Conference on Robotics and Automation : ICRA : [proceedings]. IEEE International Conference on Robotics and Automation, 2009*, 3097–3102. <https://doi.org/10.1109/ROBOT.2009.5152617>.
- [21] N. Abolhassani and R. V. Patel, “Deflection of a flexible needle during insertion into soft tissue,” *Annu. Int. Conf. IEEE Eng. Med. Biol. - Proc.*, pp. 3858–3861, 2006, doi: 10.1109/IEMBS.2006.259519.

- [22] Tsumura, R., Takishita, Y., Fukushima, Y., & Iwata, H. (2016). Histological evaluation of tissue damage caused by rotational needle insertion. *2016 38th Annual International Conference of the IEEE Engineering in Medicine and Biology Society (EMBC)*. <https://doi.org/10.1109/embc.2016.7591879>.
- [23] Li, A. D., Liu, Y., Plott, J., Chen, L., Montgomery, J. S., & Shih, A. (2021). Multi-bevel needle design enabling accurate insertion in biopsy for cancer diagnosis. *IEEE Transactions on Biomedical Engineering*, *68*(5), 1477–1486. <https://doi.org/10.1109/tbme.2021.3054922>.
- [24] Li, A., Plott, J., Chen, L., Montgomery, J. S., & Shih, A. (2020). Needle deflection and tissue sampling length in needle biopsy. *Journal of the mechanical behavior of biomedical materials*, *104*, 103632. <https://doi.org/10.1016/j.jmbbm.2020.103632>.
- [25] J. Schaible *et al.*, “Full-core biopsy systems take larger liver tissue samples with lower fragmentation rates than conventional side-notch systems: A randomized trial,” *Cancer Manag. Res.*, vol. 12, pp. 1121–1128, 2020, doi: 10.2147/CMAR.S209824.
- [26] Young Bang, J., Krall, K., Jhala, N., Singh, C., Tejani, M., Arnoletti, J. P., Navaneethan, U., Hawes, R., & Varadarajulu, S. (2021). Comparing needles and methods of endoscopic ultrasound–guided fine-needle biopsy to optimize specimen quality and diagnostic accuracy for patients with pancreatic masses in a randomized trial. *Clinical Gastroenterology and Hepatology*, *19*(4). <https://doi.org/10.1016/j.cgh.2020.06.042>.
- [27] S Zhou, Steve R., et al. “Prostate Cancer Detection Rate of Freehand versus 3-Dimensional Template Mapping Biopsy Using a Magnetic Resonance Imaging-Ultrasound Fusion Device in Biopsy Naïve Men.” *Journal of Urology*, vol. 203, no. 4, 2020, pp. 699–705., <https://doi.org/10.1097/ju.0000000000000587>.
- [28] C. S. McGill, J. A. Schwartz, J. Z. Moore, P. W. McLaughlin, and A. J. Shih, “Precision grid and hand motion for accurate needle insertion in brachytherapy,” *Med. Phys.*, vol. 38, no. 8, pp. 4749–4759, 2011, doi: 10.1118/1.3611040.
- [29] C. M. Brede, N. J. Douville, and S. Jones, “Variable correlation of grid coordinates to core location in template prostate biopsy,” *Curr. Urol.*, vol. 6, no. 4, pp. 194–198, 2013, doi: 10.1159/000343538.
- [30] Casanova, F., Carney, P. R., & Sarntinoranont, M. (2014). In vivo evaluation of needle force and friction stress during insertion at varying insertion speed into the brain. *Journal of neuroscience methods*, *237*, 79–89. <https://doi.org/10.1016/j.jneumeth.2014.08.012>.
- [31] Fink, K. G., Hutarew, G., Pytel, A., & Schmeller, N. T. (2005). Prostate biopsy outcome using 29 mm cutting length. *Urologia Internationalis*, *75*(3), 209–212. <https://doi.org/10.1159/000087795>.

- [32] Simpfendörfer, T., Kuru, T. H., Steinemann, S., Bergsträsser, C., Block, S., Roth, W., Roethke, M. C., Hohenfellner, M., & Hadaschik, B. A. (2014). Trocar-sharpened needles for image-guided prostate biopsy improve sample quality and performance: First clinical results. *Journal of Endourology*, 28(11), 1384–1388.
<https://doi.org/10.1089/end.2014.0121>.
- [33] Hurlston, Robert. “Abaqus vs Solidworks Simulation.” *Fidelis*, Fidelis, 10 Oct. 2022, <https://www.fidelisfea.com/post/abaqus-vs-solidworks-simulation>.
- [34] “Stress-Strain Properties.” *Stress-Strain Properties - 3 - MATLAB Cody - MATLAB Central*, <https://www.mathworks.com/matlabcentral/cody/problems/8050-stress-strain-properties-3>.
- [35] Franiel T;Fritzsche F;Staack A;Rost J;Hamm B;Beyersdorff D; “[Histopathologic Quality of Prostate Core Biopsy Specimens: Comparison of an MR-Compatible Biopsy Needle and a Ferromagnetic Biopsy Needle Used for Ultrasound-Guided Prostate Biopsy].” *RoFo : Fortschritte Auf Dem Gebiete Der Rontgenstrahlen Und Der Nuklearmedizin*, U.S. National Library of Medicine, <https://pubmed.ncbi.nlm.nih.gov/16933199/>.
- [36] “Retlaw Industries.” *Custom Thermoplastic Product Manufacturers in Hartland, Wisconsin*, <https://www.retlawindustries.com/PlasticTypes>.
- [37] “Titanium Properties.” *Kyocera SGS Europe*, <https://kyocera-sgstool.co.uk/titanium-resources/titanium-information-everything-you-need-to-know/titanium-properties/#:~:text=It's%20Young's%20modulus%20of%20elasticity,shear%20modulus%20of%2045%20GPA>.
- [38] “Modulus of Elasticity.” *Young's Modulus: Modulus of Elasticity Units & Formula*, <https://omnexus.specialchem.com/polymer-properties/properties/young-modulus#:~:text=The%20modulus%20of%20elasticity%20of%20nylon%20is%202.7,0.4%20x%20106%20psi>.